Search for Single Top–Quark Production via Flavor-Changing Neutral Currents with the CDF II Experiment

Antonios Papaikonomou

Zur Erlangung des akademischen Grades eines
DOKTORS DER NATURWISSENSCHAFTEN
von der Fakultät für Physik der
Universität Karlsruhe (TH)

genehmigte

Dissertation

von

Dipl. Phys. Antonios Papaikonomou
aus Athen, Griechenland

Tag der mündlichen Prüfung: 19.06.2009

Referent: Prof. Dr. Th. Müller, Institut für Experimentelle Kernphysik

Korreferent: Prof. Dr. W. Wagner, Bergische Universität Wuppertal, Gaußstr.20, 42097 Wuppertal

Introduction

The discovery of the top quark in 1995 at Fermilab completed the puzzle of the third family of the Standard Model (SM). The mass of this particle, though, turned out to be much larger ($m_{top} = (173.1 \pm 1.3)$ GeV/c^2) than first expected, about 40 times that of the bottom quark, the top's weak isospin partner in the third family. The top mass is of the order of the Electro-Weak Symmetry Breaking (EWSB) scale $v = 246$ GeV and therefore provides a probe of the physics associated with the generation of weak gauge-boson masses. The top quark can be produced in the SM either via the strong interaction in top-antitop quark pairs or singly via the electroweak interaction.

The possibility of single top-quark production via the strong interaction is not implemented in the SM. This could occur through flavor-changing neutral currents (FCNC) which means through interactions, by which a quark flavor is transformed to another quark flavor in the final state, while the charge of the initial quark state remains the same for the final quark state. However, the SM does not contain FCNC at tree level, though they can occur at higher order through radiative corrections. Because of the loop suppression, these SM effects will be small, and therefore, large FCNC provide a window to physics beyond the SM.
According to theoretical predictions, the anomalous FCNC couplings may be significant in many extensions to the SM (e.g. supersymmetry) and could be detected at hadron colliders. In this analysis, we are specifically interested in the t-u-g coupling and the t-c-g coupling, two of the possibilities to produce a top quark via 'anomalous' FCNC couplings. In this scenario, an up quark or a charm quark and a gluon from the colliding hadrons combine to form a top quark, which then decays.
In this thesis, the top-quark is reconstructed based on its SM decay-signature $t \rightarrow bW$ and subsequent leptonic W-boson decay. The latter consists of a bottom quark jet, a lepton and missing energy (neutrino). The lepton and its corresponding neutrino originate from the W boson decay.
The result of my analysis is hence the measurement of the production cross-section multiplied by the branching ratio BR($t \rightarrow bW$). This can be interpreted within an effective theory, a model-independent approach, which is not fundamental and only valid up to a specific energy scale. Within this theoretical framework, the expressions, which stand for quantities like the matrix element, the cross section and the decay rate, contain the parametrization of the anomalous coupling constants κ_{gtu} and κ_{gtc}. The main goal of our analysis is to set an upper limit on the cross section of the anomalous top-quark production-channel $u(c) + g \rightarrow t$. The result is then used to deduce an upper limit for the anomalous couplings and the corresponding branching ratios. This search uses CDF Run II data corresponding to an integrated luminosity of 2.2 fb^{-1}.

Contents

Chapter 1

Theoretical Framework

In this chapter, the theoretical background of the analysis, presented in this thesis, is discussed. The chapter consists of two main sections. The first section, section 1.1, is shortly introducing the physics described by the so called Standard Model of particle physics. The second part of the chapter, section 1.2 is referring to new physics, that is, physics beyond the range of the established Standard Model. The aim of both sections is to describe quantities relevant to the analysis.

1.1 Standard Model Physics

This section consists of three parts. Section 1.1.1 gives an overview of the theoretical structure of the Standard Model of particle physics. Furthermore, it introduces and defines the parameters used later on in this analysis. In section 1.1.2, the top-quark production within the framework of the Standard Model is discussed. The last part, section 1.1.3, deals with the concept and importance of the interactions, known as FCNC.

1.1.1 The Standard Model (SM)

There are four fundamental forces considered by the physicists to be the generators of any known interaction in nature: The strong force, the electromagnetic force, the weak force and gravitation. The four forces and their most significant features are shown in table 1.1.

Three of these forces, the strong, the weak and the electromagnetic force, also called interactions, have been successfully combined in a complete theory. Gravitation could not yet be combined with the other three forces. One can study this force in the frame of a separate theory, called General Relativity. Each element of the theory that includes the three of the four forces is described as a Quantum Field Theory (QFT), a theoretical structure based on the concepts that come from fusing special relativity, quantum mechanics and fields. Gauge theories, such as QFT, suggest that

force	couples with	effect	rel. strength	reach
strong	color charge	binds quarks and gluons	10^0	10^{-15} m
electro-magnetic	electric charge	interaction between el. charged particles	10^{-2}	infinite
weak	weak charge	radioactive decay	10^{-5}	subnuclear
gravitation	mass	attraction of masses	10^{-38}	infinite

Table 1.1: The four fundamental forces in nature and their most important characteristics [1].

symmetry transformations may be performed locally as well as globally. In general, a physical system is described by Lagrangians. In a gauge theory, those Lagrangians are invariant under gauge transformations, i.e., local phase transformations of the fields representing the particles. In order to ensure the invariance of the Lagrangian and compensate for the local change of particle fields, additional fields, called the gauge fields, have to be introduced. In a QFT, the excitations of the gauge fields represent particles transmitting the forces. As stated by the Noether theorem [2], each symmetry implies a conserved current, eventually corresponding to charge conservation. As a result, only particles carrying the charge of a certain force are able to interact via the latter.

The three forces can be described in terms of unitary groups of different dimensions and one can write this combination of gauge groups as $SU(3)_C \bigotimes SU(2)_L \bigotimes U(1)_Y$. The group $SU(3)_C$ is the gauge group of the theory of the strong interactions known as QCD. $SU(2)_L \bigotimes U(1)_Y$ refers to the electroweak theory, which is the successful mixing of the weak nuclear force and electromagnetism. Currently all available experimental data support this gauge theory, also referred to as the Standard Model.

The SM is an elegant mathematical framework based on the QFTs mentioned above, the spin statistic theorem and three elementary symmetries: the Charge, the Parity and the Time reversal (CPT). The SM describes two kinds of particles, the constituents of matter named after the Fermi statistic, usually called fermions, and the carriers of the forces, the gauge bosons, named after the Bose statistic. The Fermi statistic considers particles with spins $s = \frac{1}{2}, \frac{3}{2}, \frac{5}{2}, \ldots$, while the Bose statistic refers to particles with spins $s = 0, 1, 2 \ldots$.

The fermions, shown in table 1.2, consist of quarks and leptons and can be ordered in three generations. One generation differs from another only in the flavor, i.e. the different fermion-types, and the mass of the particles, since all other corresponding quantum numbers are the same. Each generation involves a quark and its weak partner and a lepton and its corresponding neutrino. For every constituent of mat-

ter one also has to consider the existence of its antiparticle. It should be mentioned that the quarks have to carry an additional quantum number in the SM, the color charge. This is of three different types (red, green or blue). Since the color cannot be detected in nature, the quarks must be confined into colorless particles, which are classified into baryons (three quark states), of which most prominent representatives are the proton and the neutron, and mesons (quark-antiquark states). Both baryons and mesons belong to the hadrons, the general category that stands for a bound state of quarks.

generation	fermion	category	symbol	charge [e]	spin	mass [MeV/c^2]
1.	up	quark	u	$\frac{2}{3}$	$\frac{1}{2}$	$1.5 - 3.3$
1.	down	quark	d	$-\frac{1}{3}$	$\frac{1}{2}$	$3.5 - 6.0$
1.	electron	lepton	e	-1	$\frac{1}{2}$	0.5109
1.	e-neutrino	lepton	ν_e	0	$\frac{1}{2}$	$\leq 2 \times 10^{-6}$
2.	charm	quark	c	$\frac{2}{3}$	$\frac{1}{2}$	$1.27^{+0.07}_{-0.11} \times 10^3$
2.	strange	quark	s	$-\frac{1}{3}$	$\frac{1}{2}$	104^{+26}_{-34}
2.	muon	lepton	μ	-1	$\frac{1}{2}$	105.6583
2.	μ-neutrino	lepton	ν_μ	0	$\frac{1}{2}$	≤ 0.190
3.	top	quark	t	$\frac{2}{3}$	$\frac{1}{2}$	$171.2^{+2.1}_{-2.1} \times 10^3$
3.	bottom	quark	b	$-\frac{1}{3}$	$\frac{1}{2}$	$4.20^{+0.17}_{-0.07} \times 10^3$
3.	tau	lepton	τ	-1	$\frac{1}{2}$	1776.84 ± 0.17
3.	τ-neutrino	lepton	ν_τ	0	$\frac{1}{2}$	≤ 18.2

Table 1.2: The fermions ordered in three generations and their properties taken from Reference [3].

The gauge bosons stand for the gauge fields introduced in each of the gauge theories, which the SM consists of. In the quantum gauge theory described by the group $SU(N)$, there end up being $N^2 - 1$ gauge fields. The massless gauge field of this theory is known as the gluon. The group $SU(3)_C$ has eight generators, and this means that there are eight types of gluons predicted by the theory. The case of the remaining $SU(2)_L \bigotimes U(1)_Y$ part of the symmetry group and its gauge bosons is more complicated. Local gauge invariance under the exact symmetry requires all gauge bosons to be massless. However, the observed weak interactions in nature have limited reach, which means that the W^+, the W^- and the Z^0 bosons must have mass. This problem was resolved through the introduction of the Higgs Mechanism [4], which describes the spontaneously breaking of the $SU(3)_C \bigotimes SU(2)_L \bigotimes U(1)_Y$ sym-

metry into the observed $SU(3)_C \bigotimes U(1)_{EM}$. By postulating the existence of a new scalar field, the Higgs field, one is able to construct interactions with the $W^{\pm}$ and the Z bosons, such that they acquire mass. A similar procedure takes place when fermions couple to this field, they become massive. The Higgs field is a scalar complex weak doublet, which yields one new physical scalar particle after electroweak symmetry breaking, the Higgs boson. The Higgs boson has not been experimentally observed yet, but present limits indicate that the mass of the Higgs boson is greater than 114.4 GeV at the 95% confidence level [3], while recent measurements at the Tevatron excluded also the mass range $160-170$ GeV at the 95% confidence level [5]. The relation of the gauge bosons to the three forces and some of their properties are summerized in table 1.3.

force	boson	symbol	el. charge [e]	spin	mass [GeV/c^2]
strong	gluon	g	0	1	0
electromagnetic	photon	γ	$< 5 \times 10^{-30}$	1	$\leq 1 \times 10^{-27}$
weak	W boson	$W^{\pm}$	± 1	1	80.398 ± 0.025
	Z boson	Z^0	0	1	91.1876 ± 0.0021

Table 1.3: The gauge bosons, related to the forces they carry, and some of their properties [3].

When dealing with electroweak processes containing quarks, one has to be aware of the fact that the mass eigenstates are not equivalent to the flavor eigenstates. This was experimentally found and is implemented in the theory by a flavor-mixing matrix. The mass eigenstates d, s, b and the flavor eigenstates $d^{'}$, $s^{'}$, $b^{'}$, which participate in the weak interaction, are related to each other through the Cabbibo-Kobayashi-Maskawa matrix (CKM-matrix) [6]. It is expressed by a 3×3 unitary matrix V_{CKM} as shown in 1.1:

$$\begin{pmatrix} d^{'} \\ s^{'} \\ b^{'} \end{pmatrix} = \begin{pmatrix} V_{ud} & V_{us} & V_{ub} \\ V_{cd} & V_{cs} & V_{cb} \\ V_{td} & V_{ts} & V_{tb} \end{pmatrix} \begin{pmatrix} d \\ s \\ b \end{pmatrix} \tag{1.1}$$

The single elements of this matrix have to be determined experimentally. $V_{q_1 q_2}$ are proportional to the coupling of two quarks q_1, q_2 to a W boson. The current values (90% confidence level) [3] for the different elements $V_{q_1 q_2}$ are given in 1.2.

$$V_{\mathrm{CKM}} = \begin{pmatrix} 0.97419 \pm 0.00022 & 0.2257 \pm 0.0010 & 0.00359 \pm 0.00016 \\ 0.2256 \pm 0.0010 & 0.97334 \pm 0.00023 & 0.0415^{+0.0010}_{-0.0011} \\ 0.00874^{+0.00026}_{-0.00037} & 0.0407 \pm 0.0010 & 0.999133^{+0.000044}_{-0.000043} \end{pmatrix} \tag{1.2}$$

Calculation of Useful Quantities

The strength of an interaction is determined through the corresponding coupling constant. Usually the Lagrangian or the Hamiltonian of a system can be separated into a kinetic part and an interaction part. The coupling constant expresses the strength of the interaction part with respect to the kinetic part, or between two sectors of the interaction part. The interactions between particles can be described by Feynman diagrams in the SM. During the processes the forces couple to the interacting particles and so gauge bosons are emitted and reabsorbed. Such diagrams are shown in section 1.1.2. The diagrams can de translated into a formula by means of the Feynman rules. This formula provides the matrix element $\mathcal{M}$, which is needed for the calculation of the differential cross section or the decay rate of a process, since it provides the crucial information for the transition from one quantum state to another.
In scattering, a differential cross section $\frac{d\sigma}{d\Omega}$ is defined by the probability to observe a scattered particle in a given quantum state per solid angle unit Ω. The total cross section σ, or for simplicity also referred to as the cross section, is the integral of the differential cross section on the whole sphere of observation. A cross section is therefore a measure of the effective surface area seen by the colliding particles, and as such is expressed in units of area. The cross section of two particles colliding with each other is a measure of the interaction event between the two particles. The cross section is proportional to the probability that an interaction occurs.

Another important quantity, is the decay rate $d\Gamma$, also referred to as partial width, of an unstable particle into a specified final state. The calculation is very similar to the one of the differential cross section, while through analogous integration one obtains the partial width Γ, related to the specific final state. The total width Γ_i, also referred to as width, gives a measure of the probability of a particle i decaying to any state. Since a particle may decay into several others, a useful quantity to define, is the branching ratio (BR). BR is defined as the width of a particle decaying to a specific final state over the width of this particle decaying to all possible states the latter is allowed to decay to.

At the Tevatron, protons and antiprotons are accelerated and finally brought to collision. Because of the composite nature of the protons (or antiprotons) stated above, the calculation of a measurable cross section is a complicated enterprise. Considering composite particles like protons, one has to take into account that the momentum of the proton is shared among all the elementary constituent particles, also called partons. Those constituents are usually referred to as the valence quarks, which are bound by virtual gluons. The gluons can split into quark-antiquark pairs, the sea quarks. The valence quarks of the proton, carrying most of its momentum, consist of two up quarks and one down quark. The momentum fraction carried by those partons is being described by the Parton Distribution Function (PDF) $f_i(x_i, Q^2)$, which is defined as the probability density for finding a particle i with a certain longitudinal momentum fraction x_i at momentum transfer Q^2. The latter describes the typical energy scale of the considered interaction, which is usually set

to $Q^2 = m^2_{\text{top}}$ in top-quark physics. Four PDFs at this scale are shown in figure 1.1. One has to convolute the PDFs with the partonic cross sections in order to calculate the measurable cross section in $p\bar{p}$ scattering experiments.

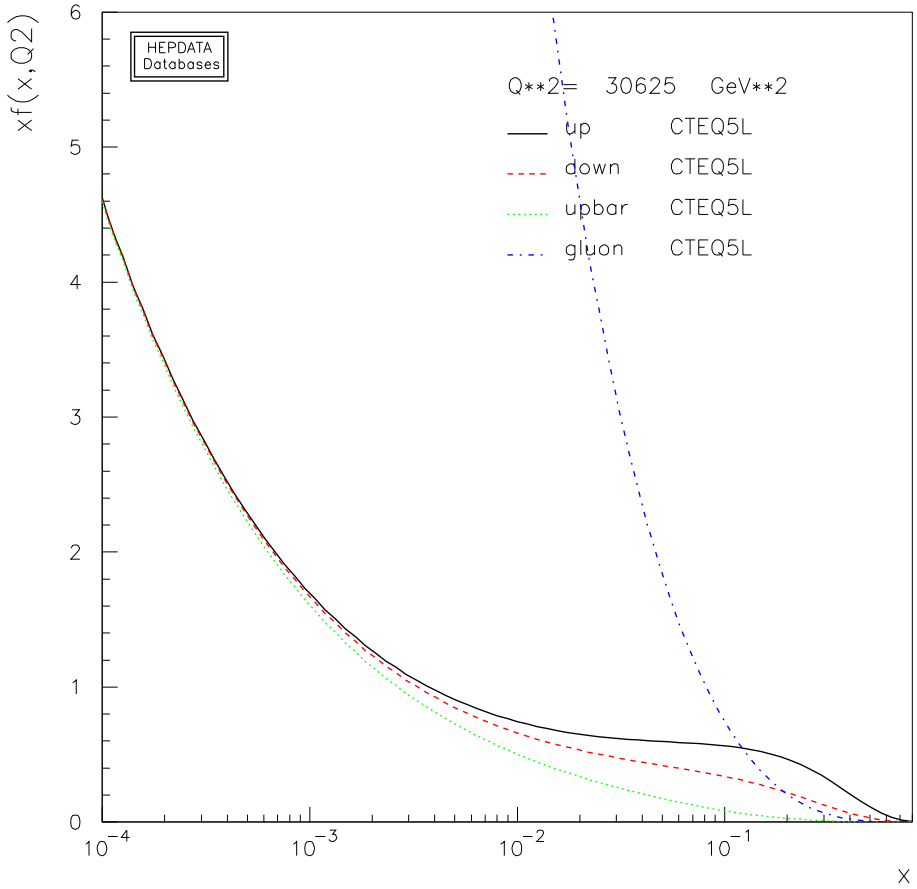

Figure 1.1: The CTEQ5L parton distribution function at Q^2 =(175 GeV/c^2)^2 [7].

1.1.2 Top-Quark Production in the SM

The SM predicts two ways in which a top quark may be produced: top-quark pair-production, also called $t\bar{t}$ production and single top-quark production. A single top-quark may be produced in three different ways: through the W-gluon-fusion, also called t-channel, through the s-channel, also called W^* and in association with an on-shell W-boson. Top-quark pair-production occurs via the strong interaction, while single top-quarks are produced through the electroweak interaction. Both production modes have already been detected at the Tevatron [8, 9, 10, 11, 12].

All direct measurements of production and decay of the top quark have been made by the CDF and DØ experiments in $p\bar{p}$ collisions at the Tevatron. The first studies were performed during Run I, at $\sqrt{s} = 1.8$ TeV, which was completed in 1996. The most recent and highest-statistics measurements are from Run II, which started in

2002 at $\sqrt{s} = 1.96$ TeV. In hadron collisions, top quarks are produced dominantly in pairs through the QCD processes $q\bar{q} \rightarrow t\bar{t}$, see figure 1.2(a) and $gg \rightarrow t\bar{t}$, see figures 1.2(b)-1.2(d). At 1.96 TeV, the production cross section in these channels is expected to be 6.9 ± 0.5 pb [13] for $m_{\rm top} = 175$ GeV/c^2, with a contribution of 85% from $q\bar{q}$ annihilation.

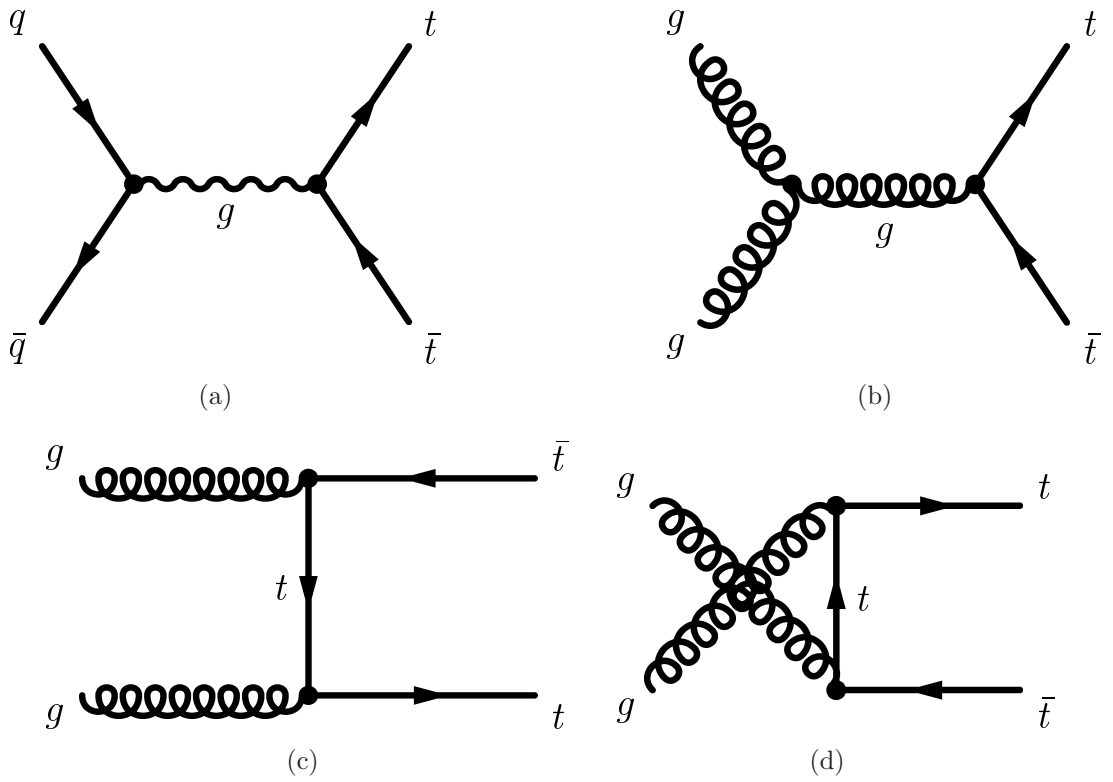

Figure 1.2: (a): Feynman diagram of the top-quark pair-production mode through quark-antiquark annihilation. (b), (c) and (d): Feynman diagrams of the top-quark pair-production mode through gluon fusion.

The combined rate for the single top-quark processes is approximately 3 pb. The expected cross section in the t-channel for $m_{\rm top} = 175$ GeV/c^2 is 2.16 ± 0.12 pb, while in the s-channel one expects a cross section of 0.98 ± 0.04 pb [14]. The identification of top quarks in the electroweak single top-quark channel is much more difficult than in the QCD $t\bar{t}$ channel, due to a less distinctive signature and significantly larger backgrounds. The Feynman diagrams of single top-quark production are shown in figures 1.3(a)-1.3(d). Feynman diagram in figure 1.3(d) is not relevant for the searches at the Tevatron.

The top quark decays almost 100% into a W boson and a bottom quark. This is so, because the Ws and Wd final states are suppressed relative to Wb by the square of the CKM matrix-elements V_{ts} and V_{td}, while $V_{tb} >> V_{ts}, V_{td}$, as shown on 1.2. With a mass above the Wb threshold, and V_{tb} close to unity, the decay width of the top quark is dominated by the two-body channel $t \rightarrow Wb$. The width predicted in

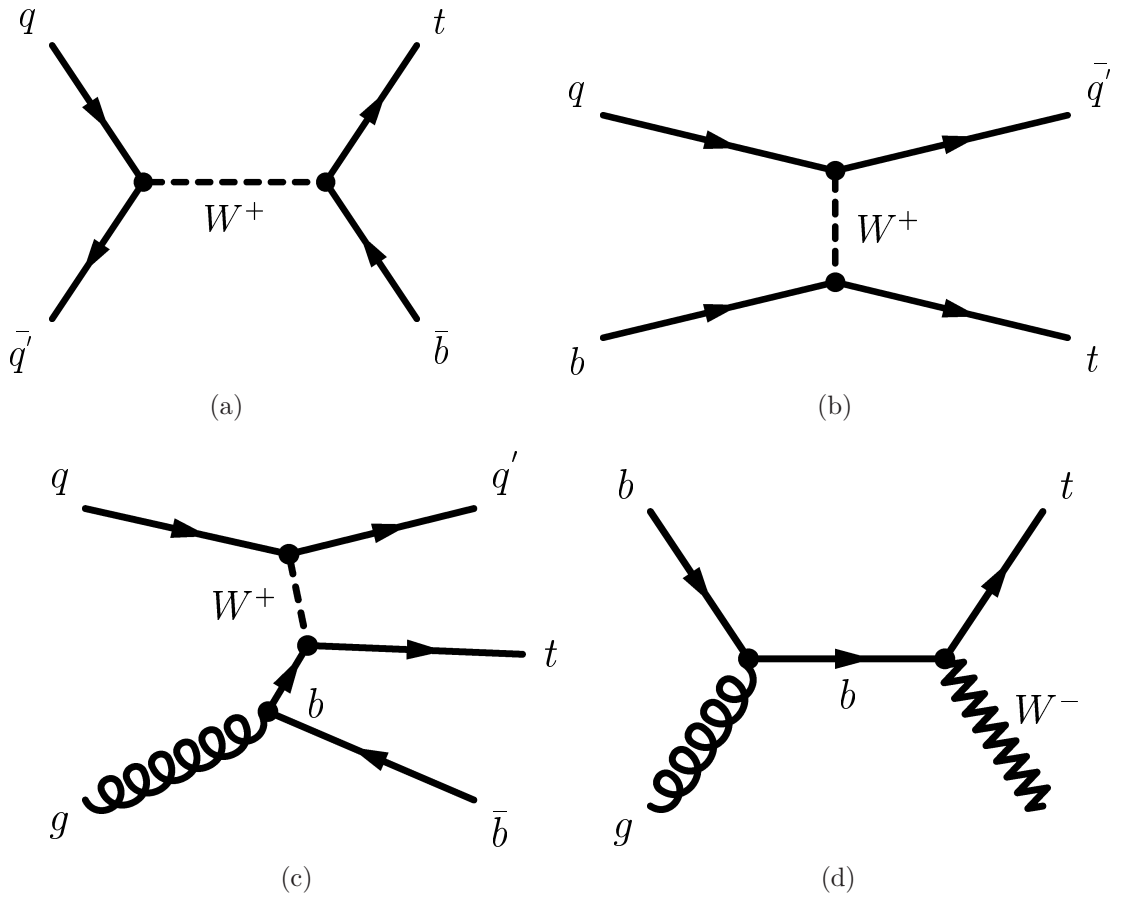

Figure 1.3: (a): Feynman diagram of the s-channel single top-quark production. (b): Leading-order Feynman-diagram of the t-channel single top-quark production. (c): Most important next-to-leading order Feynman-diagram of the t-channel single top-quark production. (d): Feynman diagram for the associated production of a single top-quark and an on-shell W-boson.

the SM at next-to-leading order is:

$$\Gamma_t = \frac{G_F m_{\text{top}}^3}{8\pi\sqrt{2}} \left(1 - \frac{M_W^2}{m_{\text{top}}^2}\right)^2 \left(1 + 2\frac{M_W^2}{m_{\text{top}}^2}\right) \left[1 - \frac{2\alpha_s}{3\pi}\left(\frac{2\pi^2}{3} - \frac{5}{2}\right)\right], \quad (1.3)$$

where G_F is the Fermi coupling constant, M_W is the mass of the W boson, α_s is the strong coupling constant and m_{top} refers to the top quark pole mass. With its correspondingly short lifetime of $\approx 0.5 \times 10^{-24}$ s, the top quark decays before top-flavored hadrons or $t\bar{t}$-quarkonium bound-states can form.

1.1.3 Flavor-Changing Neutral Currents in the SM

FCNC (Flavor-Changing Neutral Currents) stands for an interaction, in which a quark flavor in the initial state changes to another in the final state, while its charge remains the same. The SM does not contain tree-level FCNC, though they can occur at higher order through radiative corrections. But even at next-to-leading order, FCNC are suppressed, mainly due to the GIM mechanism [15]. The latter is named after the initials of Glashow, Iliopoulos and Maiani, who postulated it. In the bottom-quark sector, the large top-quark mass alleviates the GIM-suppression leading to FCNC decays with branching ratios (BR) at the level of 10^{-6} , while in the top-quark sector, FCNC decays are more strongly suppressed and occur only at the order of BR $\approx 10^{-14} - 10^{-10}$. A typical Feynman diagram describing such processes is shown in figure 1.4, also called 'penguin' diagram.

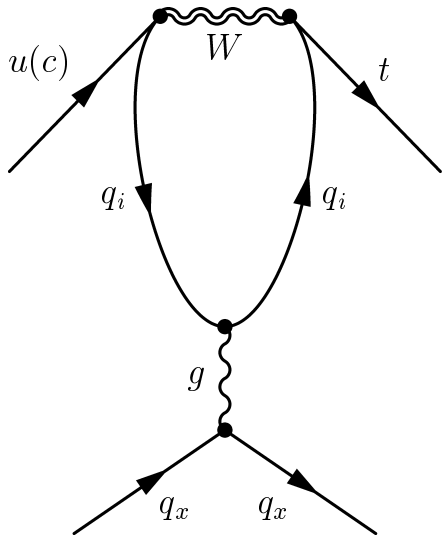

Figure 1.4: Feynman diagram of the FCNC interaction $u(c) + g \rightarrow t$ as expected in the SM. q_i stands for d, s, b, while q_x stands for all quark flavors.

1.2 Beyond SM Physics

The top quark is very heavy, with a mass about 40 times that of the next heaviest quark in the SM, the bottom quark. For this reason it is a likely place to search for new physics. If new physics is found in the top-quark sector, it is possible that this could explain why the top is so heavy and how its mass is generated. This could in turn provide us with clues as how the other quark masses arise, which is a question the SM makes no effort to adress. Perhaps there is new physics specific

to the third family, physics which can explain why the top quarks, bottom quarks and tau lepton are so much heavier than their first and second family counter parts. In addition, there could be new interactions that are not really involved in producing the large masses, but coupling more significantly to particles with large mass, and thus can be detected by studying the top quark, while only affecting the other quarks insignificantly.

1.2.1 Questions concerning the SM

Even if the SM explains and predicts many processes in nature, it is already known that the model is incomplete. Many fundamental questions remain unanswered and the SM seems to be unable of answering them, at least based on the structure it has today. One of the problems has already been mentioned and refers to the implementation of gravity in the SM. A promising quantum field theory for gravitation has not yet been accomplished. Because gravitation is a very weak force on small scales, it is also difficult to make experimental tests. On the other hand, the electromagnetic force and the weak force have been successfully combined to the so-called electroweak force in the frame of the GWS-theory, named after the theorists Glashow, Weinberg and Salam. This theory requires the existence of a new particle, the Higgs boson, which has not yet been found. In case that it won't be discovered in the future, one should be looking for alternative theories. Even if the Higgs boson will be detected and the electromagnetic force proves to be compatible with the weak force, there is still no guarantee that combining subsequently the strong force with the electroweak force will be possible. Furthermore, the SM has problems in predicting the masses of particles, in fact it makes no predictions about them at all. Moreover, the question why the weak force is 10^{32} times stronger than gravity (hierarchy problem) remains unexplained, which is correspondent to the question why the Higgs boson mass is so small compared to the grand unification scale. One would also ask oneself why there have to be three generations of fermions, since the matter in the world seems to be consisting of the particles of just the first generation. Another universal problem is the discrepancy in the abundances of matter and antimatter. The current amount of CP violation is not enough to motivate it. Nevertheless, one crucial matter which has been paid attention to by the physisists and still remains unsolved, is the nature of the dark matter and the dark energy, which are considered to make up most of the energy density of the known universe. Dark matter refers to observed phenomena which include the rotational speeds of stars in galaxies, orbital velocities of galaxies in clusters, gravitational lensing of background objects by galaxy clusters and the temperature distribution of hot gas in galaxies and clusters of galaxies. Dark energy was postulated in order to explain recent observations that the universe appears to be expanding at an accelerating rate. The SM has no candidate constituents which could fit in the pattern of these astronomical observations. Considering all the above points, one comes to the conclusion that extensions to the SM in the near future will be inevitable.

1.2.2 Anomalous Top-Quark Production via FCNC

As already discussed in section 1.1.3, the FCNC effects are expected to be small in the SM. However, anomalous couplings could lead to enhancements of FCNC in the top sector and their observation would be a clear sign of new physics [16]. It has been argued that anomalous FCNC couplings may be significant in many extensions to the SM, such as:

- supersymmetry (SUSY) [17, 18]
- other models with multiple Higgs doublets [19]-[27]
- models with new dynamical interactions of the top quark [28, 29]
- models where the top quark has a composite structure [30]
- models where the top quark has a soliton structure [31, 32].

It has been suggested that supersymmetric contributions to such couplings may be large enough to be measured at a more powerful hadron collider, e.g. the LHC [33, 34]. For instance, the branching ratio $BR(t \to cg)$ is expected to be at the level of $\approx 10^{-4}$ in the unconstrained Minimal Supersymmetric Standard Model (MSSM), while in the R-parity violating MSSM, the same BR is at the level of $\approx 10^{-3}$ [18]. In the analysis presented in this thesis, the FCNC chromomagnetic operators will be examined in a model-independent way using direct top-quark production at the Fermilab Tevatron.

1.2.3 Model Independent Approach through an Effective Theory

In order to study the anomalous FCNC coupling it is not necessary to create a whole new theory. One may incorporate new physics in the SM considering an effective Lagrangian [35, 36]:

$$\mathcal{L}_{eff} = \mathcal{L}_0 + \mathcal{L}_1 \tag{1.4}$$

where $\mathcal{L}_1$ contains operators of dimension higher than four, multiplied by coefficients with appropriate dimensions of mass to insure that the dimension of the Lagrangian as a whole remains four. Since the resultant theory is not valid to an arbitrarily high energy scale, it is not a fundamental physical theory. Instead, it represents a theory that is 'effective' at a lower energy scale where the energy is too low to allow us to see the full details of the underlying physics.

For energies above the mass cut-off scale, the effective theory breaks down.

We consider here the possibility of a flavor-changing gluonic current. In this case, $\mathcal{L}_0$ will be the QCD Lagrangian, given by

$$\mathcal{L}_0 = -\frac{1}{4}G^a{}_{\mu\nu}G^{a\mu\nu} + \bar{q}i\gamma^\mu D_\mu q - m_q\bar{q}q \tag{1.5}$$

where $D_\mu = \partial_\mu - ig_s\frac{\lambda^a}{2}G^a{}_\mu$ is the covariant derivative and $G^{a\mu\nu}$ is the gauge field-tensor of the gluon. In the scenario that is considered in this thesis, an up quark, or a charm quark, and a gluon from the colliding hadrons combine to form an s-channel top quark, which then decays. In that case, $\mathcal{L}_1$ is defined as follows:

$$\mathcal{L}_1 = \frac{g_s\kappa_{gtu}}{\Lambda}[\bar{u}\sigma^{\mu\nu}\frac{\lambda^a}{2}tG^a{}_{\mu\nu} + h.c.] \tag{1.6}$$

where κ_{gtu} is a dimensionless parameter that relates the strength of the 'new coupling' to the constant g_s. Λ is the new physics scale, related to the mass cut off scale above which the effective theory breaks down. λ^a are the Gell-Mann matrices, and $\sigma^{\mu\nu} \equiv \frac{i}{2}[\gamma^\mu, \gamma^\nu]$ transforms as a tensor under the Lorentz group. The parton cross-section for direct top-quark production is given by [36]:

$$d\sigma = \frac{1}{4}\frac{1}{(4\pi)^5}\frac{\hat{s} - M^2_{\ell,\nu_\ell}}{\hat{s}^2}|\bar{\mathcal{M}}|^2 d\Omega_b d\Omega_\ell dM^2_{\ell,\nu_\ell}, \tag{1.7}$$

where the spin-averaged squared matrix-element is

$$\begin{aligned}|\bar{\mathcal{M}}|^2 &= \frac{256\pi^3\alpha^2\alpha_s}{3\sin^4\theta_W}\frac{\kappa^2_{gtu}}{\Lambda^2} \\ &\times \frac{\hat{s}\,(p_b\cdot p_{\nu_\ell})\left[\hat{s}\,(q_u\cdot p_\ell) + m^2_{\text{top}}\,(q_g\cdot p_\ell)\right]}{\left[\left(\hat{s} - m^2_{\text{top}}\right)^2 + m^2_{\text{top}}\Gamma^2_t\right]\left[\left(M^2_{\ell,\nu_\ell} - M^2_W\right)^2 + M^2_W\Gamma^2_W\right]}.\end{aligned} \tag{1.8}$$

The quantities p_{b,ℓ,ν_ℓ} are the four-momenta of the outgoing bottom quark, lepton and neutrino respectively, $q_{u,g}$ are the four-momenta of the incoming up quark and gluon. Γ_W is the decay width of the W boson, $\sqrt{\hat{s}}$ is the parton center-of-mass energy, α is the fine-structure constant, θ_W is the weak mixing angle, also known as Weinberg angle, while Γ_t is defined as follows:

$$\Gamma_t = \Gamma_{t\to bW}\times\left[1 + \frac{128M^2_W\alpha_s}{3\alpha^2\left(1 - \frac{M^2_W}{m^2_{\text{top}}}\right)^2\left(1 + 2\frac{M^2_W}{m^2_{\text{top}}}\right)}\left(\frac{\kappa^2_{gtu}}{\Lambda^2}\right)\right], \tag{1.9}$$

where $\Gamma_{t\to bW}$ is the SM top-quark decay-width to a bottom quark and a W boson, given by

$$\Gamma_{t\to bW} = \frac{G_F m^3_{\text{top}}|V_{tb}|^2}{8\pi\sqrt{2}}\left[1 - \frac{M^2_W}{m^2_{\text{top}}}\right]^2\left[1 + 2\frac{M^2_W}{m^2_{\text{top}}}\right]. \tag{1.10}$$

The squared invariant mass of the charged lepton and the neutrino M^2_{ℓ,ν_ℓ} is defined as

$$M^2_{\ell,\nu_\ell} \equiv (p_\ell + p_{\nu_\ell})^2, \tag{1.11}$$

where M^2_{ℓ,ν_ℓ} is not necessarily equal to the on-shell mass of the W boson. The analogous expressions to equations 1.6, 1.8 and 1.9 for the *gtc*-coupling are implied. One could hope to learn about these anomalous FCNC couplings both by studying single top-quark production and decays. However, it brings us back to the problem of using top-quark decays to determine the magnitude of a coupling. The decay can provide information about the relative branching fraction of the exotic decay compared to the SM top-quark decay $t \to W^+b$, but since it does not allow one to measure the top-quark decay-width, it cannot provide a limit on the size of the exotic operator without first making an assumption concerning the nature of the Wtb interaction.
New physics contributions to single top-quark production would scale as $\left(\sqrt{\hat{s}}/\Lambda\right)^n$ where n is a positive integer or zero [37]. On the other hand, top-quark decay-processes scale as $(m_{\text{top}}/\Lambda)^n$. At high energy colliders such as the Tevatron, $\sqrt{\hat{s}}$ can be considerably larger than m_t, thus enhancing the relative importance of new physics in single top-quark production. While the $t \to ug$ decay will occur in the presence of the anomalous couplings given in equation 1.6, see figures 1.6(a) and 1.6(b), it is negligible compared to the $t \to bW$ decay for κ/Λ values of a few tenth of TeV^{-1}. In reference [38] the *gtc*–coupling strength κ_{gtc} is studied by examining the decay of the top quark into a charm quark and a gluon. It is found that an upper limit on κ_{gtc} of 0.43 TeV^{-1} for 200 pb^{-1} of data could be measured at the Tevatron. If the c and the u jets are not distinguished, their result applies equally well to κ_{gtu}/Λ, if one uses the up quark coupling alone.

When the W boson decays into a charged electron or muon and its corresponding neutrino, it has an experimentally identifiable signature and only the $t \to bW \to b\ell\nu_\ell$ decay will be considered for the signal. Figure 1.5 shows the Feynman diagram for direct top-quark production and subsequent decay into $b\ell\nu_\ell$.

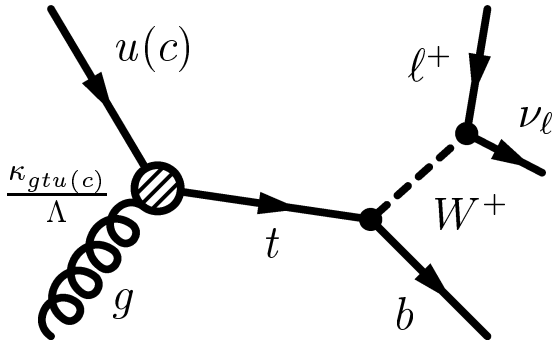

Figure 1.5: Feynman diagram for direct anomalous top-quark production and subsequent decay into $b\ell\nu_\ell$.

In figures 1.6(c) and 1.6(d), the dependance of the anomalous top-quark production cross sections on the coupling strengths is demonstrated. Three different orders of calculation are shown in each plot, leading order (LO), next-to-leading order (NLO) and resummation (Resum) [34].

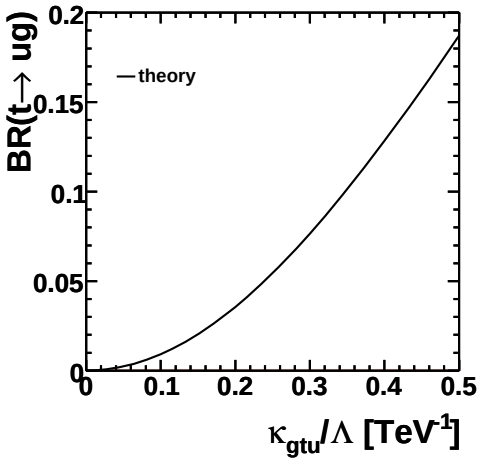

(a) $t \to ug$

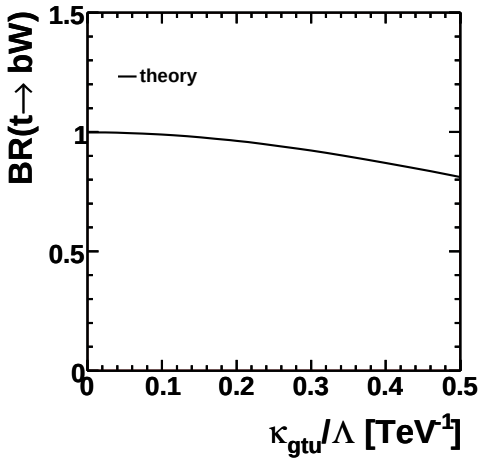

(b) $t \to bW$

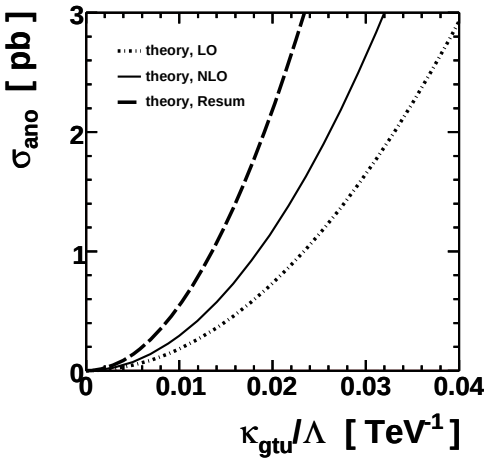

(c) $\sigma_{ano} \propto {\kappa_{gtu}}^2$

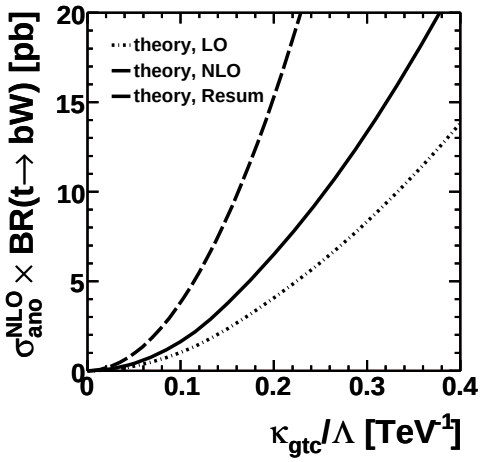

(d) $\sigma_{ano} \propto {\kappa_{gtc}}^2$

Figure 1.6: Motivation for searching in the SM top-quark decay channel, while studying the anomalous top-quark production: the branching ratio of the anomalous top-quark decay (a) is negligible compared to the SM top-quark decay (b) in the region $\kappa/\Lambda \lesssim 0.2$ TeV^{-1}, while the anomalous top-quark production (c), (d) is significant. The upper two plots are showing the branching ratios in LO calculation, whereas the lower two plots are showing the anomalous top-quark production cross sections in three different orders of calculation, leading order (LO), next-to-leading order (NLO) and resummation (Resum).

This analysis is the first one at the Tevatron searching for the $2 \rightarrow 1$ processes $u(c) + g \rightarrow t$, while a previous analysis [39] by the DØ collaboration has looked for $2 \rightarrow 2$ processes, such as $q\bar{q} \rightarrow t\bar{u}$, $ug \rightarrow tg$, and $gg \rightarrow t\bar{u}$, resulting in the best upper limits on the anomalous gtu and gtc couplings to date: $\kappa_{gtu}/\Lambda < 0.037$ TeV^{-1} and $\kappa_{gtc}/\Lambda < 0.15$ TeV^{-1} at the 95% C.L.. Given the existing upper bound of the anomalous coupling, $t \rightarrow bW$ will be the dominant decay mode of the top quark, see figure 1.6.

All four experiments at LEP and two of the experiments at HERA have searched for anomalous single top-quark production via FCNC. The ALEPH collaboration have searched in $e^+e^- \rightarrow \bar{t}c, \bar{t}u$ and set the limits $BR(t \rightarrow Zc) + BR(t \rightarrow Zu) <$ 14%, for $BR(t \rightarrow \gamma c) + BR(t \rightarrow \gamma u) = 0$ and $m_{\text{top}} = 174$ GeV/c^2 [40]. The DELPHI collaboration has searched in $e^+e^- \rightarrow t\bar{c}$ and give the following limits on the anomalous coupling constants: $\kappa_Z(\kappa_\gamma = 0) = 0.434$ and $\kappa_\gamma(\kappa_Z = 0) = 0.505$ for $m_{\text{top}} = 175$ GeV/c^2 and $\Lambda = 175$ GeV [41]. In addition, the L3 collaboration, searching for $e^+e^- \rightarrow t\bar{c}/t\bar{u}$ reactions, too, find $\kappa_Z = 0.37$, $\kappa_\gamma = 0.43$, $BR(t \rightarrow Zq) < 13.7\%$ and $BR(t \rightarrow \gamma q) < 4.1\%$ for $m_{\text{top}} = 175$ GeV/c^2 and Λ near the TeV-scale [42]. The OPAL collaboration argue their limits to be consistent with the search by the ALEPH collaboration, by presenting the following limits at the same top-quark mass range: $BR(t \rightarrow Zc) + BR(t \rightarrow Zu) < 13.7\%$, $\kappa_\gamma = 0.48$ and $\kappa_Z = 0.41$ at 95% C.L. [43]. Furthermore, the H1 Collaboration searched in $ep \rightarrow e + t + X$ reactions and was able to set a limit of 0.27 on $\kappa_{tu\gamma}$ at 95% C.L. [44], while the ZEUS Collaboration managed to improve the exclusion limit up to 35% ($\kappa_{tu\gamma} < 0.174$) at 95% C.L. [45].

FCNC couplings to the top quark involving the Z boson have been constrained by the analysis of top-quark decays at the Tevatron [46]. The limit given on the branching ratio is $BR(t \rightarrow Zq) < 3.7\%$ at 95% C.L. for $q = u, c$.

Chapter 2

Experimental Facilities

This chapter describes the experimental facilities used to collect the data analyzed in this doctor thesis. The Collider Detector at Fermilab (CDF) experiment is hosted by the Fermi National Accelerator Laboratory.

2.1 The Fermi National Accelerator Laboratory

The Fermi National Accelerator Laboratory (FNAL), also known as Fermilab, is located in Batavia, Illinois (USA), in a distance of about 70 km from Chicago. It covers an area of about 27.5 km^2. Much of what we know about matter and energy and even how the universe began was discovered there over the last four decades. Various experiments advanced the understanding of matter with the discovery of the bottom quark (1977), the top quark (1995) and the tau neutrino (2000). Fermilab is home to the world's most powerful fully operational particle accelerator, the Tevatron. An aerial view of the Fermilab site is shown in figure 2.1.

2.1.1 The Tevatron Accelerator Chain

In order to reach energies of 980 GeV per beam, a system of several accelerators is needed. Figure 2.2 gives a schematic overview of these accelerators. In the first stage of acceleration, the Cockcroft-Walton pre-accelerator is used to generate negative charged hydrogen ions out of hydrogen gas and then accelerate them via electric fields up to an energy of 750 keV. Afterwards, the ions enter an approximately 150 m long linear accelerator (LINAC), where they are accelerated up to 400 MeV by oscillating electric fields. Before leaving this acceleration stage, the ions pass through a carbon foil, which removes their negative charges (electrons), so that only protons remain to be promoted to the next level. Further on, the beam of protons is bent in a circular path by the magnets of a circular accelerator, called the Booster. On its way out of the Booster, the beam has an energy of 8 GeV. In the next stage, the protons enter the Main Injector, a multitask-accelerator completed in 1999.

Figure 2.1: Aerial shot of the Fermilab site. Two rings of the accelerator system, the Tevatron and the Main Injector, can be seen.

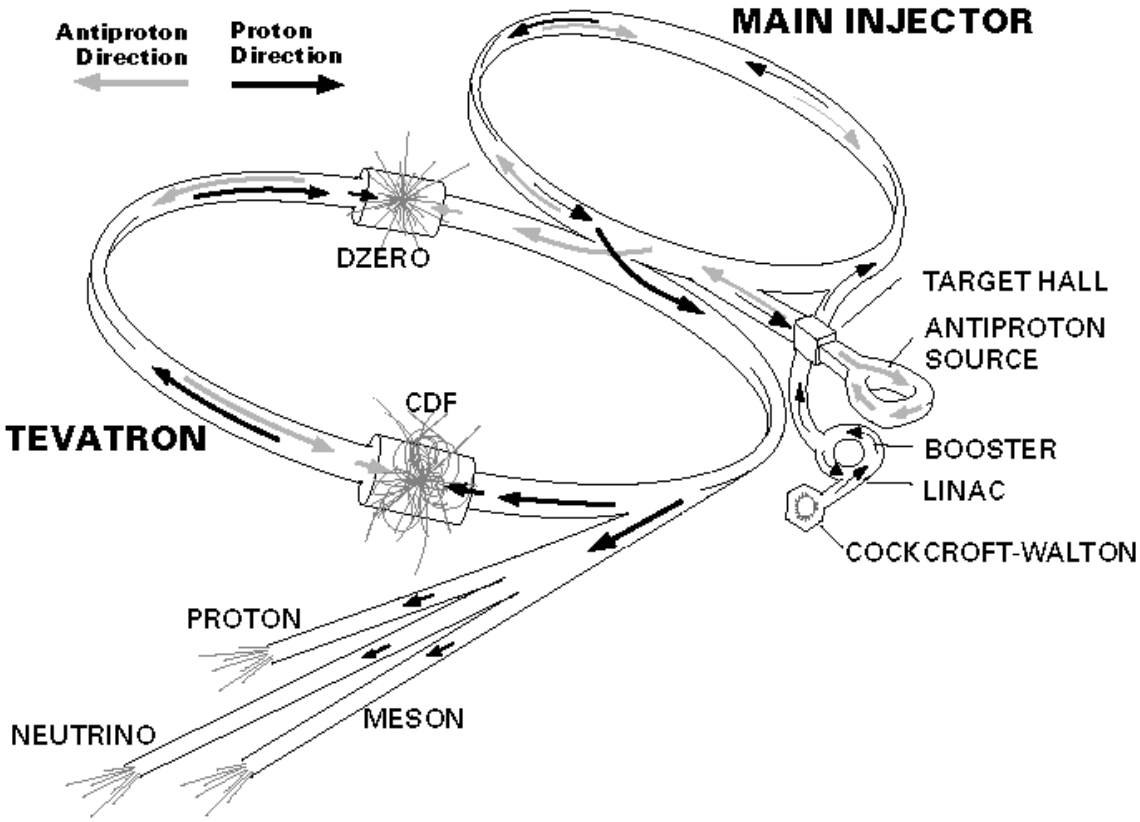

Figure 2.2: Schematic view of Fermilab's accelerators for Run II.

This machine accelerates protons up to 150 GeV, while protons with 120 GeV are used for antiproton production. The latters are forced to collide with a nickel target, which is installed at the Antiproton Source facility. The interactions with the target produce a variety of particles, among them antiprotons, which are being collected, focussed and finally stored in the Accumulator Ring.

From the Antiproton Source, the antiprotons are sent to the Recycler which is located along the ceiling of the Main Injector. The proposed purpose of the Recycler was to recycle antiprotons from the Tevatron, cooling and storing them alongside those from the Antiproton Source. Those plans have been abandoned due to early problems in Run II. The Recycler now accepts transfers only from the Antiproton Source and cools the antiprotons further than the Accumulator is capable. In addition to stochastical cooling, electron cooling is necessary for higher intensities. Electron cooling works on the principle of momentum transfer between electrons and antiprotons of the same average velocity. The antiproton beam is overlaid with a 4.3 MeV electron beam traveling about 20 m along the same path in the Recycler. Coulomb scattering leads to energy transfer from the antiprotons to the co-streaming electrons until thermal equilibrium is attained. After cooling the so-called "stash", the antiprotons are mined into nine parcels, each split into four bunches.

To prepare the final injection to the Tevatron main ring, i.e during the so-called "shot setup", seven bunches of 8 GeV protons are transferred from the Booster to the Main Injector and accelerated to 150 GeV. After being coalesced to one bunch, the protons are shot into the Tevatron ring. This procedure is repeated 36 times. After transferring all proton bunches to the Tevatron ring, four antiproton bunches are extracted from the Recycler and accelerated to 150 GeV in the Main Injector before they are shot into the Tevatron. This procedure is repeated nine times, leading to a 36×36 bunch structure of the Tevatron beam.

In the final stage, the proton and antiproton beams with 150 GeV energy are injected in the Tevatron, a circular accelerator with a circumference of about 6 km. Each beam is accelerated to an energy of 0.98 TeV which is equal to (anti)protons reaching velocities of 0.9999995 times the speed of light. At two certain points of the facility these beams are forced to collide with each other, producing a center of mass energy of $\sqrt{s} = 1.96$ TeV. At each of those two collision points, a detector is placed in order to collect data from the products of the collision. One of these detectors is the CDF II experiment, which is also where the data for this analysis originates from. The other detector is called DØ, also indicated in Figure 2.2. The time interval between the filling of the Tevatron with protons and antiprotons and the dumping of the beams is called a store.

2.1.2 Luminosity

The instantaneous luminosity $\mathcal{L}$ is a measure of the ability of an accelerator to produce collisions, specifically the chance that a proton will collide with an antiproton. It is given by:

$$\mathcal{L} = n \cdot f \cdot \frac{N_p N_{\bar{p}}}{4\pi\sigma_x\sigma_y}, \tag{2.1}$$

where n is the number of bunches, f is the revolution frequency, N_p ($N_{\bar{p}}$) is the number of protons (antiprotons) per bunch, and σ_x and σ_y represent the average transverse width of the bunches. $\mathcal{L}$ is measured in units of $\mathrm{cm}^{-2}\mathrm{s}^{-1}$, typifying a particle flux.

The instantaneous luminosities achieved by the Tevatron have been steadily increasing. This is shown in figure 2.3, where the instantaneous peak luminosities of every store of Run II are presented.

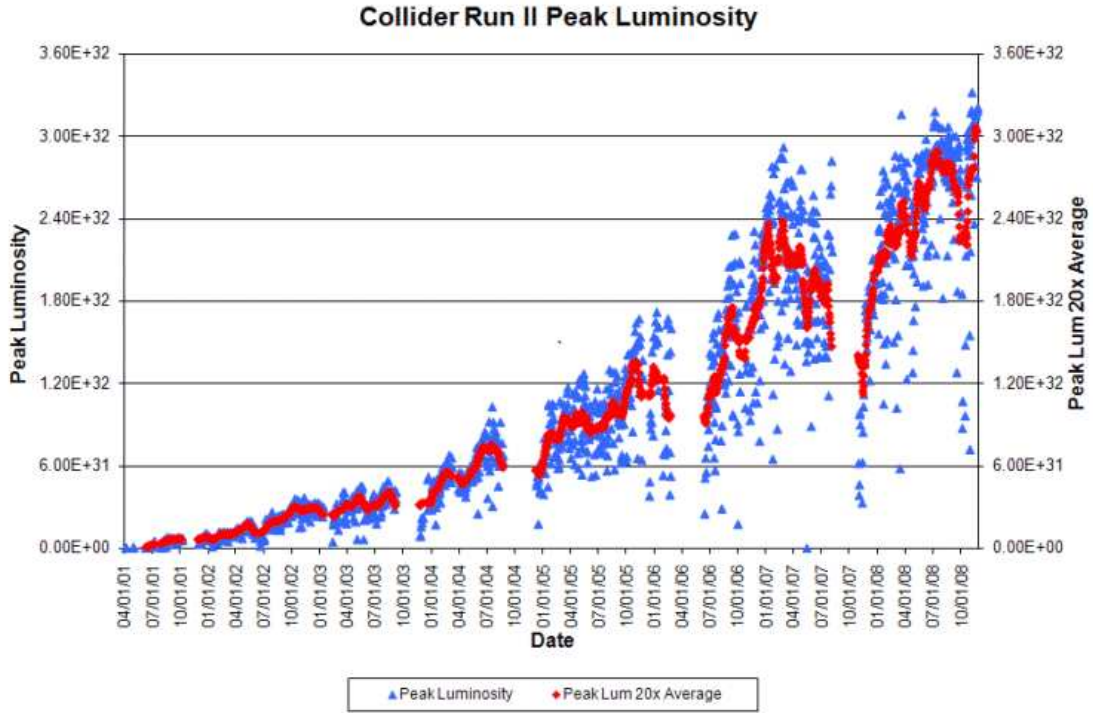

Figure 2.3: Peak luminosity per store since the start of Run II.

The maximum luminosity is reached at the beginning of a store because the number of protons and antiprotons diminishes during collisions, leading to an exponential decrease in luminosity. The luminosity delivered per calendar year is illustrated in figure 2.6(b). At the beginning of Run II, the initial luminosities were rather small but increased with improved understanding and handling of the accelerators. The design luminosity [47] was reached in Winter 2006/2007, the current record luminosity is $370 \cdot 10^{30}$ $\mathrm{cm}^{-2}\mathrm{s}^{-1}$ (January 2009).
Integrating the instantaneous luminosity over time gives the so-called integrated luminosity, $\mathcal{L}_{\mathrm{int}} = \int \mathcal{L}\mathrm{d}t$, which is a measure of the amount of collected data. To calculate the event rate of a certain physics process, the probability of the process

occurring is essential. This probability, the cross section σ, is usually given in cm^2. In particle physics, cross sections are preferably quoted in picobarn (pb), where 1 pb = 10^{-36} cm^2. For a particular cross section, the number of events N in a given amount of data can be calculated by $N = \sigma \cdot \mathcal{L}_{\text{int}}$. The measurement of the luminosity is done with low mass Čerenkov detectors, so called Čerenkov Luminosity Counters (CLC) [48]-[50].

The design of the CLC is optimized to detect primary particles coming from the interaction point in $p\bar{p}$ inelastic collisions and to be as insensitive as possible to secondary particles which contribute significantly to the uncertainty in the measurement. A single detector element consists of a 2 meter long cone made of aluminized mylar with a light collector attached to one end directing the Čerenkov light onto the face of a photomultiplier (PMT) with quartz window. As a radiator isobutane is used, because it has one of the largest indexes of refraction at atmospheric pressure for commonly available gases and good transparency for photons in the ultra-violet region where most of the Čerenkov light is emitted. The Čerenkov light-cone half-angle is 3.1° and the momentum threshold for light emission is 9.3 MeV/c for electrons and 2.6 GeV/c for pions. Prompt particles coming from the $p\bar{p}$ interactions traverse the full length of the counter and generate a large amplitude PMT signal ($\sim$ 100 photoelectrons). The full luminosity monitor system consists of 48 such conical counters per side arranged in three layers of 16 counters each for a total of 96 channels. The counters are located inside the 3-degree hole and point to the counter of the CDF II detector as shown in figure 2.4 and cover the $3.7 < |\eta| < 4.7$ range. Figure 2.5 shows the components of the CLC detector.

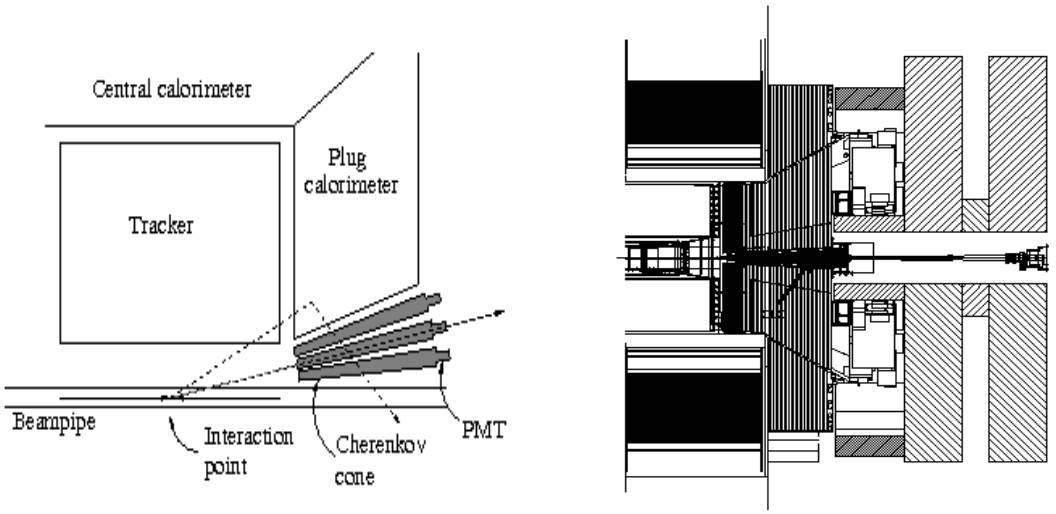

(a) (b)

Figure 2.4: (a): Schematic view of the luminosity monitor inside a quadrant of CDF. (b): The Čerenkov Luminosity Counters in CDF.

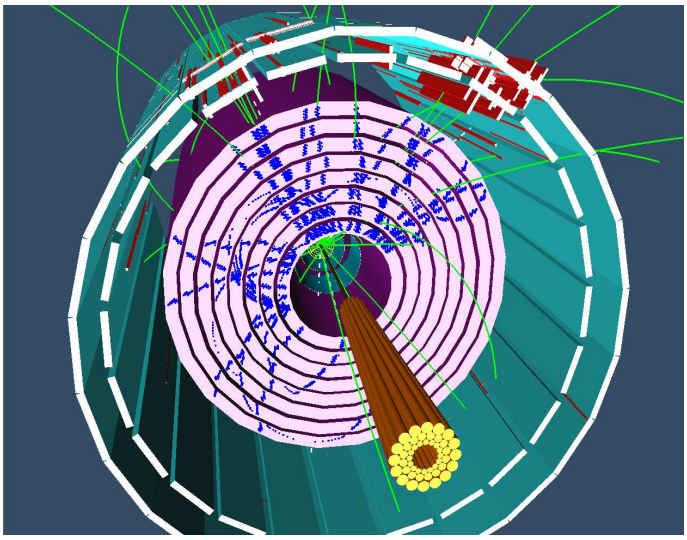

(a)

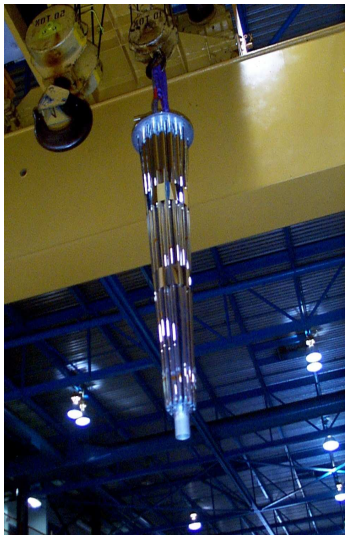

(b)

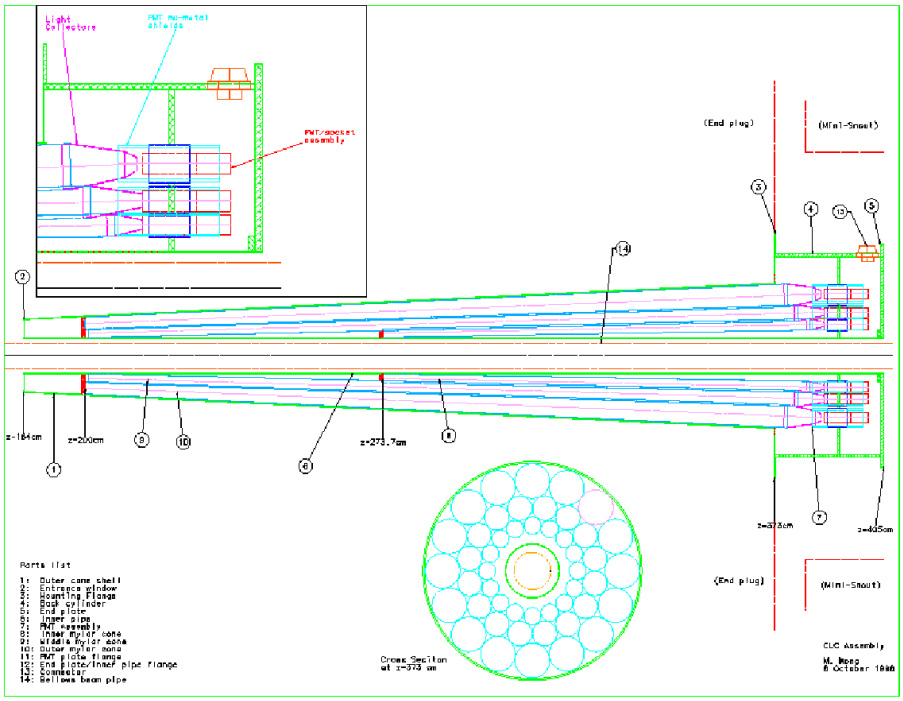

(c)

Figure 2.5: (a): Location of the CLC detector in 3D simulation. (b): A picture of the CLC detector. (c): Schematic view of the CLC detector.

In order to measure the luminosity for Run II effectively, two separate schemes are used, the timing and the amplitude measurement. Both schemes attempt to estimate the average number of interactions in a given crossing.
The main role in the timing based algorithm plays the precise timing to count the number of time clusters in the Čerenkov detector. Particles from each interaction arrive at the same time in the counters. These time clusters are counted offline and so the number of interactions for that particular bunch crossing can be determined on average. Online, the number of hit channels is counted in order to provide a quick measurement of luminosity. The latter option works well for low luminosities. In the amplitude based algorithm, the main role plays the counting of the number of particles from the interaction region that hit the counters. This is very different from counting hits because hits come from all sources, including secondaries from the beam pipe and plug and halo particles. In order to count primary interactions a resolution good enough to distinguish the peaks of a single, double and triple interaction in the counters is needed. Online, this is obtained by summing up the amplitudes above certain thresholds, while offline the single PMT amplitudes can be directly accessed. The CLC detector is designed to reliably perform bunch-by-bunch luminosity measurements at peak instantaneous luminosities of $2 \cdot 10^{32}$ cm^{-2}s^{-1} with 6 interactions per bunch crossing, on average, and respond to a 132 ns bunch spacing.

Figure 2.6 illustrates the development of $\mathcal{L}_{\text{int}}$ over time. Up to date (January 2009), the Tevatron delivered about 5.3 fb^{-1} whereof CDF II managed to record approximately 4.4 fb^{-1}, leading to an average data taking efficiency of 83%, which is shown on figure 2.6(c). The data used in the analysis described in this thesis were taken from March 2002 (store 1120) until August 2007 (store 5592) and correspond to an integrated luminosity of 2.2 fb^{-1}, see figure 2.6(a).

2.2 The Collider Detector at Fermilab

More than 60 institutes in 12 countries build the collaboration maintaining the Collider Detector at Fermilab. The only German partner in this collaboration is the *Institut für Experimentelle Kernphysik* in Karlsruhe. Figure 2.7 shows the detector.

The CDF II detector is placed at one of the two interaction points at the Tevatron, to be more specific at interaction point B0. CDF II is an azimuthally and forward-backward symmetric general-purpose solenoid detector [51]. It is designed to detect the resulting particles of the collisions, this means to track the charged particles and to measure the momentum and the energy of all the particles interacting with the detector material. Figure 2.8 shows a cutaway view of the CDF II detector with its various components. It consists of the tracking system, the calorimeter system and outermost the muon system. All the above systems, as well as the trigger system, are explained in detail in sections 2.2.1, 2.2.2, 2.2.3, and 2.2.4, respectively.

The detector is described using a cylindrical coordinate system. The z-axis is set along the proton beam, while the polar angle θ is defined with respect to the proton beam direction and the azimuthal angle ϕ with respect to the outgoing radial

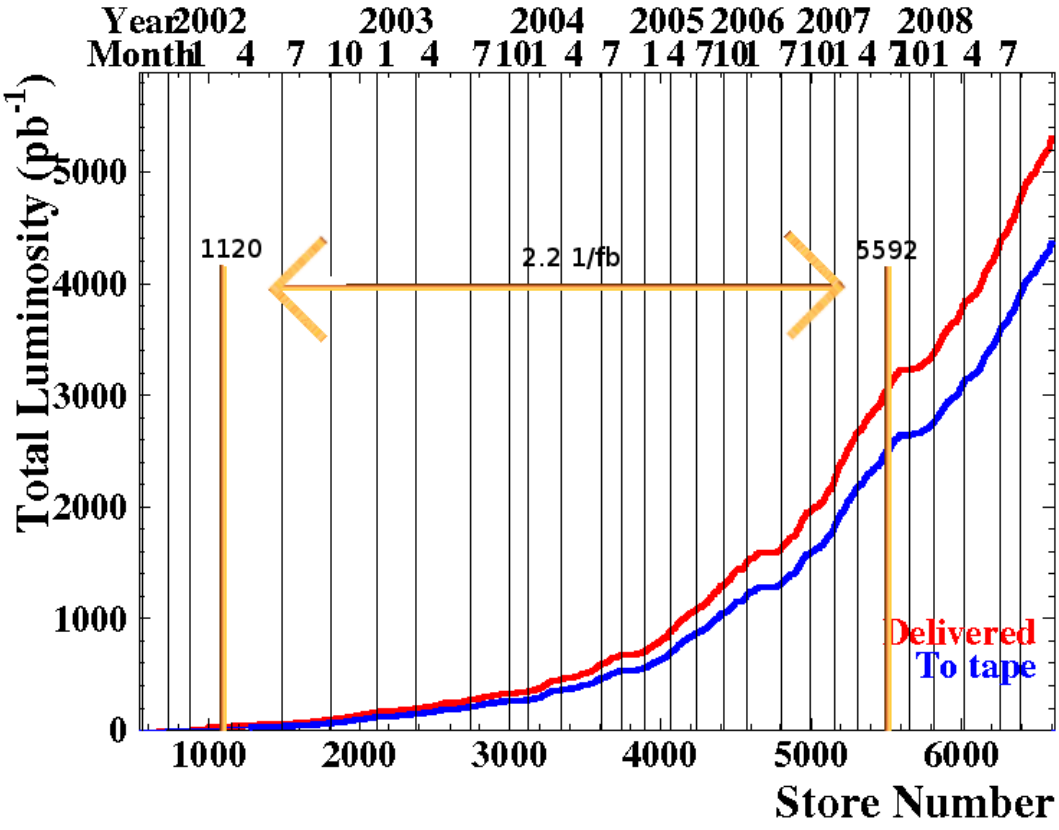

(a)

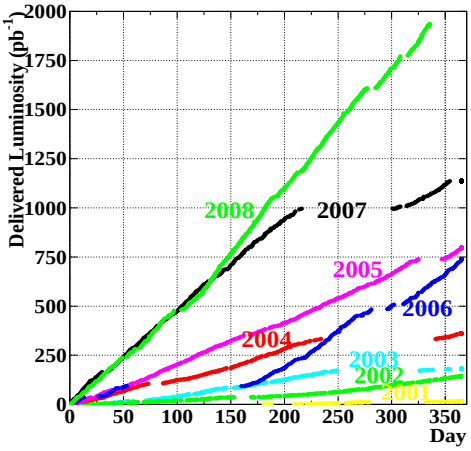

(b)

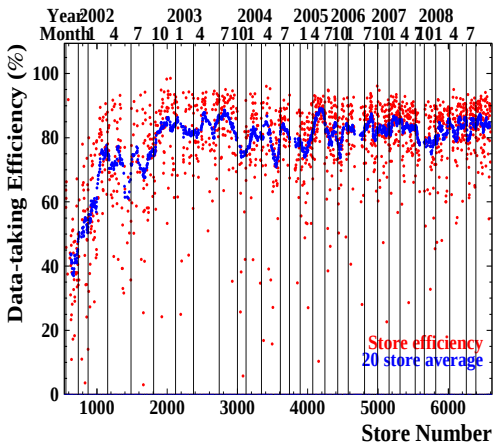

(c)

Figure 2.6: (a): Live integrated luminosity delivered (red) and written to tape (blue) since the start of Run II. The arrow indicates the used amount of data for this analysis. (b): Luminosity delivered by the Tevatron per year. (c): Data taking efficiency per store number.

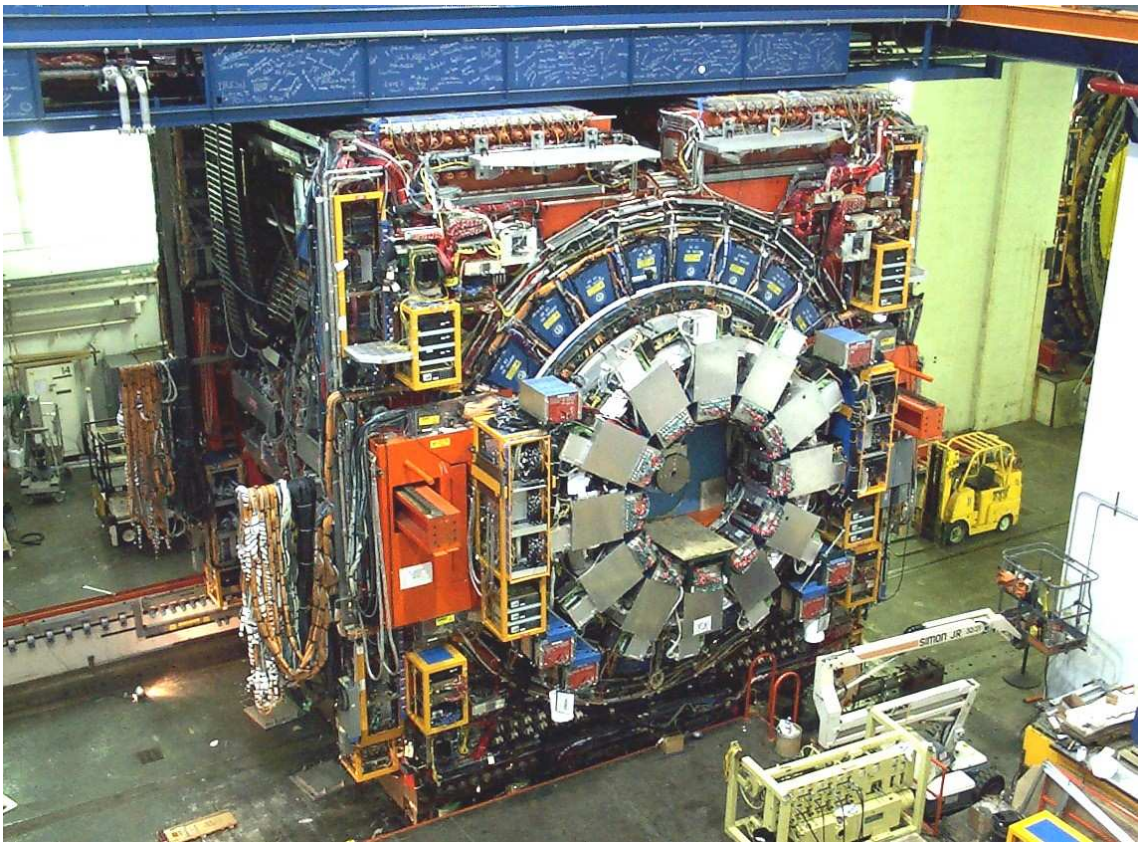

Figure 2.7: The CDF II detector (while rolling in for Run II).

direction, as shown in figure 2.8(c). Instead of θ, the pseudorapidity η is frequently used, which is given by $\eta = -\ln\left(\tan\frac{\theta}{2}\right)$. The transverse energy and momentum of a particle are defined as $E_{\mathrm{T}} = E \cdot \sin\theta$ and $p_{\mathrm{T}} = p \cdot \sin\theta$, respectively.

2.2.1 The Tracking System

The devices of the tracking system are closest to the beamline. This enables them to determine the primary vertex of the event and further reconstruct charged particles. The different parts of the system are imbedded in a 1.4 Tesla magnetic field which is parallel to the beam-axis and provided by a superconducting solenoid. The solenoid is 4.8 m long and its radius is 1.5 m. It is contained within a cryostat where it is cooled by liquid helium. The different parts of the tracking system are the silicon detectors, the Central Outer Tracker (COT) and the Time of Flight (TOF) detector and their location is shown in figures 2.8(b) and 2.9.

The innermost silicon detector is called Layer 00 (L00). L00 is used for improved precision of track measurements and b tagging efficiency. Layer 00 is placed directly outside the beampipe at a radius of approximately r = 1.6 cm and covers the region of $|\eta| \leq 4.0$. It was called 'Layer 00' in order to clarify that it is really the innermost

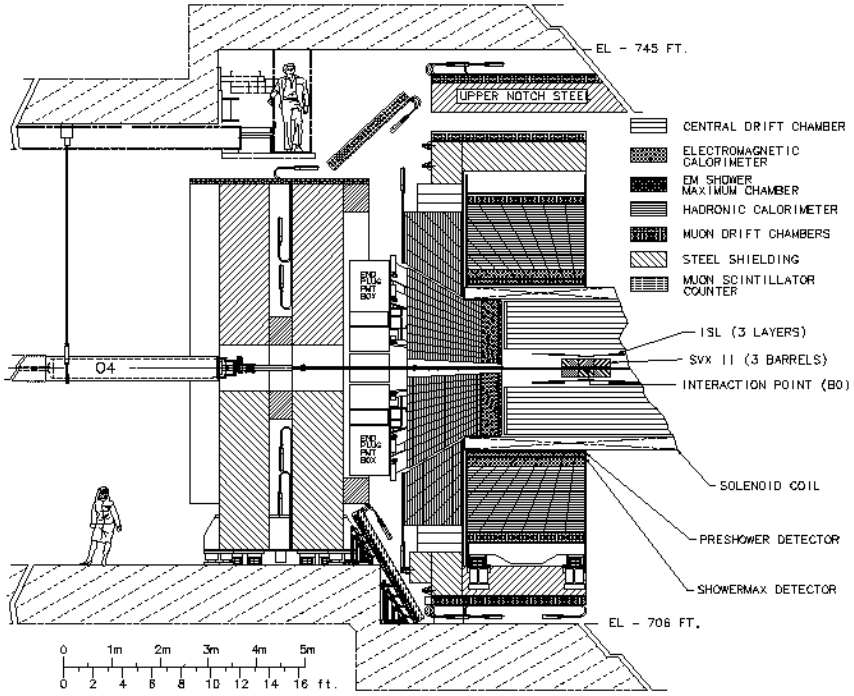

(a)

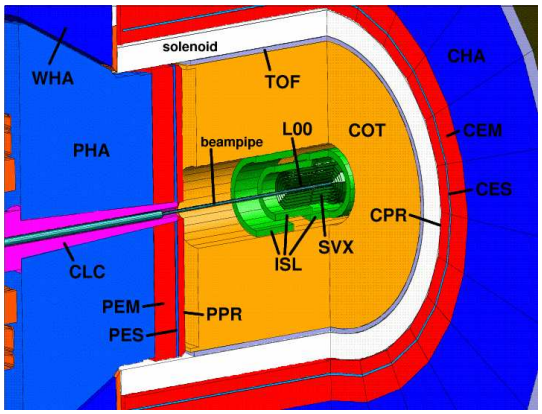

(b)

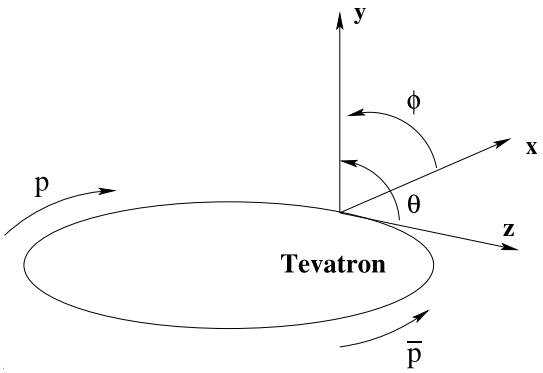

(c)

Figure 2.8: (a): Elevation view of one half of the CDF II detector. (b): Inner parts of the CDF II detector. Green and orange parts stand for the tracking system, while red and blue for the calorimeters. (c): The CDF II coordinate system.

layer and not confuse it with the innermost layer of SVX II (layer 0). L00 consists of 72 modules equipped with single-sided silicon microstrip detectors, with six modules in z and 12 staggered wedges in ϕ. Six wedges contain 'narrow' modules at a radius of r = 1.35 cm and 6 wedges use 'wide' modules at a radius of r = 1.62 cm. The narrow and wide modules overlap for full coverage. Similar to SVX ladders, each module consists of two silicon sensors bonded together end-to-end. The narrow modules are 256 strips wide and the wide modules are 512 strips wide. Only half of

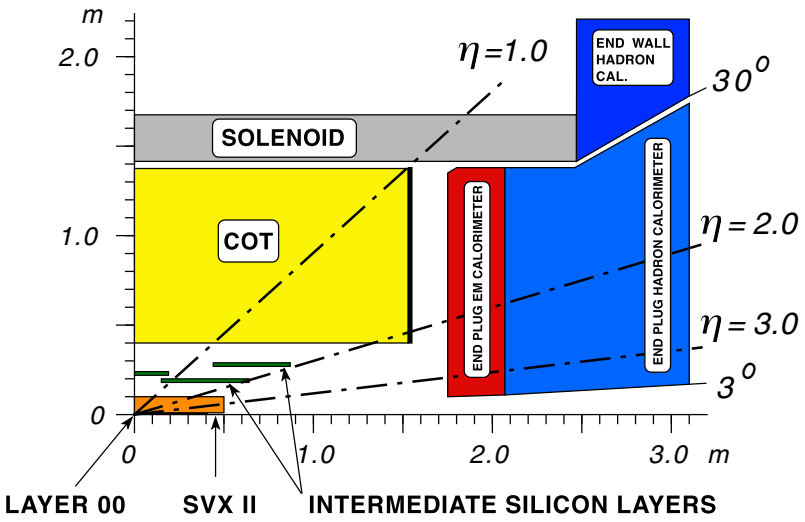

Figure 2.9: Longitudinal view of the CDF II tracking system.

these strips are read out (128 readout strips for narrow modules, 256 readout strips for wide modules). However, unlike in SVX, the readout hybrids are located outside of the tracking volume (one group on the west side to read out the west modules and one group on the east side to read out the east modules) and connected to the sensors by a fine-pitch cable. Figure 2.10(a) shows an end view of Layer 00.

The Silicon Vertex Detector (SVX) is often called SVX II to distinguish it from its Run I predecessors, SVX and SVX'. Its purpose is high-precision tracking and secondary vertex detection at inner radii. It extends from r = 2.1 cm to r = 17.3 cm and covers an area of $|\eta| \leq 2.0$. SVX consists of five layers of double-sided silicon microstrip detectors. Strips are aligned axially on one side, with 90-degree stereo on the other side for layers 0, 1 and 3 and small-angle stereo (1.2 degrees) on the other side for layers 2 and 4. SVX's layout consists of 360 half-ladders, organized into 6 bulkheads in z (three barrels each with a bulkhead on either side), 5 layers in r and 12 wedges in ϕ. Ladders in adjacent wedges overlap slightly, to provide full coverage. The individual ladders get wider in successive layers; layer 0 (the innermost layer) has 256 strips on the axial side of each ladder, while layer 4 (the outermost layer) has 896 strips on the axial side of each ladder. An end view of SVX is shown in Figure 2.10(b).

The purpose of the Intermediate Silicon Layer (ISL) is to provide enhanced linking of tracks between SVX II and COT in the central region. Moreover, in the plug region, where COT coverage is incomplete, it provides improved silicon-only tracking capabilities. ISL is located between SVX II and COT. It's central layer is at r = 22 cm and the forward/backward layers are at r = 20 cm and r = 28 cm. The central layer covers $|\eta| < 1.0$ and the forward/backward layers cover $1.0 < |\eta| < 2.0$. ISL is equipped with double-sided silicon microstrip detectors (axial on one side, small-angle stereo on the other side). The ISL consists of 296 total half-ladders. Each ladder has 1024 strips on the axial side and 768 strips on the stereo side. Only

half of these are actually read out (512 axial, 384 stereo). ISL ladders are very similar to SVX, except each half-ladder consists of three silicon sensors bonded end-to-end with a single double-sided hybrid which reads out both sides of the silicon. The hybrids do not lie on the top of the silicon as they do for SVX half-ladders, but are rather attached at the end. Figure 2.10(c) gives a schematic overview of ISL.

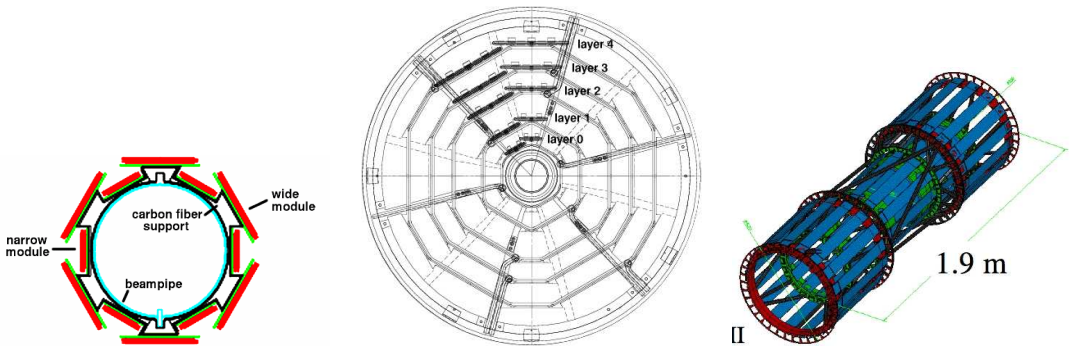

(a) (b) (c)

Figure 2.10: Schematic overview of the components of the silicon microstrip detector: (a) Layer 00, (b) SVX II, and (c) Intermediate Silicon Layers.

The Central Outer Tracker (COT) is used for general-purpose tracking in the central regions of the detector. It is placed outside of the silicon tracker, from r = 40 cm to r = 137 cm and covers $|\eta| \leq 1.0$. COT is an open-cell drift chamber with argon-ethane gas in a 50:50 mixture and provides in total 96 measurements. It replaces the Run I Central Tracking Chamber (CTC) and features a greater number of sense wires (about five times more), enhanced stereo coverage and faster drift times. It consists of 2520 cells which are divided into 8 superlayers. The number of cells in each superlayer ranges from 168 for SL1 to 480 for SL8. Superlayers 2, 4, 6 and 8 are axial (wires parallel to the beam), while superlayers 1, 3, 5 and 7 are at a small stereo angle (2 degrees). Each cell has a wire plane containing 12 sense wires and 13 potential wires, with two additional shaper wires at either end. Wire planes are separated by gold-on-Mylar field panels with stainless steel wires at either end. Cells are installed at a 35-degree Lorentz angle.

The Time-of-Flight Detector (TOF) is designed to collect time-of-flight information in order to enhance particle identification abilities in the central detector, especially for improving K-π discrimination. It is placed outside of COT, at an approximate radius of 140 cm. TOF is a scintillator read out by PMTs via lightguides and new for Run II. It consists of 216 bars of scintillator, each running the length of COT, arranged cylindrically with a PMT at each end of each bar. PMTs 0 to 215 are on the east side and 216 to 431 are on the west side. The bars have a trapezoidal cross section in order to minimize empty space between them.

2.2.2 The Calorimeter System

The calorimeter systems are located outside of the magnetic field of the solenoid. We distinguish between electromagnetic and hadronic calorimeter systems. The calorimeters are designed to fully absorb the kinetic energy of the particles except for the case that these particles are muons or neutrinos. They cover the range of $-3.6 < \eta < 3.6$ and $0 < \phi < 2\pi$. The whole system is built up in segments and consists of five different types of calorimeter:

The purpose of the Central Electromagnetic Calorimeter (CEM) is to measure the energy of electromagnetic showers in the central detector. It is placed outside of the solenoid in the central part of the detector and covers the region of $|\eta| < 1.1$. The CEM is a Pb/scintillator sampling calorimeter, 31 layers deep. It consists of 478 towers, which are organized into 24 wedges in ϕ and 10 tower groups in η on each side. Each tower is read out by two PMTs, one at the low-ϕ side of the tower and one at the high-ϕ side. These are typically called 'left' and 'right', respectively, with the directions defined as with the wedge upright, looking from z=0 towards the wedge. The cryogenic 'chimney', a space left for cables and cryogenic utilities for the solenoid, is located in wedge 5E. Towers 8 and 9 are removed for the chimney and tower 7 is slightly bigger to compensate.

The Central Hadronic Calorimeter (CHA) is used to measure the energy produced by hadronic showers in the central detector. It is located in the central detector outside of CEM and covers the area of $|\eta| < 0.9$. The CHA is a Fe/scintillator sampling calorimeter, 32 layers deep. It consists of 384 towers, organized into 24 wedges in ϕ and 8 tower groups in η on each side. Each tower is read out by 2 PMTs. The chimney also runs through wedge 5E of CHA. Towers 6 and 7 have a notch cut out and only one PMT.

The Endwall Hadronic Calorimeter (WHA) is used as an extension of hadronic calorimeter coverage to the endwall region. It is placed along the endwall outside of the plug and covers the region of $0.8 < |\eta| < 1.2$. The WHA is also a Fe/scintillator sampling calorimeter, but only 15 layers deep. It consists of 288 towers that are organized into 24 wedges in ϕ and 6 tower groups in η on each side. Each tower is read out by 2 PMTs.

The Plug Electromagnetic Calorimeter (PEM) measures the energy coming from the electromagnetic showers in the plug region of the detector. It is placed outside the barrel end of COT, one plug on each side, and covers the area of $1.1 < |\eta| < 3.6$. The PEM is a Pb/scintillator sampling calorimeter, 23 layers deep. It consists of 480 towers per plug, organized into 12 tower groups in η. The innermost 4 tower groups (largest η/smallest θ) each have 24 wedges in ϕ (each tower covers 15 degrees). The outermost 8 tower groups each have 48 wedges in ϕ (each covering 7.5 degrees).

The Plug Hadronic Calorimeter (PHA) is used to measure the hadronic showers in the plug region of the detector. It is placed beyond the PEM and covers $1.2 < |\eta| < 3.6$. The PHA is a Fe/scintillator sampling calorimeter, 23 layers deep and new for Run II. It consists of 432 towers per plug, organized into 11 tower groups in η. The

arrangement is the same as for PEM except the outermost tower group (smallest η/largest θ) does not exist (this area is already covered by WHA).

Tables 2.1 and 2.2 show an overview of the calorimeter properties.

Calorimeter	abbreviation	$\|\eta\|$ range	depth	Energy resolution
Central Electromagnetic	CEM	$\|\eta\| < 1.1$	18 X_0	$13.5\%/\sqrt{E}\oplus 1.5\%$
End-Plug Electromagnetic	PEM	$1.1 < \|\eta\| < 3.6$	23.2 X_0	$16\%/\sqrt{E}\oplus 1\%$
Central Hadron	CHA	$\|\eta\| < 0.9$	4.7 λ_I	$50\%/\sqrt{E}\oplus 3\%$
End Wall Hadron	WHA	$0.9 < \|\eta\| < 1.3$	4.7 λ_I	$75\%/\sqrt{E}\oplus 4\%$
End-Plug Hadron	PHA	$1.3 < \|\eta\| < 3.6$	6.8 λ_I	$80\%/\sqrt{E}\oplus 5\%$

Table 2.1: Overview of the calorimeter properties. The symbol $\oplus$ implies that the constant term is added in quadrature. The energy is given in GeV. The energy resolutions for the electromagnetic calorimeters are for incident electrons and photons and for the hadronic calorimeters for incident isolated pions. The depth is quoted in radiation lengths X_0 or hadronic interaction lengths λ_I, respectively. The depths and energy resolutions are taken from reference [52].

$\|\eta\|$ range	$\|\Delta\phi\|$	$\Delta\eta$	Calorimeter
$\|\eta\| < 1.3$	15°	~ 0.1	Central and End Wall
$1.1 < \|\eta\| < 1.2$	7.5°	~ 0.1	End-Plug Electromagnetic
$1.2 < \|\eta\| < 1.8$	7.5°	~ 0.1	End-Plug Electromagnetic & Hadron
$1.8 < \|\eta\| < 2.1$	7.5°	~ 0.1	
$1.8 < \|\eta\| < 2.1$	7.5°	~ 0.15	
$2.1 < \|\eta\| < 3.6$	15°	0.2-0.6	

Table 2.2: Segmentation and range of the different calorimeter systems.

2.2.3 The Muon System

In order to reconstruct the muons with sufficient p_T which may traverse the calorimeters, muon detectors are placed outside the hadronic calorimeter systems, see figure 2.11. The most important parts of the muon detection system are the muon chambers and the muon scintillators:

The Central Muon Chambers' system (CMU) is used to detect muons in the central detector region. It is located at the outside edge of CHA wedges and covers $|\eta| < 0.6$. The CMU is a wire chamber operated in proportional mode. It consists of 2304 cells, organized into 144 modules. There are 3 modules per CHA wedge per side. Each module is composed of 16 cells arranged in 4 radial layers of 4 cells each. Each cell contains one sense wire and runs the length of the wedge on one side.

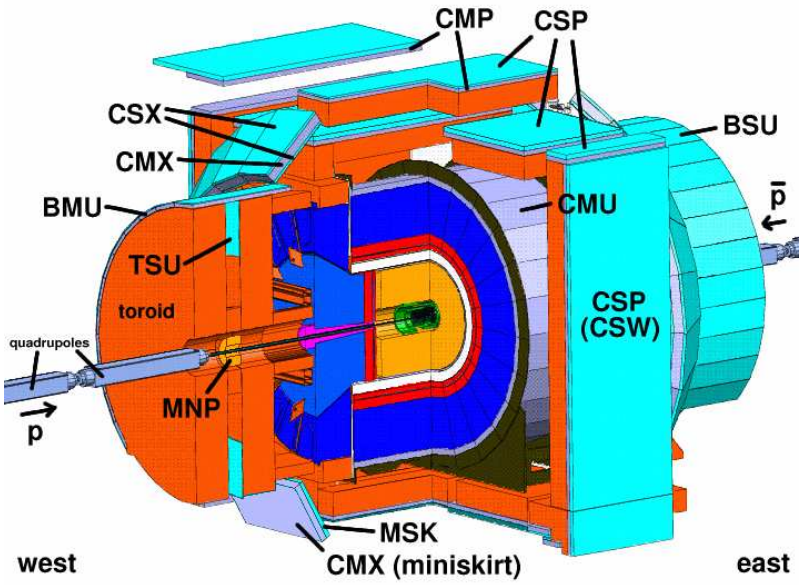

Figure 2.11: Cutaway view of the CDF II detector. Green and orange parts stand for the tracking system, while red and blue for the calorimeters.

The purpose of the Central Muon Upgrade (CMP) is to confirm the CMU tracks. Since the CMP is behind more material, CMP hits have a higher signal-to-background ratio and increase the trigger efficiency of the CMU/CMP combination. The CMP is placed along the walls, floor and top surface of CDF II. It also covers an area of $|\eta| < 0.6$. The central muon upgrade is a wire chamber operated in proportional mode. It consists of 1068 cells which are arranged in 4 layers. There are 77 stacks along the top, 65 along the bottom, 62 on the north wall and 63 on the south wall. Unlike the other detectors in CDF II, which are all (mostly) cylindrically symmetric around the beampipe, the CMP is roughly box-shaped. This is because the CMP uses the magnet return yoke steel as absorbing steel, along with some additional pieces of steel to fill gaps in the existing steel.

The Barrel Muon Chambers' system (BMU) is used to detect muons in the forward region. It is located on the outside of the toroids and covers the area of $1.0 < |\eta| < 1.5$. The BMU is a wire chamber operated in proportional mode and is new for Run II. It consists of 1728 chambers, 864 per toroid, arranged into 4 layers with 216 chambers per layer. Each chamber occupies 1.25 degrees of ϕ. The bottom 90 degrees of the barrel are not covered due to the support structures for the toroids (these are placed outside the plugs).

The Central Muon Extension (CMX) is used as an extension of the central muon coverage to $\eta = 1.0$. It is a truncated cone covering the area between the BMU and the CMP. The CMX is a wire chamber operated in proportional mode and covers $0.6 < |\eta| < 1.0$. The CMX is divided into two parts: the upper conical section, which covers the upper 270 degrees in ϕ, and the part of the lower 90 degrees in ϕ, which has a slightly different geometry due to the floor. The second part is called

the 'miniskirt'. The conical section contains 1632 cells, 864 on the west and 768 on the east side, divided into 18 wedges in ϕ (each covering 15 degrees). The miniskirt contains 576 cells, 288 per side.

	CMU	CMP	CMX	BMU
Pseudorapidity coverage	$\|\eta\| < 0.6$	$\|\eta\| < 0.6$	$0.6 < \|\eta\| < 1.0$	$1.0 < \|\eta\| < 1.5$
Min p_T of detectable μ	1.4 GeV/c	2.2 GeV/c	1.4 GeV/c	1.4-2.0 GeV/c

Table 2.3: η coverage and the minimal p_T for a muon to reach the detector for some parts of the muon system.

2.2.4 The Trigger System

Due to the bunch structure of the Tevatron beam, the bunch crossing rate is approximately 2.5 MHz (the original plan to upgrade the Tevatron to a crossing rate of 7.6 MHz was not realized because of beam stability issues). Taking into account the train structure, this is reduced to an effective crossing rate of 1.7 MHz. Since it is impossible to record each collision, it is necessary to draw decisions whether a specific event is worth to be recorded on an event-by-event basis. This is achieved by the CDF II three-level trigger system [53], illustrated in figure 2.12. The first two trigger levels are realized by special-purpose hardware, whereas the third one is implemented by software running on a Linux computer farm.

The first level (L1) finds physics objects based on a subset of the detector. Three parallel systems examine each event: calorimeter trigger boards find calorimeter-based objects, muon trigger cards identify muons and the eXtremely Fast Trigger (XFT) reconstructs tracks in the COT and matches those tracks to energy depositions in calorimeter towers or hits in the muon chambers. Information from all three systems is used independently to determine whether an event is passed to the second trigger level (L2). The typical L1 accept rate up to date is 25 kHz.

The L2 trigger performs minimal event reconstruction using custom-designed hardware consisting of several asynchronous subsystems. Besides calorimeter, track, and muon based streams, L2 incorporates information from the CEntral Shower maximum detector (CES) and SVX II. The CES, a strip chamber which is placed in the CEM at a depth corresponding to the average maximum of an electromagnetic shower, provides additional information about photons and electrons. The Silicon Vertex Trigger (SVT) [54] allows selection of tracks with a large impact parameter which is most important for B-Meson physics. L2 currently accepts about 600 events per second which are passed to the third trigger level (L3).

The L3 trigger [55] is a processor-based filtering mechanism which has access to the full event record, drawing its conclusions based on the event topology. Accepted

events are written to permanent storage media with approximately 100 Hz. To facilitate the handling of the huge collected data volumes, the events passing all three trigger levels are split into eight different data streams. The decision to which stream an event belongs depends on the triggers an event has passed; e.g. all events passing any of the high-p_{T} lepton triggers end up in "stream B".

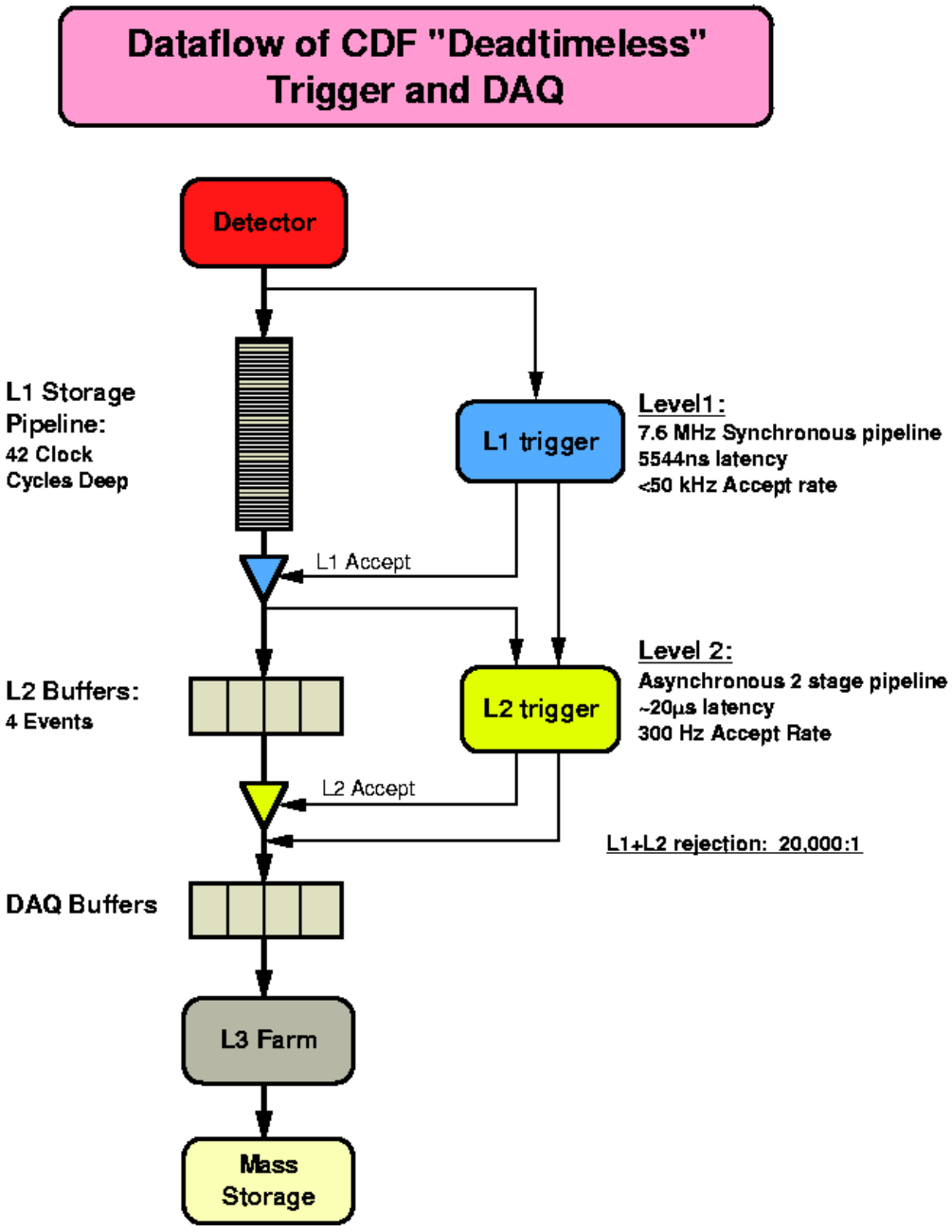

Figure 2.12: Run II readout functional block diagram.

Chapter 3

Experimental Methods

In this chapter, an overview is given concerning the experimental techniques used in this thesis. The basic methods for simulating and understanding the data taken by the CDF experiment are introduced in the following sections, starting with Monte Carlo (MC) methods and the detector simulation, the event reconstruction and finally the neural networks, which is the analysis method chosen for this thesis.

3.1 Monte Carlo Simulation

A good simulation is required when one deals with complicated analyses, such as those done at a particle detector. This requires the generation of MC events, randomly generated events that simulate different physics processes. The full generation of a MC event is done in different stages: the generation of the parton-level initial and final states, which corresponds to the generation of the matrix element (ME), the showering and the hadronization of the products. The generation of the ME can be separated from the showering and the hadronization and done by different programs. In the following subsections, the relevant MC generators to this analysis will be introduced, sorted according to their functionality.

3.1.1 Showering and Hadronization MC Generators

The process of the formation of hadrons out of quarks and gluons is called hadronization. This occurs after high-energy collisions in a particle collider, in which free quarks or gluons are created. Both cannot exist individually, due to color confinement, see section 1.1.1. There are different models used by various MC generators in order to simulate this process, some of them will be discussed in the subsections to come. Note that the cone of particles created by the hadronization of a single quark is called a jet. Jets are observed in particle detectors, rather than quarks, whose existence must be inferred.

Pythia

PYTHIA [56] is focussed on multi-particle production in hard interactions involving e^+, e^-, p, or $\bar{p}$. It uses theoretical models to describe hard and soft interactions, parton distributions, initial and final-state parton showers, multiple interactions, fragmentation and decay. In the case of the hadronization process, the Lund string model [57, 58] is chosen. The latter is a phenomenological model which treats all but the highest-energy gluons as field lines. These field lines are attracted to each other due to the gluon self-interaction and so form a narrow tube, also called string, of strong color field.

Herwig

HERWIG [59] is used for the simulation of lepton-lepton, lepton-hadron, and hadron-hadron collisions. A large range of hard scattering processes as well as initial and final state radiation are considered. The distinctive feature of HERWIG is its treatment of the subsequent decay of unstable resonances, including full spin correlations for most processes. Particular emphasis lies thereby on the detailed simulation of QCD parton showers. For the hadronization, HERWIG makes use of the preconfinement property of perturbative QCD [60] to form color-neutral clusters, which then subsequently decay into colorless hadrons.

3.1.2 Matrix Element MC Generators

The aim of tree-level matrix element generators, also called parton-level generators, is to compute the matrix element for a fixed number of partons in the final state. Given a process, they identify the relevant subprocesses and generate the corresponding amplitudes. The information about the contributing Feynman diagrams is then used to calculate cross sections and to obtain unweighted events at parton level.

These programs generally do not include any form of hadronization, thus the final states consist of bare quarks and gluons. It is necessary to interface these codes to showering and hadronization programs such as HERWIG or PYTHIA, in order to obtain a physically sensible description of the production process. This combination is essential for analyses based on multi-jet configurations where the standard showering codes are basically unable to describe the kinematics correctly.

TopReX

TopReX [61] provides the simulation of several important processes in pp and $p\bar{p}$ collisions, not implemented in PYTHIA. Some of these processes include top quarks whose spin polarizations are taken into account in the subsequent decay of the top quarks. Several non-SM top-quark decay channels are included, too. All

calculated subprocesses can be accessed from PYTHIA as external processes. In addition, TopReX can be used as stand-alone event generator, providing partonic final states before showering. The program flow chart of TopReX is shown in figure 3.1.
In this analysis, the output of TopReX was not directly passed to PYTHIA for the hadronization as shown in the figure. Instead, it was translated into "Les Houches" format, a format that can be interpreted by the so called `LesHouchesModule`. The "Les Houches" framework is useful for MC mass production, since, when making use of it, one does not have to include all ME-generators inside one package, which would lead to a huge size for the executable. Once the information is processed by the `LesHouchesModule`, it is given over to PYTHIA and subsequently to `CDFSim`, the simulation routine of the CDF framework.

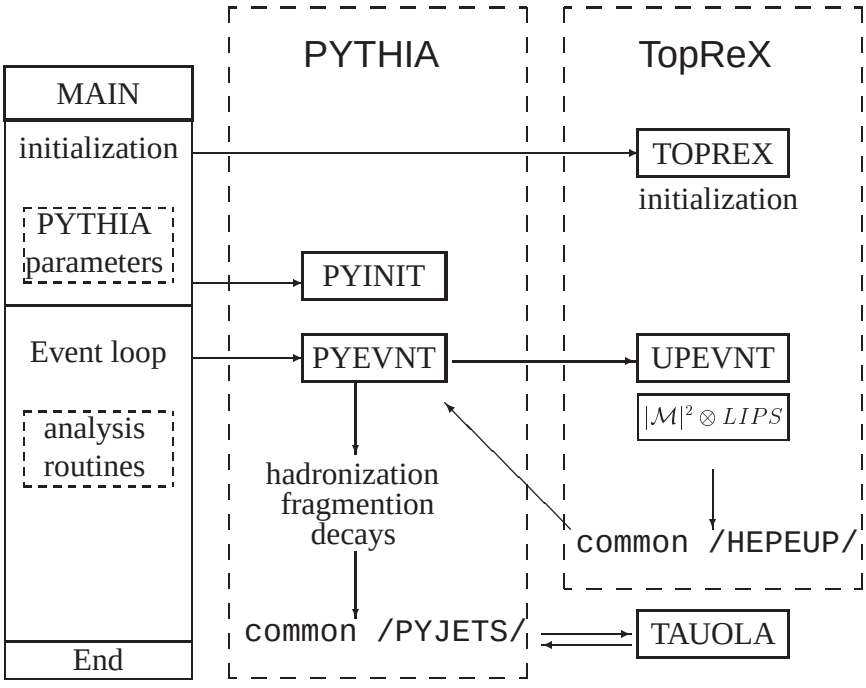

Figure 3.1: The program flow chart of TopReX MC generator. The main program initializes TopReX and PYTHIA. The initialization of TopReX consists predominantly of the passage of electroweak parameters from PYTHIA to TopReX, followed by the estimation of the minimal value of the differential cross section for the chosen hard scattering process. After the initialization, the generation of scattering events takes place in the event loop of the main program through a call to a subroutine, PYEVNT, in PYTHIA. Subsequently, a subroutine in TopReX, UPEVNT, is called.

MadEvent

MADEVENT [62] is a MC generator that can calculate arbitrary tree-level diagrams with full color and spin polarization information included. It is powered by the matrix-element generator MADGRAPH [63]. MADEVENT is used for diagrams in which the polarization of the top quark is an important part of the event kinematics. MADGRAPH generates automatically the amplitudes for all relevant subprocesses of a given a standard model process at any collider, e.g. e^+e^-, ep, pp, $p\bar{p}$. Moreover, it produces the mappings for the integration over the phase space. The process-dependent information is then passed to MADEVENT and a stand-alone code is produced that allows the user to calculate cross sections and to obtain unweighted events. The generated events are subsequently passed to a shower Monte Carlo program, where partons are perturbatively evolved through the emission of QCD radiation and eventually turned into physical states by hadronization. This MC generator was used to produce SM single top-quark events.

Alpgen

ALPGEN [64] is an event generator dedicated to the study of multi-parton hard processes in hadronic collisions. ALPGEN calculates the exact matrix elements for a large set of QCD and electroweak parton-level processes at leading order perturbation theory. Parton-level events are generated and full information on their color and flavor structure is provided, enabling the evolution of the partons into fully hadronized final states using HERWIG or PYTHIA. The large energies available at the Tevatron make final states with several hard and well separated jets a rather common phenomenon. These multi-jet final states can originate directly from hard QCD radiative processes or from the decay of massive particles, such as W or Z bosons. Among other final states, ALPGEN describes W-boson production in association with heavy-quark and light-quark production. This MC program was used for the generation of W+jets and Z+jets events. Thereby, it is important to take into account that the same n-jet configuration can be generated starting from different $(n-m)$-parton configurations, where the additional m partons are provided by the shower. Hence, to avoid double-counting of certain parts of the phase space, this necessitates a matching of the diverse parton configurations generated by the matrix element generator.

3.2 Detector Simulation

The next step, after making sure that the long-lived particles have been properly generated by the MC generators, is to specify the response of the detector to the formers. The response of all the different subcomponents of the detector, including resolution effects, inherent inefficiencies in the detector, and the reactions of the particles passing through passive material has to be taken into account in the simulation. Once this has been done, the MC events obtain a data structure similar to

the one gained from collision data. This allows reconstruction algorithms to work exactly the same way on measured and simulated events. At CDF, a program called GEANT [65] is used in order to model the tracking volume of the detector. By means of GEANT, one can simulate the passage of charged particles through the detector, including showering to secondary or tertiary particles. This simulation, in combination with the charge deposition models, allows the further simulation of the tracking detectors. However, by the time a charged particle reaches the calorimeter, it has showered into many secondary particles. Modelling all the interactions that take part in this process would require great computation capacity and power. In order to avoid this, CDF switches to a parameterized calorimeter response, tuned to test beam data, after the first inelastic collision occurs in the calorimeter. The program used for this purpose is called GFLASH [66]. This rapidly and accurately simulates the response of the calorimeter towers to the energy deposited by the incoming charged particles, completing the detector simulation. A detailed description of the CDF II detector simulation can be found in reference [67].

3.3 Event Reconstruction

In order to reconstruct physical processes, one has to convert the information collected by the detector, originating either from real collisions or from simulation, into physics quantities. The reconstruction process occurs in two basic steps. First, information from subdetectors is combined to form high-level detector objects. The latter consist of tracks in the tracking detectors and clusters in the calorimeters. Second, these objects are analyzed in order to get associated with physical objects like electrons, muons, jets, or neutrinos. After this final step, the information collected is ready to be used in a physics analysis.

3.3.1 Tracks

Tracking refers to the act of measuring the direction and magnitude of charged particles momenta. By combining all distinct point measurements, also called hits, that originate from a charged particle, CDF's tracking devices are able to reconstruct its trajectory. Because the tracking is made in a region where a magnetic field is present, it is possible to reconstruct part of the helix, which is called track, made by the particle inside the tracking device.

The curvature of the track depends on the momentum and charge of the particle, while the track direction points back to its origin.

Such tracks are described using five parameters, defined with respect to the point of minimum approach to the origin, the perigee, as illustrated in figure 3.2. The first parameter is the cotangent of the polar angle at the perigee $\cot\theta$, and is a measure of the helix pitch and the z component of the momentum. $\cot\theta$ corresponds to the pseudorapidity η. The second parameter is the half-curvature of the helix circle in

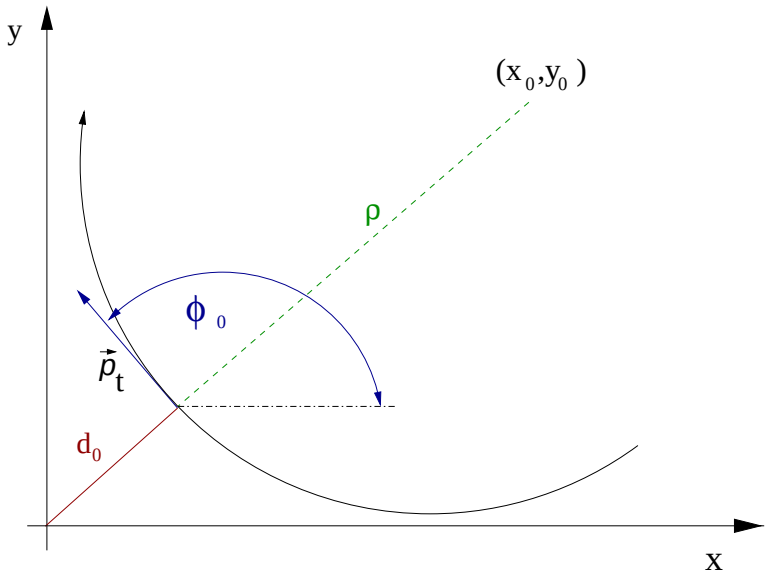

Figure 3.2: Parameterization of a charged particle track in the r–ϕ plane. The parameters are defined with respect to the perigee.

the r-ϕ plane, C, has the same sign as the charge Q of the particle and is given through $C = sign(Q)/2\rho$, where ρ is the radius of the circle centered at the perigee (x_0, y_0). C quantifies the momentum of the particle in the r-ϕ plane, the transverse momentum p_{T}. Moreover, z_0 is the z coordinate at the perigee. Furthermore, d_0, the signed impact parameter, is the distance between the helix and the origin at the perigee: $d_0 = sign(Q) \cdot \left(\sqrt{x_0^2 + y_0^2} - \rho\right)$. Finally, ϕ_0 is defined as the azimuthal direction of the helix at the perigee.

In the first stage of the tracking, tracks in the COT, see section 2.2.1 are reconstructed. This drift chamber is the tracking detector with the largest distance from the beam axis. Because its occupancy is lower and the tracks are more isolated, the reconstruction is easier for this detector compared to the one of the silicon detectors. There are two different algorithms in use to reconstruct tracks in the COT. The first algorithm is based on the code used in Run I to reconstruct tracks in the Central Tracking Chamber (CTC, now replaced by the COT) [68]. According to this approach, segments are reconstructed in the super-layers. Afterwards, these segments are linked together to reconstruct the trajectory. The second algorithm [69] uses one segment in the outer super-layers and the expected beamline to construct a reference track. The distances of the hits in the other super-layers from this reference are filled into a histogram, which is then used to determine the track parameters. This requires the tracks to be already beam-constrained, which improves the momentum resolution. However, when the reconstruction is done, the exact position of the beamline is not known. This has as a consequence that the tracks reconstructed by this algorithm have a bias towards the assumed beam position used in the construction of the reference tracks. More information about tracking in the COT can

be found in references [70, 71].
The reconstruction of the tracks in the silicon system occurs in three phases, the *outside-in* (OI), the *silicon stand-alone* (SISA), and the *inside-out* (IO) tracking. The OI-tracking algorithm propagates a track found in the COT into the silicon system and seeks to add hits to the track. Once a hit has been added, this additional information is used for the recalculation of the track parameters. Two implementations of this algorithm can be found in the CDF software. The first is based on the Run I code and uses a progressive fitter [72]. The second uses a Kalman fitter. The latter is the optimal fitter for this task, since it considers $\frac{dE}{dx}$ and multiple scattering effects. Nevertheless, since the COT does not cover the forward and backward regions $|\eta| > 1.1$, only the information of the silicon detectors can be used to find tracks up to $|\eta| < 2.0$. This is done with the SISA-tracking algorithm, which is also based on the Kalman fitter. This algorithm uses only hits not used by the two OI strategies in order to reduce combinatorics. The position of the beamline is needed for the construction of the track candidates, causing a small bias towards the assumed beam position. Furthermore, the IO tracking algorithm uses SISA tracks to define a search road for hits in the COT detector, which form a COT track. The latter is fitted using the silicon track information as constraints. Finally, using the new COT track as a seed, the silicon hits are refitted.
As far as the identification of electrons in the forward region is concerned, a special algorithm is used. This algorithm resembles the OI tracking strategy, only in this case, the primary vertex, see section 3.3.2, and an energy cluster in the PEM, instead of a COT track, are used to construct seed tracks. Two hypotheses about the charge of the particle are considered for each seed. This is done by computing the curvature for both an electron and a positron corresponding to the deposited energy.The extrapolation of those seed tracks into the silicon detector occurs analog to the propagation of the tracks within the OI tracking algorithm.

3.3.2 Primary Vertex

The primary vertex is defined as the point of the hard scattering interaction between the partons in a proton or antiproton. It is important to verify the location of the vertex in order to understand the kinematics of the particles that result from it. The knowledge of the position of a specific interaction affects the measured kinematic properties of the particles that result from a collision, because the interaction region of the particle beams has a substantial volume. The algorithm used in this case, collects a set of high-quality energetic tracks which have at least three silicon hits. Therefrom, it choses the thirty most energetic ones and performs a fit to a primary vertex. Moreover, it prunes the collection of tracks with a χ^2 cut and repeats the fit with the remaining tracks. This process is repeated until all tracks pass the cut. The result gives the final position of the primary vertex.

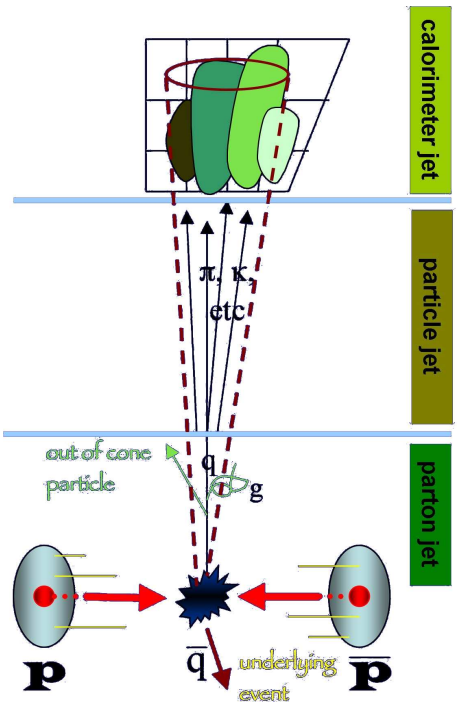

Figure 3.3: Schematic overview of jet reconstruction.

3.3.3 Jets

As already noted in section 3.1.1, one cannot detect free quarks in a particle detector. Instead, jets created by the hadronization of the quarks are measured. They appear as energy accumulation, shared among several detector calorimeter-towers. Figure 3.3 demonstrates the development from scattered partons to detector jets.

CDF experimenters use different types of jet-clustering algorithms to calculate the energy deposited in the calorimeter towers. Within the framework of this analysis, jets are clustered using a cone algorithm with a fixed cone size, in which the center of the jet is defined as $(\eta_{\text{jet}}, \phi_{\text{jet}})$ and the size of the cone as $R = \sqrt{(\eta_{\text{tower}} - \eta_{\text{jet}})^2 + (\phi_{\text{tower}} - \phi_{\text{jet}})^2} \leq 0.4$.

According to this algorithm, calorimeter towers with $E_{\text{T}i} > 1$ GeV are arranged into jets. $E_{\text{T}i} = E_i \cdot \sin\theta$ is defined as the transverse energy deposited in tower i with respect to the primary vertex z position. E_i is the sum of energies measured in the electromagnetic and hadronic compartments of that tower. First, a list of seed towers is created. It is sorted by decreasing $E_{\text{T}i}$. Within a radius of size R with respect to its position adjacent towers, for each seed tower, are used to build clusters. At the time a first list is completed, the calculation of the transverse energy and the position of the cluster starts. This is an iterative procedure: for every new center a new list of towers around it is produced. E_{T} and direction of the jet are recalculated until the geometrical center of the tower corresponds to the cluster centroid. If jets overlap more than 50%, they are merged. If that is not the case, each tower in

an overlap region is assigned to the nearest jet. In the end, the final jet energy is computed from the final list of towers N_{tow}:

$$E_{\text{jet}} = \sum_{i=0}^{N_{\text{tow}}} E_i \tag{3.1}$$

Jet-Energy Correction

The clustered energy of a detector jet has to be corrected in order to avoid distortion of the measurement due to several effects that may take place. Such phenomena are the response of the calorimeter to different particles, non-linear response of the calorimeter to the particle energies, uninstrumented regions of the detector, spectator interactions, and energy radiated outside the jet cone. The corrections are divided into discrete levels to accommodate different effects.

This allows the scaling of the measured energy of a jet back to the energy of the final-state particle-level jet. In addition, there are corrections to associate the measured jet energy to the parent parton energy. In that way, one is able to compare the measurement directly to the theory. Reference [52] provides detailed information about the jet-energy corrections.

η-dependent Corrections (Level 1) The response of the CDF calorimeter is not uniform in pseudorapidity as illustrated in figure 3.4(a). The dependencies on η arise from the separation of calorimeter components at $\eta = 0$ where the two halves of the central calorimeter join and at $\eta \approx 1.1$ where the plug and the central calorimeter adjoin. Another factor that plays a role is the different responses of the plug and the central calorimeter.

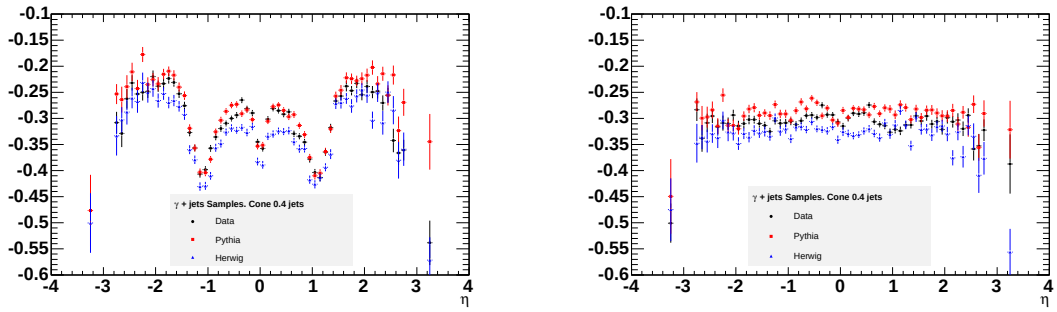

(a) (b)

Figure 3.4: Calorimeter response of photon-jet events from data and MC samples as a function of pseudorapidity (a) before and (b) after the correction of η-dependence.

The η-dependent corrections are determined based on the assumption that the two jets in dijet events should be balanced in p_{T} in absence of hard QCD radiation. The

response of the forward region of the calorimeter has to be scaled to the central region, because the latter is better understood. Moreover, one has to select a region far away from the cracks as reference. Therefore, a "trigger jet" with $0.2 < |\eta| < 0.6$ is chosen. The other jet is referred to as "probe jet". Hence, the η-dependent correction is defined as the scaling of the p_{T} of the probe jet to balance the trigger jet.

Photon-jet events are utilized in order to check the correction. This is so, because the photon should be balanced by a jet in these kind of events. Figure 3.4(b) shows the flattening of the calorimeter response as a function of η, having applied the Level 1 correction.

Multiple $p\bar{p}$ Interactions (Level 4) Because more than one $p\bar{p}$ interaction can occur in the same bunch crossing, the energy of the jets from the hard scatter is increased, in case the final-state hadrons, originating from these additional interactions, accidently overlap with the jets. The extra amount of energy has to be subtracted from the jet energy. The best approach, in order to estimate the number of interactions in a bunch crossing, would be to utilize the number of reconstructed vertices N_{vtx}. Using minimum-bias data triggered with hits in gaseous CLC in the very forward direction $3.7 < |\eta| < 4.7$, the transverse energy in a cone around a random seed tower in the central region $0.2 < |\eta| < 0.6$ is measured in dependence on N_{vtx}. The extra transverse energy per interaction as a function of N_{vtx} is given by the slope of the straight line fitted to this distribution. This is shown in figure 3.5.

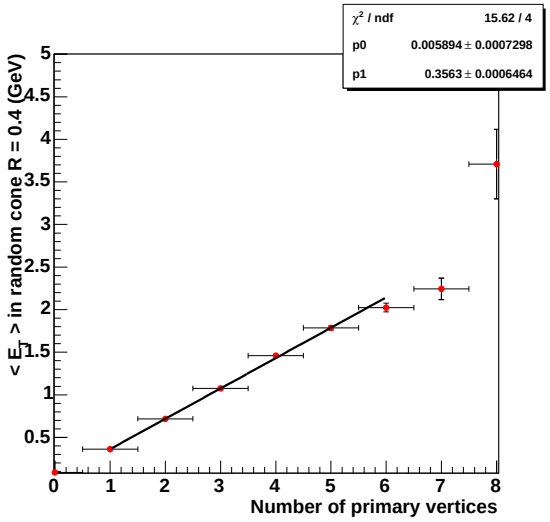

Figure 3.5: The dependence of the jet E_{T} on the number of $p\bar{p}$ interactions, i.e. the number of primary vertices N_{vtx}. The slope of the fitted straight line gives the extra transverse energy per interaction as a function of N_{vtx}.

Absolute Jet Energy Scale (Level 5) The jet energy measured in the calorimeter needs to be corrected for any nonlinearity and energy loss in the uninstrumented regions of each calorimeter. Since there are no high statistics calibration processes at high E_{T}, this correction is extracted from MC. The simulation of the calorimeter needs to accurately describe the response to single particles, such as pions, protons and neutrons. The fragmentation in MC events needs to describe the particle spectra and densities of the data for all jet E_{T}. The fragmentation and single particle response is measured in data and the MC simulation, which is tuned to describe it. The correction is obtained by mapping the total p_{T} of the hadron-level jet to the p_{T} of the calorimeter-level jet. The particle jet consists of particles within a cone of $R = 0.4$ and must be within $\Delta R < 0.1$ of the calorimeter jet. In figure 3.6, the correction of Level 5 is displayed.

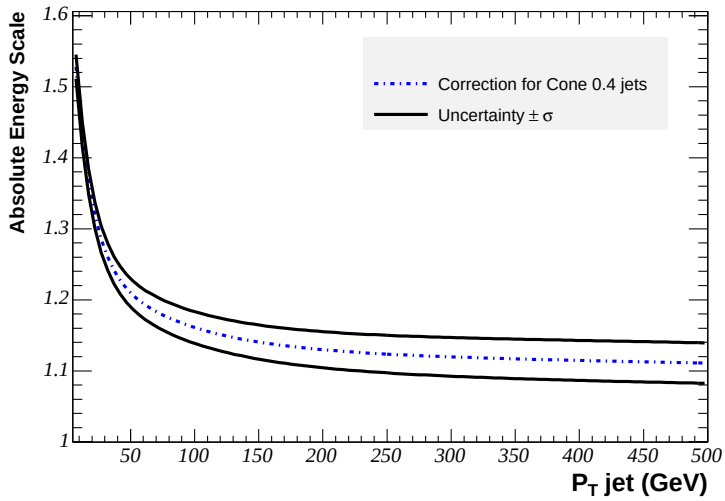

Figure 3.6: Absolute jet energy corrections as a function of jet p_{T}.

Underlying Event (Level 6) The underlying event is defined as the energy associated with the spectator partons in a hard collision event. Depending on the details of the particular analysis, this energy needs to be subtracted from the particle-level jet energy.

Out-of-Cone (Level 7) The out-of-cone correction corrects the particle-level energy for leakage of radiation outside the clustering cone used for jet definition, taking the jet energy back to parent-parton energy. The correction is derived from measurements of the energy flow between cones of size 0.4 and 1.3. The correction factor for the jets used in this analysis is shown in figure 3.7.

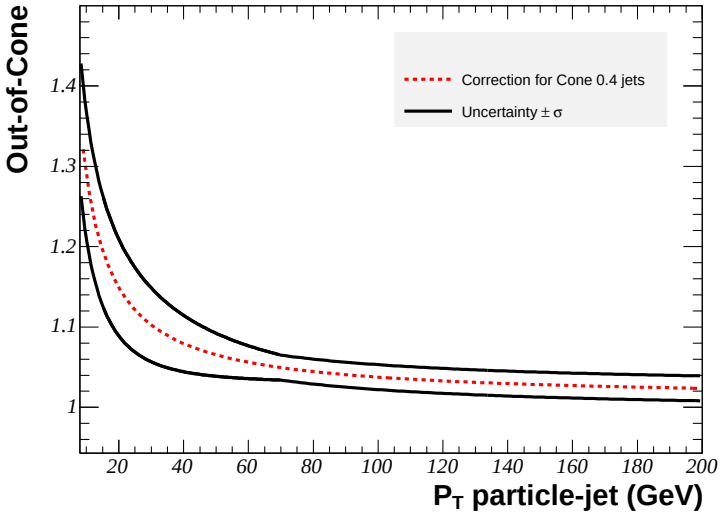

Figure 3.7: Out-of-cone jet energy corrections as function of the p_{T} of the particle jet.

3.3.4 Secondary Vertex

As already mentioned in section 1.1.2, the top quark decays to almost 100% into a W boson and a bottom quark. Therefore, it is crucial for an analysis in the top-quark sector to know the flavor of a quark producing a jet in order to be able to extract a signal. It is possible to discriminate jets originated by a bottom quark from jets originated by lighter quarks or gluons. A b quark originating from the top-quark decay is expected to hadronize almost immediately and form a jet of particles like mesons and baryons. Due to the relatively large mass of the bottom quark, the bottom hadron carries most of the momentum of the original quark. The hadron is boosted and, due to its relatively long lifetime of about 1.6 ps, it travels a sizable distance away from the primary interaction point in the laboratory rest frame before it decays. Through reconstruction of charged particle tracks, one is able to search for the trajectories of the decay products that have a large impact parameter and are therefore inconsistent with originating from the initial interaction point. The displaced tracks, that is tracks with large impact parameters, can then be tested to possess a common origin and may be used for the construction of a so called secondary vertex. This is demonstrated in figure 3.8.

The algorithm for the construction of a secondary vertex mostly in use at the CDF is called SecVtx [73]. This algorithm searches for a secondary vertex directly. SecVtx runs on an per-jet basis within each event and starts by considering silicon tracks within each jet. The tracks must be seeded (OI) or confirmed (IO) by a track in the COT. The tracks within the jet are demanded to have $p_{\mathrm{T}} > 0.5$ GeV/c, d_0 significance $S_{d_0} \equiv |d_0/\sigma_{d_0}| > 2.0$ with respect to the primary vertex. In addition, a minimum number of hits in the silicon detectors is required. These requirements

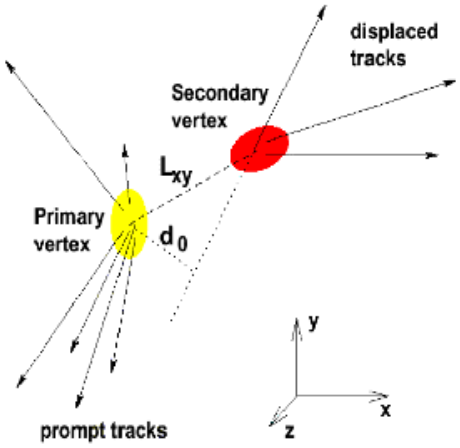

Figure 3.8: Schematic view of displaced tracks with impact parameter d_0 forming a secondary vertex. L_{xy} is defined as the projection of the two-dimensional decay length on the jet axis.

depend on the detector geometry and the quality of the reconstructed tracks. Moreover, tracks have to not exceed the maximum value for $d_0 = 0.15$ cm. This last selection criterion is chosen to prevent from reconstructing tracks of poor quality and those faked by long-lived light-flavor hadrons or nuclear interactions in the detector material. Afterwards, the selected tracks are ordered in p_{T}. In order to find a secondary vertex, the algorithm tries to construct a two-track seed vertex among the qualifying tracks. Provided that a seed vertex is found, the rest of the tracks are accounted for vertexing with the seed tracks. Once all qualifying tracks have been attached to the vertex, the vertex is refitted. In addition, tracks that contribute a $\chi^2 > 10$ to the this fit, are iteratively removed. In the case three or more tracks still belong to the vertex, the latter has to pass the following cuts. Influences originating from material and nuclear interactions that may fake a vertex can be taken care of, by constraining the absolute value of L_{xy}. L_{xy} is defined as the 2D decay length of the fitted vertex with respect to the primary vertex, projected on the jet axis. A veto on all vertices with a radius greater than 2.5 cm with respect to the center of the SVX II is applied. Furthermore, if the invariant mass of a vertex is consistent with the masses of K_S or Λ, two long-lived light-flavor hadrons, the former has to be rejected. Nevertheless, a vertex only survives the final cut if the significance of its L_{xy}, $S_{L_{xy}}$, satisfies the relation $S_{L_{xy}} > 7.5$. The latter is defined as $S_{L_{xy}} \equiv |L_{xy}/\sigma_{L_{xy}}|$. Supposing a vertex satisfies the criteria above, it is classified as a secondary vertex and the jet is said to be "b tagged". More details about the requirements can be found in reference [74].

3.3.5 Leptons

In this analysis and generally at CDF, an electron is identified as an isolated track matched to a calorimeter cluster. An isolated track matched to a stub in a muon detector is required to detect a muon. Muons leave only minimum ionizing energy in the calorimeter as they pass through it. This happens so, because bremsstrahlung of the muons is negligible and muons do not interact by the strong force. Therefore, a muon has to leave minimum ionizing energy in the calorimeter, as an additional requirement. As a result, fake muon signals, resulting from energetic particles that manage to pass through the calorimeter, are reduced. Further details about the lepton identification used in this analysis will be discussed in section 4.2.1.

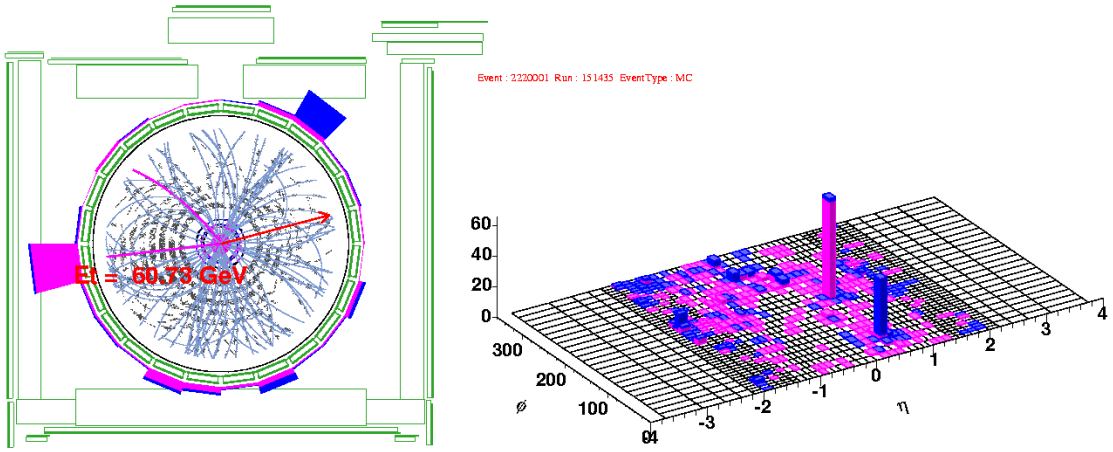

Figure 3.9: A simulated anomalous top event as it would be seen in the COT and the calorimeter (left). The color code is blue for the hadronic calorimeter and magenta for the electromagnetic calorimeter. The size of the colored clusters is proportional to the logarithm of the energy deposition. In this event, the highest cluster contains 60.73 GeV resulting mostly from electromagnetic energy. This is the tower in which the isolated electron, originating from the W decay, deposited its energy. The missing E_T vector, that points to the upper right side, represents the neutrino. On the right, the same event is demonstrated on the η-ϕ plane. The energy is given by the vertical-axis.

3.4 Neural Networks

In this analysis, the NeuroBayes® neural network package is used. It combines a three-layer feed-forward neural network with a complex robust preprocessing. This preprocessing is performed before the input variables are fed to the neural network. The neural network uses Bayesian regularization techniques for the training process. The network infrastructure consists of one input node for each input variable plus one bias node, an arbitrary number of hidden nodes, and one output node which gives a continuous output in the interval $[-1, 1]$.

The nodes of two consecutive layers are catenated with variable connections. For each node j, a biased weighted sum of the values of the previous layer x_i is calculated

$$a_j(\mathbf{x}) = \sum_i \omega_{ij} x_i + \mu_{0,j} \tag{3.2}$$

and passed to the transfer function which gives the output of the node. The bias $\mu_{0,j}$ implements the threshold of node j. The output of each node is determined by a transformed sigmoid function

$$S(\mathbf{x}) = \frac{2}{1 + e^{-a(\mathbf{x})}} - 1 \tag{3.3}$$

which gives an output of -1 for background and $+1$ for signal. As can be seen in figure 3.10, the sigmoid function is only sensitive to a relatively small range around zero. By this transformation, the interval $[-\infty, +\infty]$ is mapped to the interval $[-1, +1]$. For very large ($x \to \infty$) or very small ($x \to -\infty$) values, a saturation effect is reached. The bias mentioned above shifts the mean of the sum of the weighted input data distribution $\sum_i \omega_{ij} x_i$ to the linear part of the sigmoid function.

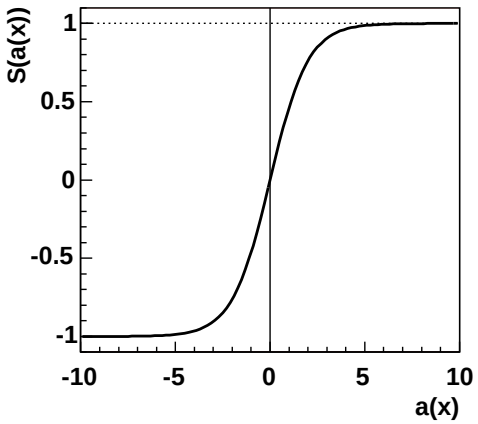

Figure 3.10: The transformed sigmoid activation function S(a(x)) as given by equation 3.3.

The output of the neural network for the output node is calculated by

$$o = S(\sum_{j=0}^{M} \omega_j \cdot S(\sum_{i=0}^{d} \omega_{ij} x_i + \mu_{0,j})) \tag{3.4}$$

where d is the number of input nodes and M the number of hidden nodes. ω_{ij} denotes the weights from the input to the hidden layer, ω_j the weights from the hidden layer to the output node. $\mu_{0,j}$ is the weight that connects the bias node with the hidden nodes.

3.4.1 The Training Process

The training of a neural network is done by minimizing the deviation between the true output and the one calculated by using the actual weights. The error function minimized in this neural network is the entropy error function

$$E_D = \sum_i \log(\frac{1}{2} \cdot (1 + T_i) \cdot o_i + \epsilon), \tag{3.5}$$

where the target value T_i is a binary number to classify event i as signal or background, o_i represents the output as given by equation (3.4). ϵ is a small regularization constant which is introduced in order to avoid numerical problems at the beginning of the training. This constant is reduced in each training iteration and is zero after just a few iterations.

The aim of the training of a neural network is to find the minimum in the multidimensional structure of the error function which may exhibit many peaks and valleys. As this task can be difficult to solve, the training process is done by the combined method of backpropagation and gradient descent, i.e. the change of each weight $\Delta\omega_{ij}$ is adjusted proportional to the current gradient of the error function $\Delta\omega_{ij} = -\eta\frac{\partial E_D}{\partial \omega_{ij}}$. The step width η is adapted individually for each weight during the training. Since the target value is not known for hidden nodes, the error induced by the current weights has to be propagated backwards from the output node by applying the chain rule for partial derivatives.

The neural network is trained with regularization techniques to improve generalization performance and to avoid overtraining. During the training process, the weights are systematically reduced in addition to the variation calculated by the gradient descent procedure. Thus, only recurring structures are intensified, while the influence of statistical fluctuations is reduced by so-called weight decay. Connections (and even nodes) that have become completely insignificant are pruned away. This reduces the number of free parameters and hence improves the signal-to-noise ratio by removing the cause of the noise, leading to an improved generalization ability. For details of the above mentioned features see references [75, 76].

3.4.2 Preprocessing of the Variables

To find the optimal starting point for minimizing the error function, the input variables are preprocessed. This preprocessing is done in a completely automatic way. Equalizing the input variables and scaling them to be distributed between -1

and 1 before passing the variables to the neural network reduces the influence of extreme outliers. Those flattened distributions are then converted into Gaussian distributions, centered at zero with standard deviation one. At the beginning of the training, this avoids saturation of the nodes due to the above mentioned shape of the activation function (see figure 3.10) and assures that also the inputs to the next layers are distributed with mean zero and width one. To decorrelate the preprocessed input variables, at first, their covariance matrix is calculated. Diagonalizing the covariance matrix using Jacobi rotations [77] and dividing the rotated input vectors by the square root of the corresponding eigenvalue transforms the covariance matrix into a unit matrix.

The above mentioned transformation to a Gaussian distribution may be altered by individual variable preprocessing like fitting a spline curve to the flattened distribution. In addition, discrete variables can be treated as members of classes. The preprocessing of those kinds of variables can also deal with a certain order of values, e.g. the number of tracks in a jet. The preprocessing is also able to deal with variables that are only given for a subset of events by assigning the missing values to a δ function.

3.4.3 Automatic Variable Selection

The significances of the training variables are determined automatically during the preprocessing in NeuroBayes®.

The correlation matrix of all preprocessed input variables is calculated including the correlation of all variables to the target. One variable after the other is omitted to determine the loss of total correlation to the target caused by its removal. The variable with the smallest loss of correlation is discarded leading to an $(n-1)$-dimensional correlation matrix. The same procedure is repeated with the reduced correlation matrix to find the least important of the $(n-1)$ remaining variables.

The significance of each variable is calculated by dividing the loss of correlation induced by its removal at the relevant point of the successive procedure by the square root of the sample size, i.e those significances are relative numbers in terms of the reduced correlation matrices.

After the preprocessing step, it is possible to cut on the significance of the variables to incorporate only those that include relevant information that is not already incorporated by other variables. The number of discarded variables is determined by scanning the sorted list, starting with the least relevant one, until the first quantity has a significance larger than the required minimum value.

3.4.4 Training Result

As already mentioned above, the network output of signal events piles up at $+1$, while background events accumulate at outputs around -1. This is illustrated in fig-

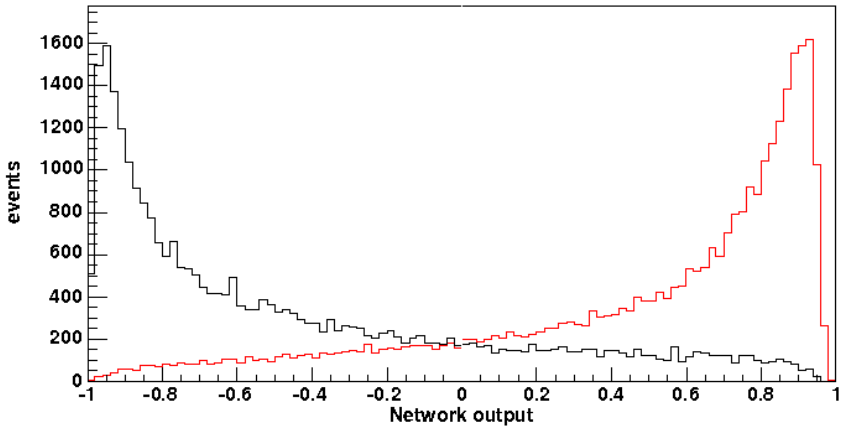

(a)

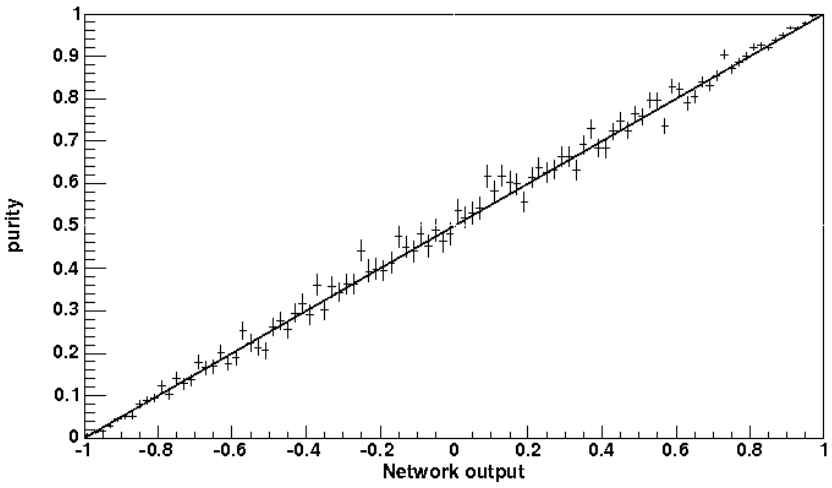

(b)

Figure 3.11: Illustration of the training result. Figure (a) shows the output distributions for signal (red line) and background (black line) events. Figure (b) shows the signal purity of each output bin and illustrates the expected linear dependence.

ure 3.11(a). After minimizing the entropy error function (3.5), the output, rescaled to the interval $[0, 1]$, can be interpreted as Bayesian *a posteriori* probability, if the *a priori* probability is correct, i.e. if a realistic mixture of signal and background has been chosen. Hence, the quality of the training can be checked by plotting the signal purity for each output bin, as illustrated in figure 3.11(b). If the network is well trained, all the points should lie on the diagonal.

For a detailed discussion of the output interpretation, see reference [75].

3.4.5 KIT Flavor Separator

The KIT flavor separator is an advanced jet flavor separating tool mainly developed to increase the sensitivity of the standard model single top-quark searches [78]. The flavor separator is also based on a NN which employs 31 input variables to discriminate b-quark jets on one hand from c-quark jets and light-quark jets on the other hand. The KIT flavor separator is also used as an input variable in the NN used for this search.

Chapter 4

Data Modeling and Event Yield

The application of multivariate analysis' methods requires a thorough understanding of both signal and background. In this chapter, all samples used for this analysis will be discussed, starting with the measured data samples, as well as the selection requirements for the candidate events. Moreover, signal and background simulation will be presented. As already mentioned in section 1.2.3, anomalous top-quark events feature a signature of a b-quark jet plus the decay products of a W boson. The latter is chosen to decay leptonically in this analysis. This serves the purpose of reducing the background originating from multijet production, initiated by the strong interaction.

4.1 Data Samples

The experimentally measured data, used for this analysis, were taken from March 2002 until August 2007 and correspond to an integrated luminosity of 2.2 fb^{-1}. High-p_{T} lepton triggers are used for the data selection, because of the fact that only the leptonic decay of the W boson is considered. A COT track with $p_{\mathrm{T}} > 9$ GeV/c matched to an energy cluster in the CEM with $E_{\mathrm{T}} > 18$ GeV is required. Constistency between the shower profile of this cluster and the expectation obtained by measurements, done with test-beam electrons, is demanded. Moreover, forward electron candidates should be energetic enough in order to deposit at least 20 GeV of their energy in the PEM. Furthermore, the ratio of hadronic-to-electromagnetic energy is necessary to fulfill $\frac{E_{\mathrm{HAD}}}{E_{\mathrm{EM}}} < 0.075$. As far as muons are concerned, a COT track with $p_{\mathrm{T}} > 18$ GeV/c is required. This has to be matched to a track segment in the muon chambers. The data are arranged into three basic categories, depending on which trigger they activated. The datasets of the first category, `bhel`, incorporate central electrons, while those of the second class, `bhmu`, contain muons. Finally, the datasets of the third class, `bpel`, comprise forward electrons. In order to verify and increase their quality, all data sets are being reprocessed offline, before the analysis starts. Calibrations, alignment, cluster energies are checked and corrected, leptons are being identified, while the jet clusters and the secondary vertices are fitted.

Table 4.1 shows some details of the data samples which were used for this analysis. The data were reprocessed with CDFSOFT2 [79] versions 5.3.1 and 6.1.1 in the first stage and afterwards reprocessed with version 6.1.4mc by the Top-Quark Analysis-Group. Moreover, they were stripped into `0d`,`0h`,`0i` and `0j` datasets. The period of data taking and the run range correspond to the plots shown in section 2.1.2.

period	run range	dataset	events [10^6]	$\mathcal{L}$ [pb^{-1}]		CDFSOFT2
				sub i	CMX	
0	138425 - 186598	`0d`	1016	331.47	318.11	5.3.1
1 - 4	190697 - 203799	`0h`	754	362.94	359.50	6.1.1
5 - 7	203819 - 212133	`0i`	573	258.37	258.37	6.1.1
8	217990 - 222426	`0i`	335	166.29	166.29	6.1.1
9	222529 - 228596	`0i`	250	156.76	152.78	6.1.1
10	228644 - 233111	`0i`	390	243.19	243.49	6.1.1
11	233133 - 23779	`0j`	369	234.99	229.98	6.1.1
12	237845 - 24166	`0j`	256	162.01	155.25	6.1.1
13	241665 - 24623	`0j`	545	280.86	268.35	6.1.1

Table 4.1: Information about the data samples used in this analysis: period of data taking, run range, type of stripping, integrated luminosity, number of events included in the set, CDFSOFT2 version used for reprocessing the data. sub i stands for the subdetectors CEM, CMUP and PHX, while the second column of the integrated luminosity refers to the CMX subdetector.

The data acquisition is not a continuous procedure as one may have already noticed in the presented tables and plots. This happens because the data taking is interrupted when hardware or software errors occur. However, each store consists of cycles, the so called runs, during which the data is collected non-stop. Only those runs can be used for analysis in which all detector components worked according to specifications. Runs in which certain components failed have to be excluded. After each run is validated, the suitable ones are organised in a list, which is called "goodrun" list [80]. This analysis uses the "goodrun" list version 19 [81], which can be found in the Appendix A. Table 4.2 shows the integrated luminosity in the various detector parts, which were used in this analysis.

Sub-detector	$\mathcal{L}$ [pb^{-1}]
CEM	2196.88
CMUP	2196.88
CMX	2152.12
PHX	2196.88

Table 4.2: Integrated luminosity in the detector components used for this analysis.

4.2 Requirements for Candidate Events

As already stated in section 1.2.3, the anomalous top-quark production is studied based on the SM decay signature of the top quark. The latter decays to almost 100% into a b-quark jet and a W boson, which then decays leptonically. Therefore, the experimental signature for the signal is $t \to bW \to b\ell\nu_\ell$. In this section, the requirements for the candidate events are discussed in detail.

4.2.1 Lepton Identification

After offline reconstruction, the lepton candidates have to pass further cuts in order to improve the purity. For central electrons, a reconstructed track with $p_{\mathrm{T}} > 10$ GeV/c has to match a cluster in the CEM with $E_{\mathrm{T}} > 20$ GeV. Furthermore, $E_{\mathrm{HAD}}/E_{\mathrm{EM}} < 0.055 + 0.00045 \cdot E$ is required; the ratio of cluster energy to track momentum E/p has to be smaller than 2.0 for track momenta ≤ 50 GeV/c. Electron candidates in forward direction are defined by a cluster in the PEM with $E_{\mathrm{T}} > 20$ GeV and $E_{\mathrm{HAD}}/E_{\mathrm{EM}} < 0.05$. The cluster position and the primary vertex are combined to form a search trajectory in the silicon tracker and seed the pattern recognition of the tracking algorithm. For the electron candidate to pass the selection, the found track has to fulfill certain quality criteria. Electron events are rejected, if an additional high-p_{T} track is found that forms a common vertex with the track of the electron candidate and has a curvature of opposite sign. These events are likely to stem from the conversion of a photon.

Muons are identified by requiring a COT track with $p_{\mathrm{T}} > 20$ GeV/c that extrapolates to a track segment in a muon chamber. Signal muons have to be detected in the CMU and CMP simultaneously or in the CMX. In order to minimize background contaminations further requirements are imposed. The energy depositions in the electromagnetic and hadronic calorimeters have to correspond to the expectation regarding minimum ionizing particles. To reject cosmic muons or muons from in-flight decays of long-lived particles (such as K_S, K_L, or Λ), the impact parameter d_0 of the track must be small. Cosmic muons are further rejected through their characteristic track timing and topology.

Furthermore, exactly one isolated lepton candidate is required, whereby a candidate is considered isolated if the E_{T} not assigned to the lepton in a cone of $R = 0.4$ centered around the lepton is less than 10% of the lepton E_{T} or p_{T}, respectively. This lepton is called tight lepton. A detailed description of all lepton requirements can be found in references [82, 83, 84].

4.2.2 Jet Reconstruction and Selection

In this analysis, jets are reconstructed with a cone of $R = 0.4$ without taking into account calorimeter towers which are associated to any tight isolated electron. The jet energy is corrected up to level 5, i.e for the η-dependence of the calorimeter

response, for multiple $p\bar{p}$ interactions, and absolute energy scale (i.e. up to the underlying particle jet). Candidate jets, required to have detector $|\eta| < 2.8$, must have corrected $E_{\mathrm{T}} > 20$ GeV to be called tight jets. Detector η is defined as the pseudorapidity of the jet calculated with respect to the origin of the coordinate system, which is located in the center of the detector. Only events with exactly one tight jet are accepted, whereby the jet must be tagged as a b-quark jet by requiring a displaced secondary vertex within the jet.

4.2.3 Missing Transverse Energy

The missing E_{T} ($\vec{\not\!\!E}_{\mathrm{T}}$) is defined by

$$\vec{\not\!\!E}_{\mathrm{T}} = -\sum_i E_{\mathrm{T}}^i \hat{n}_i, \tag{4.1}$$

where i denotes the calorimeter tower number with $|\eta| < 3.6$, $\hat{n}_i$ is a unit vector perpendicular to the beam axis which points at the i^{th} calorimeter tower. Additionally, $\not\!\!E_{\mathrm{T}} = |\vec{\not\!\!E}_{\mathrm{T}}|$ is defined. Because this calculation is based on calorimeter towers, $\vec{\not\!\!E}_{\mathrm{T}}$ has to be adjusted for the effect of the jet corrections for the tight and the loose jets.

Since muons pass the calorimeters without showering, i.e. as minimum ionizing particle, a correction is applied by adding all transverse momenta of the traversing muons to the sum and by removing the average ionization energy. The corrected $\not\!\!E_{\mathrm{T}}$ is required to be greater than 25 GeV.

4.2.4 Vetoes

Dilepton Veto To ensure that there is exactly one tight lepton, events are rejected, which have either an additional tight lepton or a loose lepton. Loose leptons are leptons which pass all cuts except the isolation cut, or are identified in the CMP, CMU or BMU solely.

QCD veto To further suppress events in which no real W boson is produced, additional cuts are applied. The cuts are based on the assumption that these events do not produce $\not\!\!E_{\mathrm{T}}$ by nature but due to lost or mismeasured jets. Therefore, one would expect small $\not\!\!E_{\mathrm{T}}$, small $\not\!\!E_{\mathrm{T}}$ significance $\not\!\!E_{\mathrm{Tsig}}$, a small transverse W-boson mass $M_{\mathrm{T},W}$, and small values of the angle $\Delta\phi_{\vec{\not\!\!E}_{\mathrm{T}},\mathrm{jet}}$ between $\vec{\not\!\!E}_{\mathrm{T}}$ and a jet. The $\not\!\!E_{\mathrm{T}}$ significance is defined as

$$\not\!\!E_{\mathrm{Tsig}} = \frac{\not\!\!E_{\mathrm{T}}}{\sqrt{\sum_{\mathrm{jets}} C_{\mathrm{JES}}^2 \cos^2(\Delta\phi_{\vec{\not\!\!E}_{\mathrm{T}},\mathrm{jet}}) + \cos^2(\Delta\phi_{\vec{\not\!\!E}_{\mathrm{T}}^{\mathrm{uncorr}},\vec{\not\!\!E}_{\mathrm{T}}^{\mathrm{corr}}})}} \tag{4.2}$$

with the level 5 jet-correction factor C_{JES} and the azimuthal angle $\Delta\phi_{\vec{\not\!\!E}_{\mathrm{T}}^{\mathrm{uncorr}},\vec{\not\!\!E}_{\mathrm{T}}^{\mathrm{corr}}}$ between uncorrected and corrected $\vec{\not\!\!E}_{\mathrm{T}}$. The transverse W-boson mass is given by

$$M_{\mathrm{T},W} = \sqrt{2{p_{\mathrm{T}}}^{\ell}\not\!\!E_{\mathrm{T}} - \vec{{p_{\mathrm{T}}}}^{\ell} \cdot \vec{\not\!\!E}_{\mathrm{T}}} \tag{4.3}$$

with ${p_{\mathrm{T}}}^{\ell}$ being the transverse momentum of the charged lepton.

Events passing the electron trigger must have $M_{\mathrm{T},W} > 20$ GeV. For central electrons, it is additionally required that $\not\!\!E_{\mathrm{Tsig}} > -0.05 M_{\mathrm{T},W} + 3.5$. Furthermore, the relation $\not\!\!E_{\mathrm{Tsig}} > -7.6 + 3.2|\Delta\phi_{\ell,\mathrm{jet}}|/0.8$ must be satisfied, with $\Delta\phi_{\ell,\mathrm{jet}}$ being the azimuthal angle between the charged lepton and the jet.

Forward electrons must have $\not\!\!E_{\mathrm{Tsig}} > 2.0$.

In muon events, the transverse W-boson mass must fulfill $M_{\mathrm{T},W} > 10$ GeV. Events containing CMUP muons are additionally required to have $\not\!\!E_{\mathrm{T}} > 60|\Delta\phi_{\ell,\mathrm{jet}}| - 145$.

Z-Boson Veto To remove Z-boson events, events are rejected in which the charged lepton can be paired with any more loosely defined jet or lepton to form an invariant mass consistent with the Z peak, defined as the range from 76 GeV/c^2 to 106 GeV/c^2.

Cosmic Veto Cosmic rays are identified using timing and track displacement information and are removed in this analysis, as are photon conversion candidates.

4.3 Signal MC

In order to calculate the leading order (LO) matrix element of the signal process, the TopReX Monte Carlo (MC) generator (version 4.23 [61]) was used. The parton showering and the hadronization of this output was done with PYTHIA (version 6.409 [56]). Furthermore, the PDF set CTEQ5L1 was used for the calculation. In TopReX, the process $u(c) + g \to t$, a $2 \to 1$ anomalous FCNC process, was chosen for the simulation on partonic level, which is described by the theory in section 1.2.3. The subsequent decay of the top-quark was forced to be SM like, whereas the resulting W-boson was allowed to decay only leptonically. For the MC production, we chose $\kappa/\Lambda = 0.023$ TeV^{-1}, which translates into a production cross section of $\sigma_{ano} = 1$ pb for the anomalous top-quark. This decision resulted from mainly three reasons: first, the coupling constant should be chosen in a sensible and sensitive parameter space, as argued in section 1.2.3. In addition, much higher values for the cross section (e.g. 10 pb, 100 pb) were already excluded, whereas our analysis would not be sensitive at that level for much smaller values (eg. 0.1 pb). Nevertheless, the chosen value for σ_{ano} would be in that way easy to rescale.
We also checked at parton level whether the kinematics are somehow influenced by the choice of the coupling constant. The check was done by comparing three samples

with different values for the anomalous coupling constant, each consisting of 100,000 events, to a sample with the same cross section as the one used for the analysis. The only parameter variating in the generation of these three control samples was the anomalous coupling constant: the first sample was generated for $\kappa/\Lambda = 0.05$ TeV^{-1} and has a cross section of 4.6 pb, the second sample for $\kappa/\Lambda = 0.1$ TeV^{-1} and $\sigma_{ano} = 18.3$ pb and finally, the third sample was generated for $\kappa/\Lambda = 0.01$ TeV^{-1} and $\sigma_{ano} = 0.18$ pb. We found that there is no difference worth paying attention to in the part of the spectrum of κ/Λ that is of interest for us. This is shown in figures 4.1-4.5.

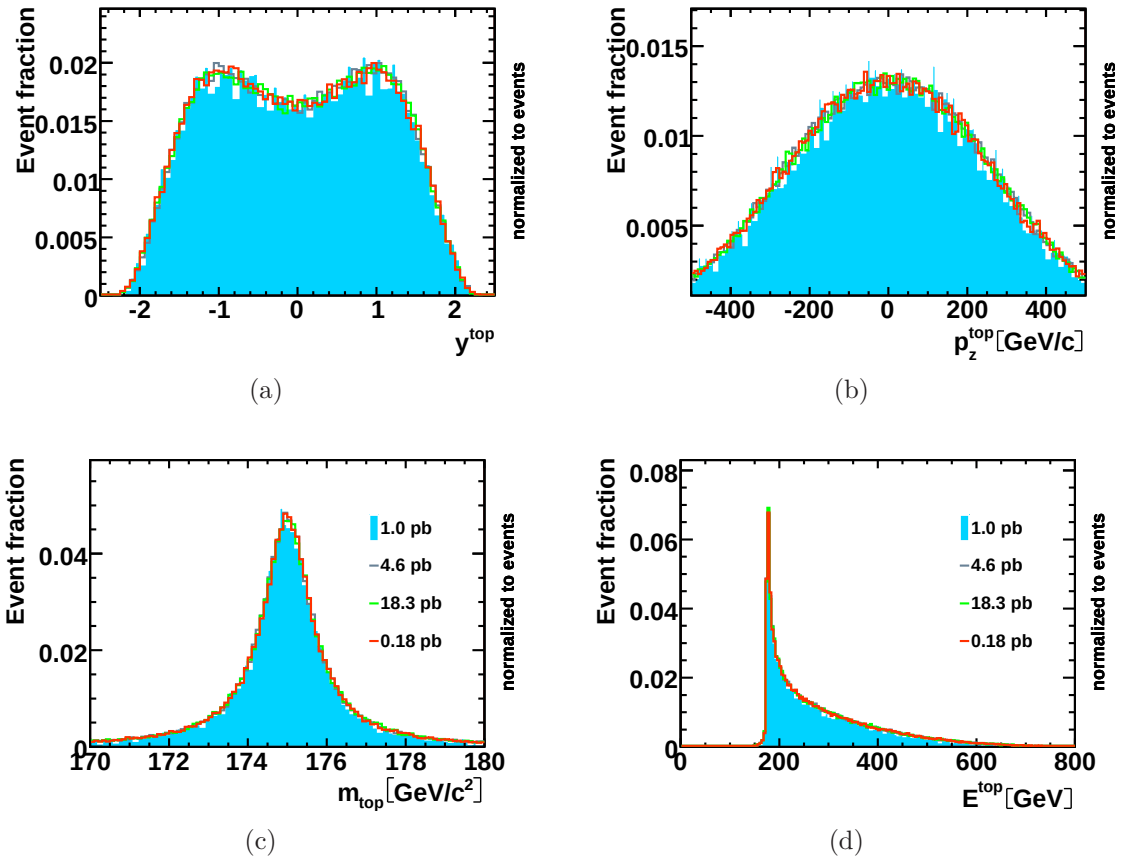

(a) (b)

(c) (d)

Figure 4.1: (a), (b), (c) and (d) are control plots for checking the kinematics for different values of the coupling constants at parton level. The region filled with blue color belongs to a sample with a cross section of 1 pb, as the one used for this analysis. The former is compared to anomalous top-quark samples with higher or lower cross sections, which corresponds to higher or lower values for the coupling constants. No significant difference can be seen.

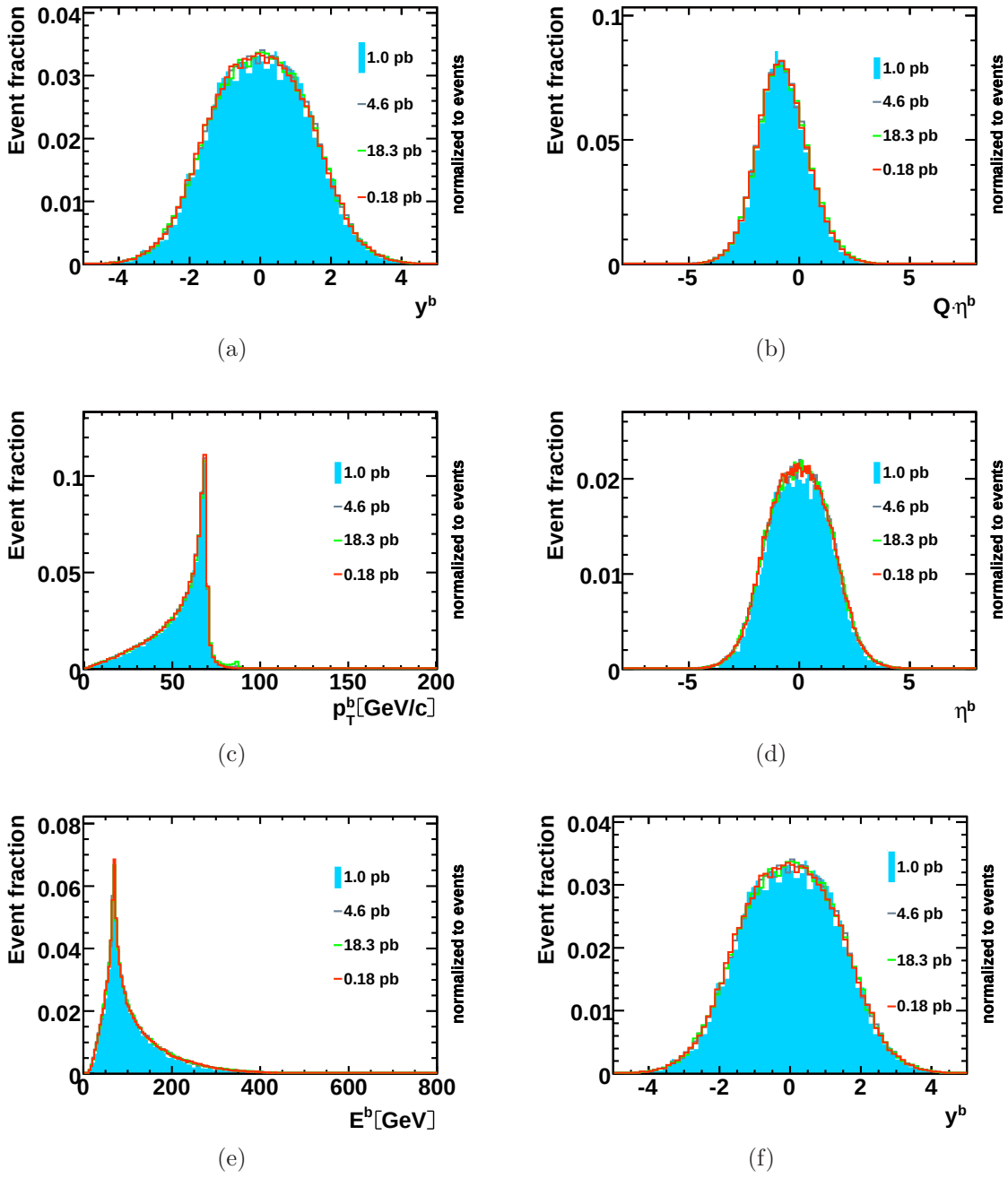

Figure 4.2: (a), (b), (c), (d), (e) and (f) are control plots for checking the kinematics for different values of the coupling constants at parton level. The region filled with blue color belongs to a sample with a cross section of 1 pb, as the one used for this analysis. The former is compared to anomalous top-quark samples with higher or lower cross sections, which corresponds to higher or lower values for the coupling constants. No significant difference can be seen.

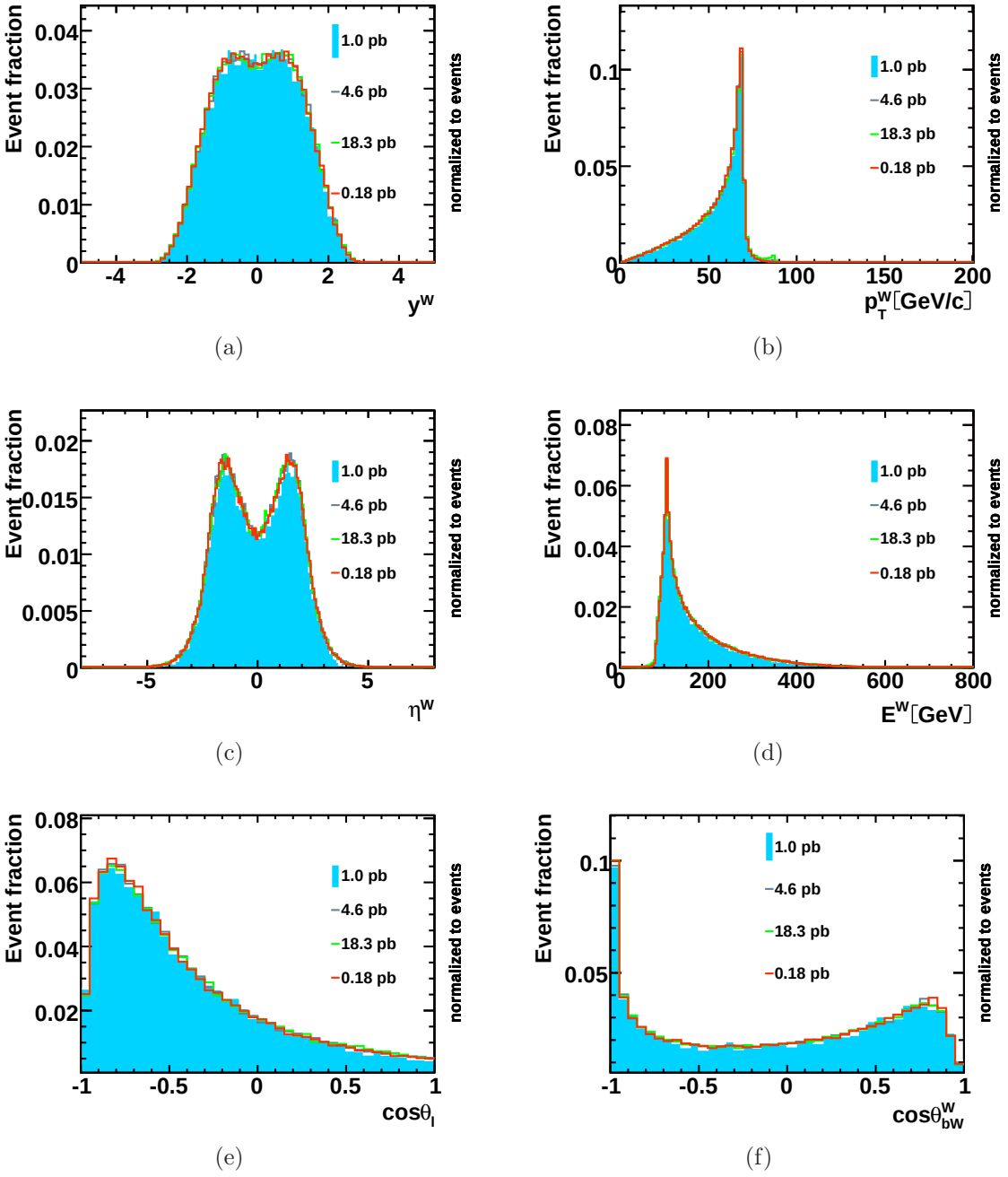

(a) (b) (c) (d) (e) (f)

Figure 4.3: (a), (b), (c), (d), (e) and (f) are control plots for checking the kinematics for different values of the coupling constants at parton level. The region filled with blue color belongs to a sample with a cross section of 1 pb, as the one used for this analysis. The former is compared to anomalous top-quark samples with higher or lower cross sections, which corresponds to higher or lower values for the coupling constants. No significant difference can be seen.

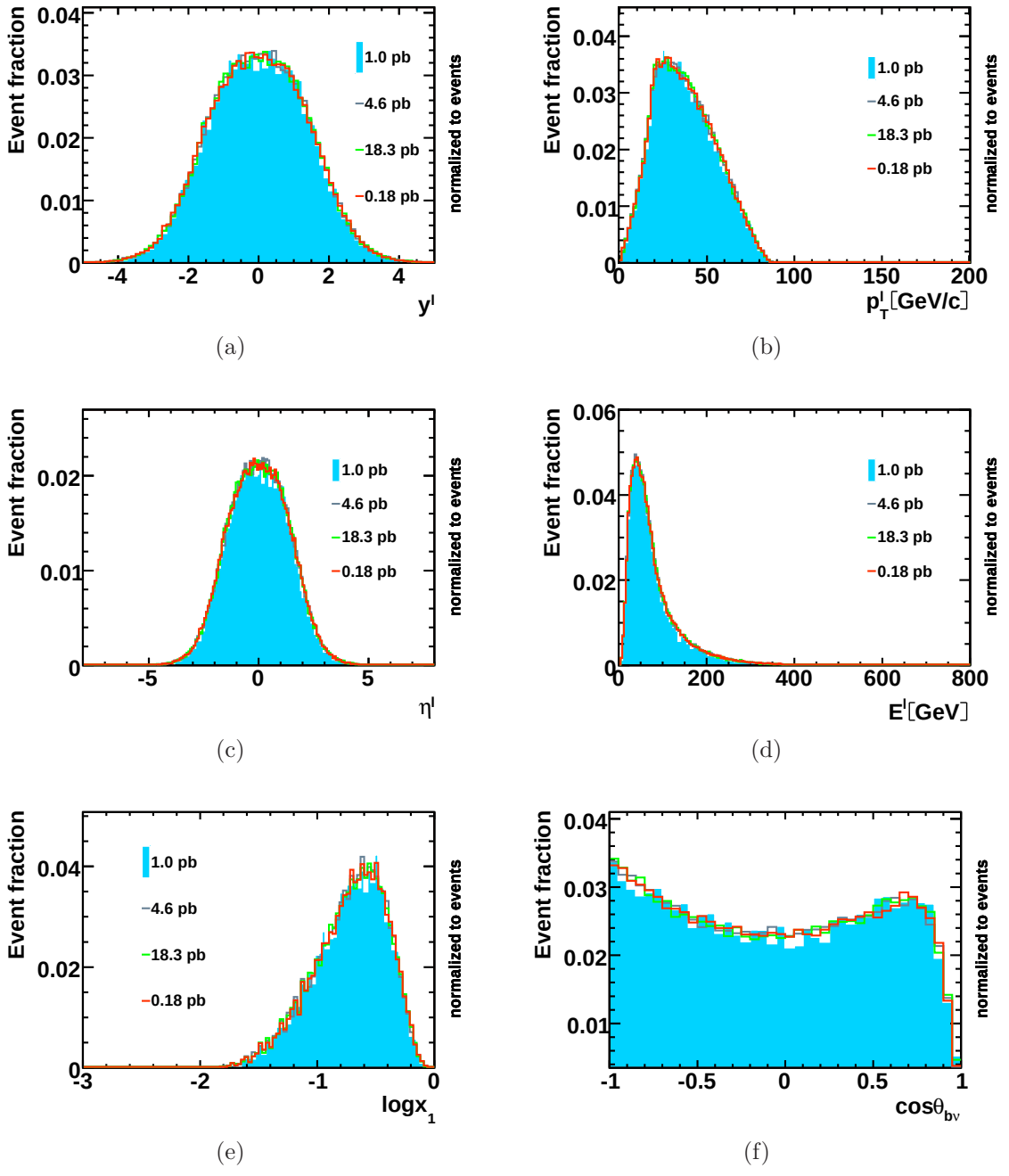

Figure 4.4: (a), (b), (c), (d), (e) and (f) are control plots for checking the kinematics for different values of the coupling constants at parton level. The region filled with blue color belongs to a sample with a cross section of 1 pb, as the one used for this analysis. The former is compared to anomalous top-quark samples with higher or lower cross sections, which corresponds to higher or lower values for the coupling constants. No significant difference can be seen.

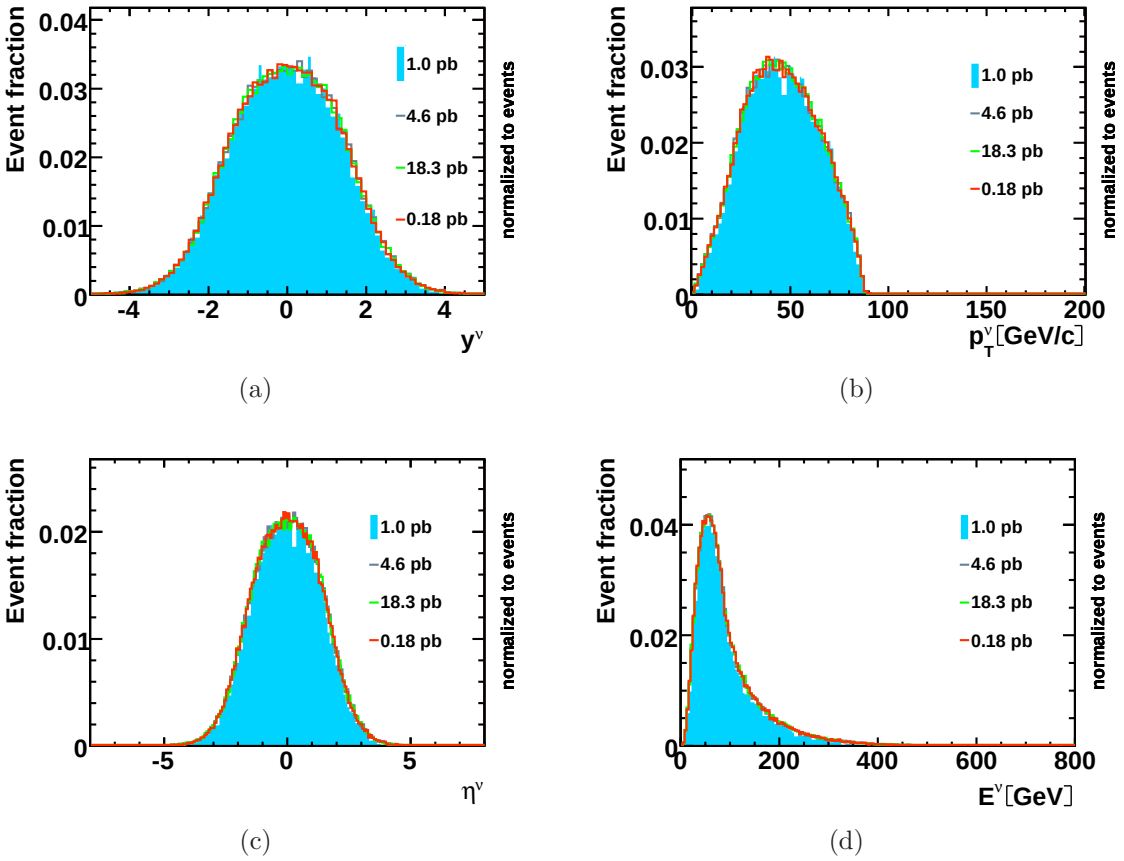

(a) (b)

(c) (d)

Figure 4.5: (a), (b), (c) and (d) are control plots for checking the kinematics for different values of the coupling constants at parton level. The region filled with blue color belongs to a sample with a cross section of 1 pb, as the one used for this analysis. The former is compared to anomalous top-quark samples with higher or lower cross sections, which corresponds to higher or lower values for the coupling constants. No significant difference can be seen.

It has to be mentioned, that the ad-hoc chosen value of the anomalous production cross section does not play any role in the fit-technique used in this study, which will be discussed later in the data analysis.

Figure 4.6 shows the anomalous vertex in the approach of the effective theory, which is applied in TopReX. This vertex corresponds to the term in 4.4. The higher order term is of no interest for this search. Equations 4.5-4.9 define most of the important variables. Further details about the parameters used in the program can be found in references [61, 85].

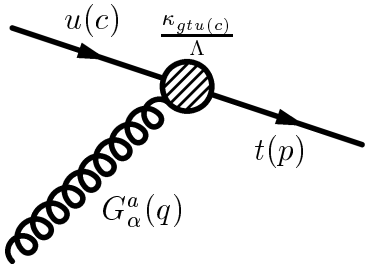

Figure 4.6: $u(c)$-g-t vertex in the effective approach and parametrisation of the ingoing and outgoing fields.

$$g_s t^a \left[\frac{1}{\Lambda}\sigma_{\mu\nu}\hat{H} + \underbrace{\frac{1}{\Lambda^2}\gamma^\mu \left(\hat{X}p^\nu + \hat{Y}q^\nu\right)}_{\text{higher order}} \right] Q^{\mu\nu\alpha} \tag{4.4}$$

$$\begin{aligned} Q^{\mu\nu\alpha} &= q^\mu g^{\nu\alpha} - q^\nu g^{\mu\alpha} && (4.5)\\ \hat{H} &= h_L P_L + h_R P_R && (4.6)\\ P_{L/R} &= \frac{1}{2}\left(1 \pm \gamma^5\right) && (4.7)\\ & && (4.8) \end{aligned}$$

$$\text{for higher-order term} \begin{cases} \hat{X} = x_L P_L + x_R P_R \\ \hat{Y} = y_L P_L + y_R P_R \end{cases} \tag{4.9}$$

q^ν stands for the four-momentum of the gluon, p^ν for the four-momentum of the top quark, while t^a are the Gell-Mann matrices satisfying $Tr\left(t^a t^b\right) = \frac{\delta^{ab}}{2}$. In table 4.3, some of the parameter values used for the MC simulation of the anomalous production channel, are shown.

parameter	value	explanation
ntot	1000000	total event number
decTop(11)	1	anomalous top-quark decay activated
decTop(3)	1	SM decay activated $t \rightarrow bW$
Ipar(31)	1	running top-mass according top-quark width
AN_FL(3)*	1.0	SM value for t-W-b
AN_FR(3)*	0.0	SM value for t-W-b
AN_HL(11)*	0.02337	FCNC t-u-g
AN_HR(11)*	0.02337	FCNC t-u-g
AN_HL(12)*	0.0	FCNC t-c-g
AN_HR(12)*	0.0	FCNC t-c-g
W-boson	0 0 0 0 0 0 1 1 1	W boson decays leptonically

Table 4.3: Some of the TopReX parameters set to special values for the MC simulation of the anomalous top-quark production. All parameters denoted with * concern polarisation coefficients of left/right-handed couplings.

4.4 Modeling of Backgrounds

In this section, the modeling of the complete spectrum of expected processes contributing to the $W+1$ jet bin is discussed. Most of the processes are described using MC simulation, while some background processes are derived from data. A complete list of Monte Carlo samples used in this analysis can be found in Appendix B.

(a) $Wb\bar{b}$ ($c\bar{c}$) (b) Wc

Figure 4.7: Examples of Feynman graphs showing W+heavy flavor background production: (a) illustrates production of a W boson in association to a gluon splitting into a heavy-quark pair. (b) shows the production of a W boson in addition to a c quark.

The background to anomalous top-quark production in the b-tagged lepton+jets sample is dominated by W-boson production in association with heavy-flavor quarks, illustrated in figure 4.7: $Wb\bar{b}$, $Wc\bar{c}$, and Wc production, called W+heavy flavor in the following.

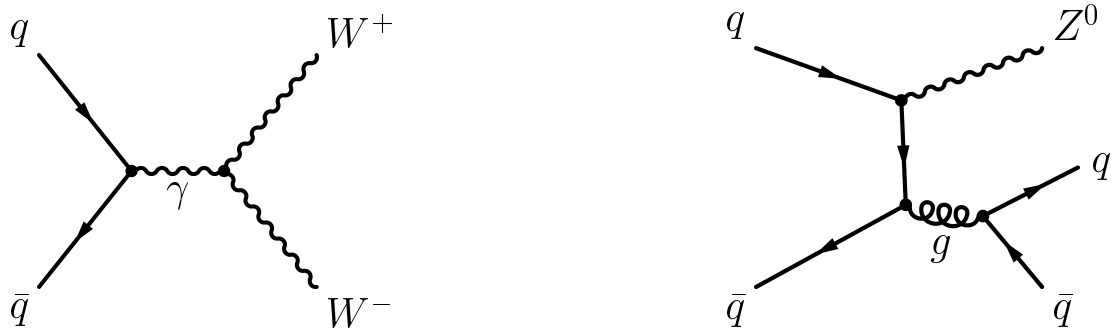

(a) Diboson production (b) Z+jets

Figure 4.8: Examples of (a) diboson and (b) Z+jets background production. Variations of (a) can produce ZZ and WZ events. For Z+jets production, exemplarily illustrated in (b), only leptonic Z-Boson decays are considered.

Additional background sources are SM single top-quark and top-quark pair production being illustrated in figures 1.3 and 1.2, respectively, diboson production (including WW, WZ, and ZZ) whereof an example is given in figure 4.8(a), as well as Z-boson production in association with quarks. The latter is also called Z+jets production and contains leptonically decaying Z bosons. This is demonstrated in figure 4.8(b). W-boson, diboson, and Z-boson events with a light-flavor jet mistakenly tagged as heavy flavor are named mistags.

(a) Jet fakes isolated lepton (b) Semi-leptonic decay

Figure 4.9: Examples of Feynman graphs showing production of QCD backgrounds. In events like (a), a jet can be misidentified as isolated lepton to fake the signature of single top-quark events. In $b\bar{b}$ events, a semi-leptonically decaying b hadron can lead to the same signature as single top-quark events if the lepton is spuriously identified as isolated lepton, as illustrated in (b).

A substantial background arises from QCD-induced multijet events, e.g. direct $b\bar{b}$ production as illustrated in figure 4.9. Those events mimic the signature of W-boson production if a jet (or a lepton from a semileptonic decay) is erroneously identified as an isolated lepton and transverse energy is mismeasured, leading to artificial $\not{E}_{\mathrm{T}}$. These events are called non-W events, due to the fact that no on-shell W boson is

produced.

It has been argued [86, 87], that the modeling of the leading-order contribution to single top-quark production via t-channel with leading-order parton shower MC generators is incapable of representing the measured final states. Figure 1.3(b) shows the leading-order process ($2 \to 2$) with a b quark in the initial state. The former stands for $b+u \to d+t$ or $b+\bar{d} \to \bar{u}+t$. Since the b quark stems from the quark sea, it is described by the corresponding PDF. Nevertheless, the origin of the b quark is a gluon-splitting process, which means that a b-flavored antiquark is expected in the event. This factor has to be considered by the leading-order parton shower programs, which produce the $\bar{b}$ quark through backward evolution, following the DGLAP scheme [88, 89, 90]. However, only the soft part of the transverse momentum distribution of the $\bar{b}$ quark is modeled in a satisfying way, while the pseudorapidity spectrum should not be expanding so far into the forward region.

In this analysis, the modeling of t-channel was improved by matching two different samples, created by the matrix-element generator MADEVENT, whose final-state partons were showered by PYTHIA. The parametrisation of the parton distribution functions was chosen to be CTEQ5L [91].

The first sample, `stop01`, is described by the leading-order (LO) Feynamn diagram in figure 1.3(b), while the second, `stop02`, stands for the most important next-to-leading-order (NLO) contribution and is shown in figure 1.3(c). The LO process is a $2 \to 2$ process ($b+q \to q'+t$), while the NLO is a $2 \to 3$ process ($g+q \to q'+t+\bar{b}$). In the second process, the $\bar{b}$ quark is produced directly in the hard scattering described by the matrix element and suitable to describe the hard part of the p_{T} distribution of the $\bar{b}$ quark.

The exact description of the modeling of SM single top-quark production via s-channel and t-channel can be found in [92, 94].

The $t\bar{t}$ process was simulated using PYTHIA and the cross section of the process was set to be 6.7 ± 0.42 pb, see reference [93]. For the modeling, diboson, simulated events generated with PYTHIA are used, while the W+heavy flavor and Z+heavy flavor backgrounds were simulated using a combination of ALPGEN and PYTHIA.For the samples produced with ALPGEN, the heavy flavor overlap, which takes place due to the randomly generated particles in the showering, is removed. This is of great importance for the b tagging and for the determination of efficiencies, which require a clear separation between the light and heavy flavor samples. In this analysis, the heavy-flavor overlap-removal is done by the jet-based procedure. For the heavy flavor samples, the applied algorithm keeps all events without any heavy quark in the particle list. In case there are heavy quarks in the event, they are assigned to be c or b like, except for the case that there are $c\bar{c}$ or $b\bar{b}$ pairs produced in the parton shower, which lie inside the cone of a reconstructed jet. Moreover, all events from the heavy quark samples are removed, if there is a $c\bar{c}$ or $b\bar{b}$ pair produced on matrix element level and is located in a jet cone.

The QCD background is modeled using two different approaches [95]. The central electron and muon models are obtained from central electron trigger data. The

events are required to pass all kinematic electron cuts but to fail two of the five non-kinematic cuts. Even though their kinematic properties resemble those of W-like events, those events are QCD-enriched, since the non-kinematic criteria serve primarily to filter out QCD-induced multijet events. For the forward electron sample, such a model is not yet available. For this reason, an additional QCD model is introduced, based on the idea that for a QCD event to pass the selection criteria, a jet has to resemble an electron. Hence, events from jet trigger data are required to have a jet with $E_{\mathrm{T}} > 20$ GeV, $0.05 < E_{\mathrm{HAD}}/E_{\mathrm{EM}} < 0.2$, and at least four reconstructed tracks. The latter makes it unlikely that the event contains a real electron. Once a jet is identified as a fake electron, its charge is assigned randomly, and it is further considered as a tight electron.

The event candidates of both approaches have to pass all but the lepton selection criteria and the b-tag requirement to contribute to the corresponding QCD model. Since demanding a tagged jet would cause too low statistics, the b tag in the event has to be faked using taggable jets, this means jets that satisfy $E_{\mathrm{T}} > 10$ GeV, $|\eta| < 2.4$, and $N_{\mathrm{trk}} \geq 2$. Due to the usage of the KIT flavor separator described in reference [96], it is additionally necessary to assign a hypothesis of what kind of quark flavor the jet is, b, c, or light-quark flavor. The probability that a specific quark flavor is assigned to a certain jet is given by the expected flavor composition of the QCD background. This composition is estimated by applying the KIT flavor separator to the $\not\!\!E_{\mathrm{T}} < 15$ GeV sideband of the observed data. In this sideband sample, a flavor composition of 45% b-quark jets, 40% c-quark jets, and 15% light-quark jets is found [97].

In order to describe events with a mistagged light-quark jet, W+light flavor and Z+light flavor events simulated with ALPGEN and showered with PYTHIA are used. Due to the very small fraction of tagged events in this sample, a large amount of this kind of events would be needed in simulation. Thus, the pretag sample is utilized where taggable jets are assigned to be tagged. Real tags are removed from the tagged jet. Each event is weighted by the mistag probability of the jet.

For both QCD and mistag model, the output of the KIT flavor separator is randomly assigned to the jet attributed as tagged. For this purpose template output distributions obtained from jets of simulated events corresponding to the respective quark flavor are utilized.

4.5 Expected Event Yield

In this section, the number of expected events for each process is discussed. The estimation was done with the method called "Method II For You" [98]. This method is used to calculate the normalization of processes in the b-tagged lepton+jets data-sample. First, it is assumed that the composition of the latter is known. Then, the normalization of the processes is calculated sequentially for every process, based each time on the knowledge of the previous normalization factor. Furthermore, each part of the background not perfectly modeled by MC is derived from data.

Therefore, it is necessary to first estimate the MC based processes, which have a theoretically computed or experimentally measured cross section. Combined with information about the luminosity and MC derived efficiencies, one is able to calculate the expected number of events in the sample, given by equation 4.10.

$$N_{p\bar{p}\to X} = \sigma_{p\bar{p}\to X} \cdot \epsilon_{\text{evt}} \cdot \epsilon_{\text{tag}} \cdot \int dt\mathcal{L}. \tag{4.10}$$

X stands for diboson, Z+jets, single top-quark, top-quark-pair[1] and anomalous top-quark production. $\sigma_{p\bar{p}\to X}$ is the theoretical cross section, $\int dt\mathcal{L}$ is the integrated luminosity, ϵ_{evt} is the event detection efficiency derived from MC, ϵ_{tag} is the tagging efficiency. ϵ_{evt} is given by

$$\epsilon_{\text{evt}} = \epsilon_{\text{evt}}^{\text{MC}} \cdot \epsilon_{\text{BR}} \cdot \epsilon_{\text{trigger}} \cdot \frac{\epsilon_{\text{z0}}^{\text{data}}}{\epsilon_{\text{z0}}^{\text{MC}}} \cdot \frac{\epsilon_{\text{leptonidreco}}^{\text{data}}}{\epsilon_{\text{leptonidreco}}^{\text{MC}}}, \tag{4.11}$$

where $\epsilon_{\text{evt}}^{\text{MC}}$ is the detection efficiency obtained from simulated MC events, ϵ_{BR} is the branching ratio of the W-boson. For the case of the leptonic decays of the latter, $\epsilon_{\text{BR}} = 0.324$. $\epsilon_{\text{trigger}}$ stands for the trigger efficiency, which is derived from data, while $\epsilon_{\text{z0}}^{\text{data}}$ and $\epsilon_{\text{z0}}^{\text{MC}}$ are the z-vertex cut-efficiencies in data and MC, respectively. $\frac{\epsilon_{\text{leptonidreco}}^{\text{data}}}{\epsilon_{\text{leptonidreco}}^{\text{MC}}}$ represents the lepton ID and reconstruction efficiency scale-factor.

Based on the above, table 4.4 and table 4.5 show the values used for the calculation of the expected number of events of the anomalous top-quark production for an assumed cross section of 1.0 pb. The tagging efficiency for this case is given by

$$\epsilon_{\text{tag}} = \frac{\sum_j^{events} P_j^{tag}}{N_{pretag}}, \tag{4.12}$$

where N_{pretag} stands for the number of events in the pre-tagged sample and P_j^{tag} is the probability that an event j is tagged, given by

$$P_j^{tag} = 1 - \prod_i^{jets} \left(1 - p_{tag}^i\right), \tag{4.13}$$

while p_{tag}^i stands for the tagging scale factor of the jet i. Since only one jet is expected in the event, $P_j^{tag} = p_{tag}^i = 0.95$. The luminosities for each subdetector used for the calculation are taken from 4.2.

Tables 4.6 and 4.7 show the cut flow for the anomalous top-quark production events in the electron and muon subdetectors, respectively. Muon events in the BMU subdetector were not taken into account, although mentioned in table 4.7. Table 4.8 summarizes the results.

[1]The value of the $t\bar{t}$ production cross-section is based on the calculations in references [99, 100].

subdetector	events	$\epsilon_{\text{trigger}}$	$\frac{\epsilon_{\text{z0}}^{\text{data}}}{\epsilon_{\text{z0}}^{\text{MC}}}$	$\frac{\epsilon_{\text{leptonidreco}}^{\text{data}}}{\epsilon_{\text{leptonidreco}}^{\text{MC}}}$	$\epsilon_{\text{evt}}^{\text{MC}}$ [%]
CEM	23006	0.962	1.085	0.974	2.649
PHX	7043	0.946	1.085	0.937	0.811
CEM	10575	0.913	1.085	0.930	1.218
CMX	5845	0.892	1.085	0.974	0.673

Table 4.4: Events and efficiencies of each subdetector used for the calculation of the number of expected events of the anomalous top-quark production.

subdetector	$\Delta\epsilon_{trigger}$ [%]	$\Delta\epsilon_{\text{z0}}^{\text{data}}$ [%]	$\Delta\frac{\epsilon_{\text{leptonidreco}}^{\text{data}}}{\epsilon_{\text{leptonidreco}}^{\text{MC}}}$ [%]
CEM	0.67	0.50	0.40
PHX	0.27	0.50	0.60
CEM	0.57	0.50	0.73
CMX	0.72	0.50	0.77

Table 4.5: Errors on the efficiencies of each subdetector used for the calculation of the number of expected events of the anomalous top-quark production.

CEM electrons

Cut	1 jet	2 jets	3 jets	all
Tight Di-Lepton Veto	64548	21329	5359	91236
Z Vertex Cut	64539	21323	5359	91221
Z veto	64189	21132	5273	90594
Missing Et	51391	17299	4318	73008
QCD Veto	48194	15762	3866	67822
taggable	33995	13845	3634	51474
b tag = 1	16013	5517	1385	22915

PHX electrons

Tight Di-Lepton Veto	22193	6695	1612	30500
Z Vertex Cut	22192	6695	1612	30499
Z veto	22088	6623	1591	30302
Missing Et	17291	5252	1290	23833
QCD Veto	16023	4520	1085	21628
taggable	11261	4027	1032	16320
b tag = 1	5131	1519	366	7016

Table 4.6: Cut flow table for all events in the electromagnetic calorimeters in the anomalous top-quark sample.

The calculation of the data based background, as well as the calculation of the pretagged samples, can be found in reference [98]. Table 4.9 shows the expected background and signal events in the W+1 jet bin sample, corresponding to an integrated luminosity of 2.2 fb^{-1}.

CMUP muons				
Cut	1 jet	2 jets	3 jets	all
Tight Di-Lepton Veto	28425	9371	2282	40078
Z Vertex Cut	28422	9369	2282	40073
Z veto	28332	9318	2263	39913
Missing Et	23012	7593	1852	32457
QCD Veto	21946	7423	1805	31174
taggable	15569	6540	1671	23780
b tag = 1	7219	2673	637	10529
CMX muons				
Tight Di-Lepton Veto	15898	5083	1230	22211
Z Vertex Cut	15897	5082	1230	22209
Z veto	15846	5058	1216	22120
Missing Et	12747	4111	995	17853
QCD Veto	12592	4027	970	17589
taggable	8790	3590	903	13283
b tag = 1	4090	1403	324	5817
BMU muons				
b tag = 1	3349	1045	271	4665

Table 4.7: Cut flow table for all events in the muon chambers in the anomalous top-quark sample. Muon events in the BMU subdetector were not cosindered in this analysis.

Cut	0 jet	1 jet	2 jets	3 jets	4 jets	≥ 5 jets	all
Total	50981	489390	297250	83461	18735	3895	943712
Good Run	46909	450403	273386	76804	17215	3590	868307
OBSV < 60.0	0	435197	259186	72590	0	0	766973
CMX Good Total	46362	445103	270173	75935	17011	3554	858138
≥ 1 Tight Std. lepton	0	144712	46620	11456	0	0	202788
LooseLepton cut	0	144620	- 46594	11447	0	0	202661
All							
Tight Di-Lepton Veto	0	144134	46458	11409	0	0	202001
Z Vertex Cut	0	144088	46444	11408	0	0	201940
Z veto	0	143450	46084	11263	0	0	200797
Missing Et	0	115045	37490	9203	0	0	161738
QCD Veto	0	109233	34905	8460	0	0	152598
taggable	0	76934	30796	7936	0	0	115666
b tag = 1	0	35802	12157	2983	0	0	50942

Table 4.8: Cut flow table for all events in the anomalous top-quark sample.

Process	Number of Events
t-channel single-top	17.1 ± 2.5
s-channel single-top	7.3 ± 1.1
total single-top	24.4 ± 3.6
$t\bar{t}$	12.3 ± 1.8
$Wb\bar{b}/Wc\bar{c}$	750.9 ± 225.3
Wc	622.3 ± 186.7
total W+heavy flavor	1373.2 ± 412.0
Mistags	769.9 ± 100.5
Non-W	43.0 ± 17.2
Diboson	19.9 ± 2.0
Z+jets	26.6 ± 4.2
total background	2269.3 ± 434.3
anomalous top ($\sigma_{ano} = 1$ pb)	35.3 ± 5.3
total prediction	2304.6 ± 439.6
observation	2472.0 ± 0.0

Table 4.9: Summary of predicted numbers of background and signal events in the selected data sample. Only not correlated uncertainties are included (see section 5.2).

Chapter 5

Data Analysis

In this chapter, the part of this study concerning the actual data analysis is discussed in detail. In section 5.1, all relevant information about the of the neural network used for this search is applied. The systematic uncertainties taken into account are presented in section 5.2, while in section 5.3, the statistical procedure of this analysis is introduced.

5.1 Training of the Neural-Networks

In the search for the anomalous top-quark production, no counting experiment is possible, due to a large number of background events produced by processes, which have similar kinematics as the signal process. Therefore, using a multivariate analysis method (MVA) is highly recommended. For this analysis, a neural network is used. The NN is trained in the $W+1$ jet data set, while the jet has a b tag. The training procedure is discussed in detail in the following section.

5.1.1 Training Samples

For the training of the network, it is necessary to arrange training samples consisting of the relevant modeled physics processes, each with reasonable statistics.

The samples used to train the neural networks are composed in such a way that the respective anomalous top-quark production process contributes 50% to the total number of events. The relative fractions of all considered background processes are given by the respective number of expected events quoted in table 4.9.

A list of all used processes, as well as their contributions to the training samples is given in table 5.1.

Process	
	W+1 jet ; 1 b tag
anomalous top	50.0%
t-channel single-top	0.4%
s-channel single-top	0.2%
$t\bar{t}$	0.3%
$Wb\bar{b}$	11.9%
$Wc\bar{c}/Wc$	21.4%
mistags	14.9%
Diboson	0.4%
Z+jets	0.5%

Table 5.1: Composition of the training samples used to train the neural networks to discriminate anomalous top-quark events. The contributions of the respective anomalous top-quark events is 50% of the complete training sample. The relative fractions to the background category are given by table 4.9. The absolute fractions are determined by the requirement that the contributions of all background processes sum up to 50%.

5.1.2 Input Variables

Before the training, the input variables are preprocessed as discussed in section 3.4.2 and the respective correlations to the target are determined, providing an ordered list of input variables being presented in section 5.1.2. Only variables with a significance larger than a certain threshold are utilized for the training.

For all neural-network trainings mentioned above, three categories of input variables are used: some are directly measured in the detector, others are reconstructed out of measured properties, and a few are calculated by advanced algorithms like the KIT flavor separator described in reference [96]. Furthermore, some quantities need the knowledge about the four-vector of the top quark whose reconstruction is described below.

Top-Quark Reconstruction

It is essential to reconstruct the top quark properly from the particles originating from its decay in order to use variables, which are based on the properties of the top quark, for the neural-network training. The top quark, as mentioned in 1.1.2, decays into a W boson and a b quark. Since in this analysis only the leptonic decay-signature of the W boson is of interest, one has to reconstruct the latter based on the charged lepton and the missing energy, which stands for the neutrino signature in the event. The charged lepton is reconstructed using the information from the calorimeter and the track to get its momentum and energy. The curvature of the track determines the charge of the lepton. Reconstructing the neutrino is a more

complicated case. Due to the fact that the neutrino does not interact with the matter in the detector in a way that it can be directly detected, one has to use the information obtained from the lepton in combination with $\vec{\not{E}}_{\mathrm{T}}$. $\vec{\not{E}}_{\mathrm{T}}$ is assigned to the transverse components $p_{\mathrm{x},\nu}$ and $p_{\mathrm{y},\nu}$ of the neutrino four-momentum $\mathbf{p}_\nu$. As a result, the only parameter of $\mathbf{p}_\nu$ that remains undefined is the z component of the neutrino momentum $p_{\mathrm{z},\nu}$. The latter is obtained by using a quadratic constraint of the W-boson decay kinematics, assuming a leptonically decaying W boson and a massless neutrino:

$$(\mathbf{p}_W)^2 = (\mathbf{p}_e + \mathbf{p}_\nu)^2 = M_W^2, \tag{5.1}$$

where $\mathbf{p}_i$ stands for the four momentum of the corresponding particle $i = W, e, \nu$ and $M_W = 80.4$ GeV/c^2.

There are two in general complex solutions for $p_{\mathrm{z},\nu}$. In case the solutions are real, the solution with the smaller absolute value is chosen. This decision is motivated by MC studies within searches for single top-quark and $t\bar{t}$ production. The latters showed that the choice is justified for more than 70% of all events.

$p_{\mathrm{z},\nu}$ is then given by:

$$p_{\mathrm{z},\nu}^{\pm} = \frac{\mu p_{\mathrm{z},\ell}}{E_\ell^2 - p_{\mathrm{z},\ell}^2} \pm \sqrt{\frac{(\mu p_{\mathrm{z},\ell})^2}{\left(E_\ell^2 - p_{\mathrm{z},\ell}^2\right)^2} - \frac{E_\ell^2 p_{\mathrm{T},\nu}^2 - \mu^2}{E_\ell^2 - p_{\mathrm{z},\ell}^2}}, \tag{5.2}$$

$$\text{where } \mu = \frac{M_W^2}{2} + \cos(\Delta\phi)\, p_{\mathrm{T},\ell} p_{\mathrm{T},\nu} \tag{5.3}$$

and $\Delta\phi$ is the azimuthal angle difference between charged lepton and missing transverse energy.

In some cases, the solutions for $p_{\mathrm{z},\nu}$ may turn out to be complex due to the mismeasurement of $\vec{\not{E}}_{\mathrm{T}}$. This is analogous to $M_{\mathrm{T},W} > M_W$. Considering only the real part of the solution would not satisfy equation 5.1 anymore. Since a mismeasurement of $\vec{\not{E}}_{\mathrm{T}}$ is assumed, one cannot longer take $\not{E}_{\mathrm{T,x}}$ and $\not{E}_{\mathrm{T,y}}$ to be the components of the neutrino momentum. If $M_{\mathrm{T},W}$ is fixed to be $M_{\mathrm{T},W} = M_W$, which corresponds to a vanishing of the square root in equation 5.2, a quadratic dependence of $p_{\mathrm{x},\nu}$ on $p_{\mathrm{y},\nu}$ appears. Hence, there are in general two different and sometimes complex solutions for $p_{\mathrm{x},\nu}$. Furthermore, it is assumed that $\vec{\not{E}}_{\mathrm{T}}$ is not completely mismeasured. Hence, a corrected solution for $p_{\mathrm{x},\nu}$ and $p_{\mathrm{y},\nu}$ may be found, that is as close as possible to the actual $\vec{\not{E}}_{\mathrm{T}}$. The difference is defined as:

$$\delta(p_{\mathrm{x},\nu}) := \sqrt{\left(p_{\mathrm{x},\nu} - \not{E}_{\mathrm{T,x}}\right)^2 + \left(p_{\mathrm{y},\nu} - \not{E}_{\mathrm{T,y}}\right)^2}. \tag{5.4}$$

δ is being minimized with respect to $p_{\mathrm{x},\nu}$, in which we only allow $p_{\mathrm{x},\nu}$ to be in a range where $p_{\mathrm{y},\nu}$ does not become complex. In the general case two different values for δ are found, since there are two solutions for $p_{\mathrm{y},\nu}$. If so, the solution for $p_{\mathrm{x},\nu}$ and $p_{\mathrm{y},\nu}$ is chosen, which is as close as possible to the measured $\vec{\not{E}}_{\mathrm{T}}$, that is the smaller δ.

rank	variable	relative significance (in σ)	node number
1	$M_{\ell\nu b}$	129	2
2	KIT flavor separator	85	3
3	$M_{\mathrm{T},\ell\nu\mathrm{b}}$	25	10
4	$M_{\mathrm{T,W}}$	28	6
5	$\Delta R(\ell, j)$	21	14
6	$Q_\ell \cdot \eta_{\ell\nu b}$	20	5
7	$\Delta\phi(j, \vec{\not{E}}_{\mathrm{T}})$	13	21
8	$p_{\mathrm{T,b}}$	11	4
9	$p_{\mathrm{T},\ell}$	10	8
10	$y_{\ell\nu\mathrm{b}}$	8	7
11	η_W	5	13
12	η_ℓ	5	15
13	aplanarity	3	18
14	$\Delta\phi(\ell, \vec{\not{E}}_{\mathrm{T}})$	3	20

Table 5.2: Set of discriminating variables used for the training of the neural network in the W+1-jet bin with 1 b tag. The quoted relative significances are determined as described in section 3.4.3, i.e. calculated in terms of reduced matrices. The node numbers correspond to the values on the axes of the correlation matrix, presented in figure 5.2.

Relevance and Correlation of Input Variables

While about 30 variables have initially been investigated, 20 of the formers were found suitable for the training of the neural networks. However, only those variables, 14 in number, that show a significance larger than three standard deviations in discriminating signal and background were finally kept. These variables, passing the cut on the significance ($\geq 3\sigma$), are quoted in table 5.2.

Variables which can be measured directly are: the tranverse momentum and the pseudorapidity of the charged lepton, $p_{\mathrm{T},\ell}$ and η_ℓ, the transverse momentum of the b-quark jet, $p_{\mathrm{T,b}}$, the difference in azimuth angle between the jet and $\vec{\not{E}}_{\mathrm{T}}$, $\Delta\phi(j, \vec{\not{E}}_{\mathrm{T}})$, and between lepton and $\vec{\not{E}}_{\mathrm{T}}$, $\Delta\phi(\ell, \vec{\not{E}}_{\mathrm{T}})$, and the distance in the η-ϕ plane between the charged lepton and the jet, $\Delta R(\ell, j)$.

Based on the W boson reconstruction, we define two input variables: the transverse mass and the pseudorapidity of W boson, $M_{\mathrm{T,W}}$ and η_W. From the reconstructed top quark we use the following quantities: the mass, the transverse mass and the rapidity of the reconstructed top quark, $M_{\ell\nu b}$, $M_{\mathrm{T},\ell\nu b}$ and $y_{\ell\nu b}$. The transverse mass is given by $M_{\mathrm{T}}^2 = M^2 + p_{\mathrm{T}}^2$, while the rapidity is defined as $y = \tanh^{-1} \frac{p_z}{E}$, where p_z and E are the momentum in the beam direction and the energy of the given particle, respectively. In addition, we calculate $Q_\ell \cdot \eta_{\ell\nu b}$, which is the product of the charge of the lepton Q_ℓ multiplied by the the pseudorapidity of the reconstructed

top quark. $Q_\ell \cdot \eta_{\ell\nu b}$ is a variable introduced especially for the search for anomalous top-quark production, after studying its discriminating ability at parton level. These studies showed that $Q_\ell \cdot \eta_{\ell\nu b}$ would have the potential to distinguish very well between the different SM-top-quark-production processes and the anomalous top-quark-production process, due to the latter's $2 \rightarrow 1$ signature. This is demonstrated in figure 5.1.

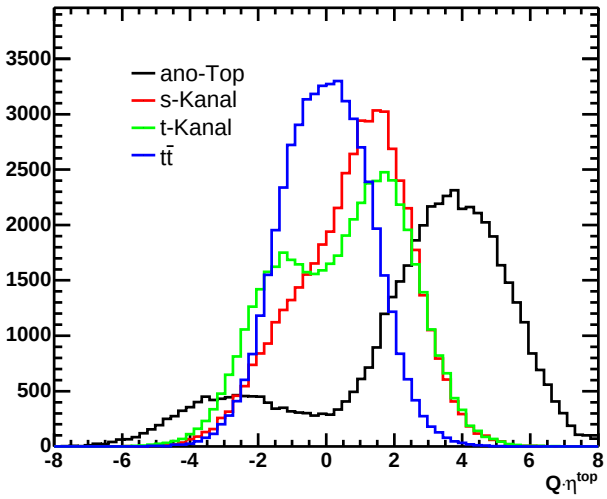

Figure 5.1: $Q_\ell \cdot \eta_{\ell\nu b}$ alias $Q \cdot \eta^{\text{top}}$, studied at parton level. $Q_\ell \cdot \eta_{\ell\nu b}$ is the product of the charged lepton multiplied by the pseudorapidity of the top-quark and is a variable introduced especially for the search for anomalous top-quark production.

An additional input variable is the output of the KIT flavor separator, introduced in section 3.4.5. To describe the event shape in general we use the aplanarity which is defined by $\frac{3}{2}$ of the smallest eigenvalue of the momentum tensor constructed from the b-quark jet, the charged lepton and the reconstructed neutrino.

The most important variable in the neural network with a contribution of 129σ, is $M_{\ell\nu b}$. The second variable to play a significant role in the NN-training, is the output of the KIT flavor separator. The next two input variables to follow in order of significance are $M_{\text{T},\ell\nu b}$ and $M_{\text{T,W}}$, which go with a similar significance into the training, namely 25σ and 28σ, respectively. $\Delta R(\ell, j)$ is the fifth best variable capable of distinguishing between background and signal events.
The sixth variable in turn is $Q_\ell \cdot \eta_{\ell\nu b}$. Unfortunately, after the reconstruction level, the variable lost a great deal of its promising potential. However, it still proved out to be among the six most important input variables and goes in the NN-training with a relative significance of 20σ.
Variables $\Delta\phi(j, \vec{\not{E}}_{\text{T}})$, $p_{\text{T,b}}$, $p_{\text{T},\ell}$ and $y_{\ell\nu\text{b}}$ occupy the four next significant nodes in the network. Furthermore, both η_W and η_ℓ contribute with 5σ to the training. The last two variables to have an impact on the discriminating ability of the NN are the

aplanarity and $\Delta\phi(\ell, \vec{\not{E}}_{\mathrm{T}})$.

Figure 5.2 shows the correlation between the variables used for the training of the neural network. The numbers 2-21 on the axes correspond to the 20 input variables, 14 of which survived the cut of $\geq 3\sigma$ in relative significance and have been already discussed. The rest of the variables that were used are shortly introduced below:

- node 17: the scalar sum of transverse energies $H_{\mathrm{T}} = E_{\mathrm{T},jet} + p_{\mathrm{T},\ell} + \not{E}_{\mathrm{T}}$ where $E_{\mathrm{T},jet}$ is the transverse energy of the b-quark jet
- node 16: the pseudorapidity of the b-quark jet η_j
- node 12: the transverse energy of the b-quark jet $E_{\mathrm{T},jet}$
- node 11: the sphericity, defined by the eigenvalue of the sphericity tensor $S_{ij} := \frac{\sum_{k=1}^{N} p_i^k p_j^k}{\sum_{k=1}^{N} \left|p^k\right|^2}$, where i and j denote the coordinates x, y and z, and the sum goes over all N objects of the event, in this case the b-quark jet, the charged lepton and the neutrino
- node 19: $\Delta\phi$ between the charged lepton and the b-quark jet $\Delta\phi(\ell, j)$
- node 9: the cosine of the polar angle between the reconstructed W boson and the direction of the top quark $\cos\Theta(W,t)_{\mathrm{lab}}$ as seen in the lab-frame

Node 1 stands for the bias node. The quality of the correlation can be extracted according to the spectrum on the right side of the plot. For example, one can see that the most correlated variables in the training are: $p_{\mathrm{T,b}}$-$M_{\ell\nu b}$, $p_{\mathrm{T,b}}$-$E_{\mathrm{T},jet}$, $p_{\mathrm{T,b}}$-$M_{\mathrm{T}\ell\nu b}$, $M_{\ell\nu b}$-$E_{\mathrm{T},jet}$, $\cos\Theta(W,t)_{\mathrm{lab}}$-$y_{\ell\nu b}$, $\cos\Theta(W,t)_{\mathrm{lab}}$-$\eta_W$, $\cos\Theta(W,t)_{\mathrm{lab}}$-$\eta_\ell$, η_W-$y_{\ell\nu b}$, η_W-η_ℓ and $M_{\mathrm{T}\ell\nu b}$-H_{T}. Strong correlated input variables imply a degradation of the discriminating power of the neural network. As a consequence, this neural network promises to perform properly from this aspect, since most of the variables seem to lack in high correlation to each other.

As mentioned above, seven more variables were investigated before setting up the final training, but were later on discarded and, for the sake of completeness, they will also be presented at this point. Those variables are the following: the transverse momentum of the W boson $p_{\mathrm{T,W}}$, the cosine of the angle between the charged lepton and the beam direction $\cos\Theta(\ell, beam)_{\mathrm{lab}}$ as seen in the lab frame, the transverse momentum of the reconstructed top-quark $p_{\mathrm{T},\ell\nu b}$, the cosine of the helicity angle of the W-boson decay $\cos\theta^*$, where θ^* is defined as the angle between the momentum of the charged lepton in the W rest-frame and the momentum of the W boson as seen in the top-quark rest-frame. Moreover, the pseudorapidity of the reconstructed top-quark $\eta_{\ell\nu b}$, the cosine of the angle between the W boson and the top quark $\cos\Theta(W,t)_{\mathrm{t}}$ as seen after a boost in the top-quark rest-frame and the cosine of the angle between the charged lepton and the W boson $\cos\Theta(\ell, W)_{\mathrm{W}}$ observed from a

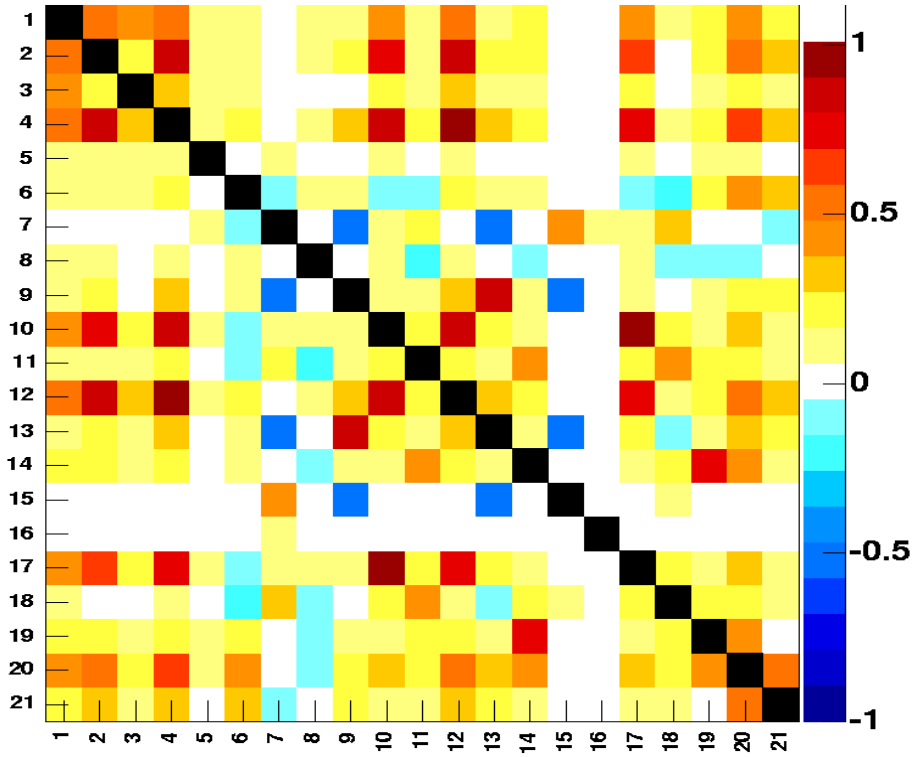

Figure 5.2: Correlation matrix of the input variables used for the NN-training. The numbers on the axes correspond to the 20 input variables for the training (numbers 2-21), 14 of which have passed the cut of $\geq 3\sigma$ in relative significance. Node 1 stands for the bias node. The correlation can be extracted according to the spectrum on the right side of the plot.

spectator in the rest frame of the W boson.

The distributions of the input variables of the network in the W+1-jet bin with 1 b tag, normalized to unit in order to compare the shape, can be found in figures 5.3-5.5. The spapes of the rest of the investigated input variables, those which were either not found suitable for the training or did not survived the 3σ cut, are presented in figures 5.6-5.8.

As one can see in figure 5.3(a), the peak at the reconstructed top-quark mass is broadened by the resolution for single top-quark events. More intense is the effect on the $t\bar{t}$ process, which has an even broader distribution, due to wrong assigned jets. Moreover, W+jets events peak at low values.
The KIT flavor separator, shown in figure 5.3(b), separates well the anomalous and SM top-quark processes from Wc and $Wq\bar{q}$ events, but the separation is limited when it comes to $Wb\bar{b} + Wc\bar{c}$ and QCD events.
$M_{\mathrm{T},W}$, presented in figure 5.3(d), separates QCD and Z+jets from processes with real W bosons. The $t\bar{t}$ events have a broad distribution with a long tail, peaking in

the overflow bin.
$\Delta R(\ell, j)$, shown in figure 5.4(a) is able to separate mainly QCD from the other processes, due to QCD events peaking at higher values.
Figure 5.4(d) shows $p_{\mathrm{T,b}}$. All top-quark production channels in this plot have harder jets in the transverse plane than the other processes. Especially $t\bar{t}$ exhibits a broad distribution over the high p_{T} values.
In the plot in figure 5.5(a), showing $p_{\mathrm{T},\ell}$, one can see that the distribution of QCD and Z+jets events is much softer than the other processes. While $t\bar{t}$ events have a broader distribution, expanding also over the high p_{T} values of $100 - 150$ GeV/c, the SM and FCNC single top-quark production distributions are very much alike.
The aplanarity plot in figure 5.5(e) shows also a softer distribution of the QCD and Z+jets events than the rest of the processes involved in the training of the neural network.
Figure 5.5(f) demonstrates the ability of $\Delta\phi(\ell, \vec{\not{E}}_{\mathrm{T}})$ to separate QCD and Z+jets from the other distributions, since the latters peak at higher $|\Delta\phi|$ values. While W+heavy jets and $t\bar{t}$ events are mostly accumulated at the region $|\Delta\phi| > 2.5$, the anomalous and single top-quark production events pile up mainly within the area of $1.5 < |\Delta\phi| < 2.5$.

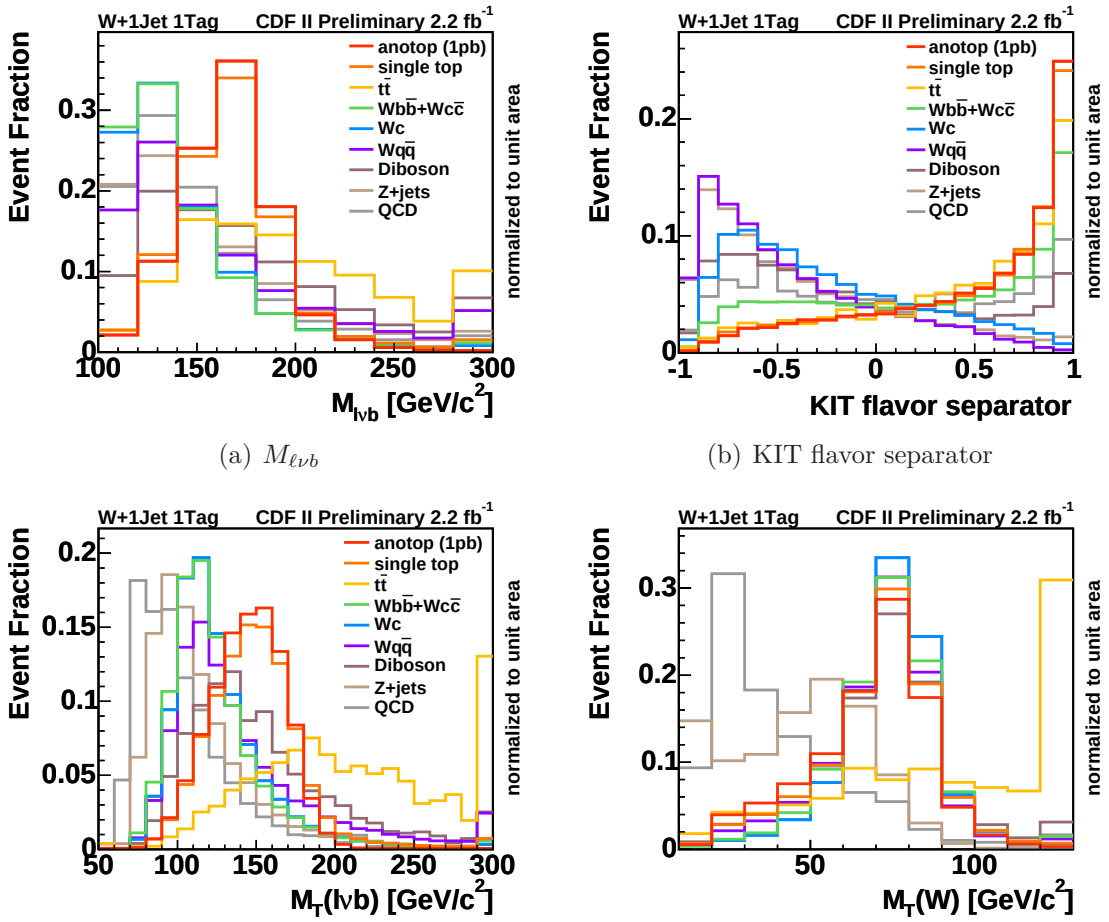

(a) $M_{\ell\nu b}$

(b) KIT flavor separator

(c) $M_{\mathrm{T}\ell\nu b}$

(d) $M_{\mathrm{T},W}$

Figure 5.3: The four most important input variables of the network: (a) $M_{\ell\nu b}$, (b) the neural-network b-tag output of the selected b-quark jet of the top-quark decay, (c) the transverse mass of the reconstructed top quark, $M_{\mathrm{T}\ell\nu b}$ (d) the transverse W-boson mass $M_{\mathrm{T},W}$.

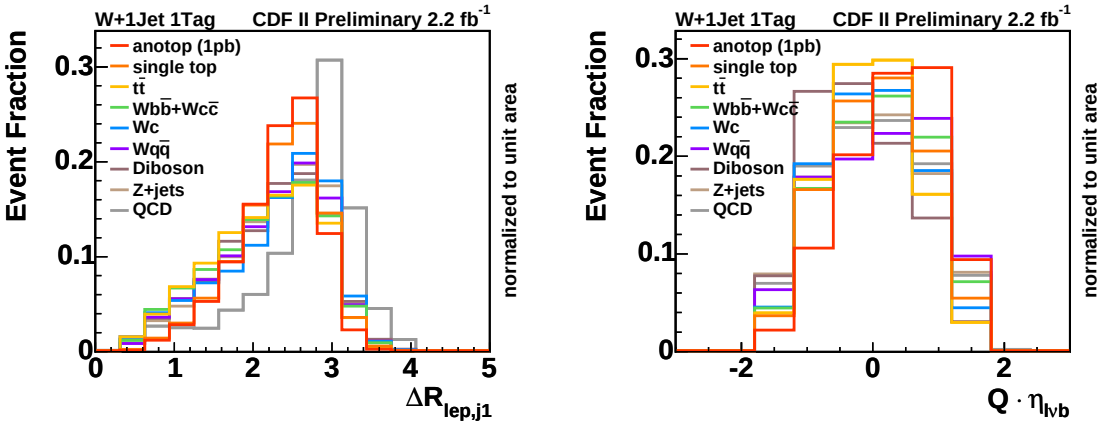

(a) $\Delta R(\ell, j)$ (b) $Q_\ell \cdot \eta_{\ell\nu b}$

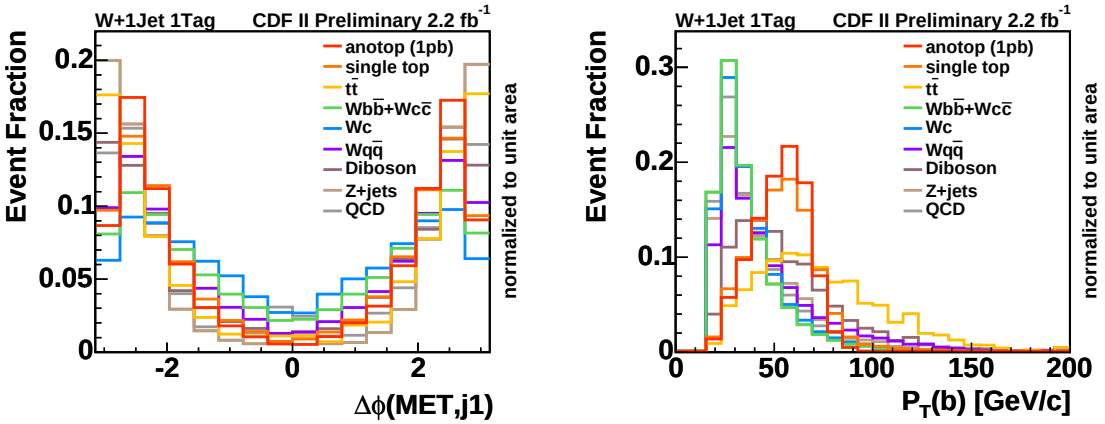

(c) $\Delta\phi(j, \not\!\!E_{\mathrm{T}})$ (d) $p_{\mathrm{T,b}}$

Figure 5.4: The input variables five to eight of the network.

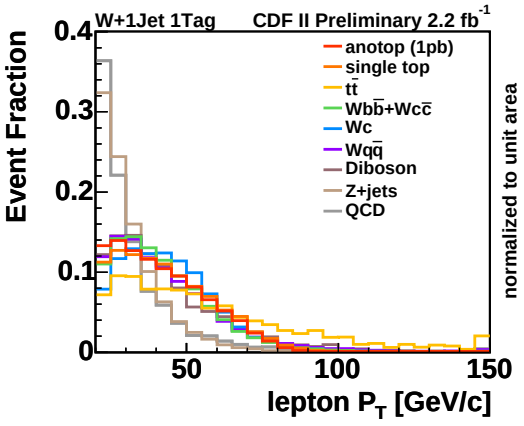

(a) $p_{\mathrm{T},\ell}$

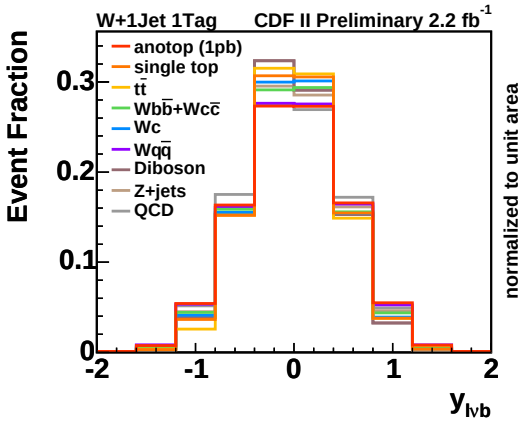

(b) $y_{\ell\nu b}$

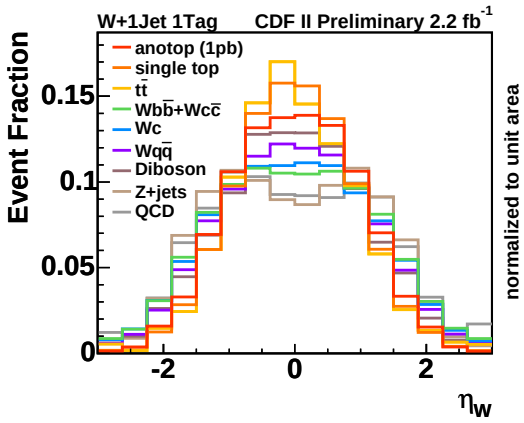

(c) η_W

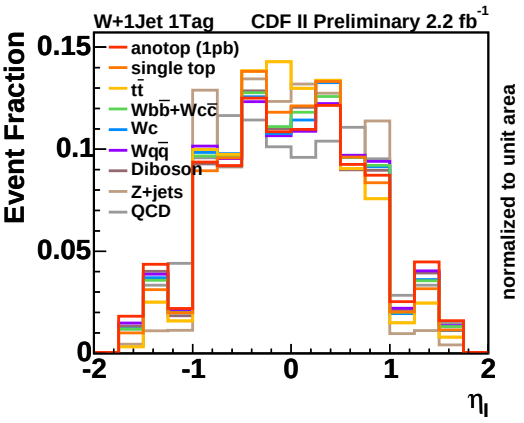

(d) η_ℓ

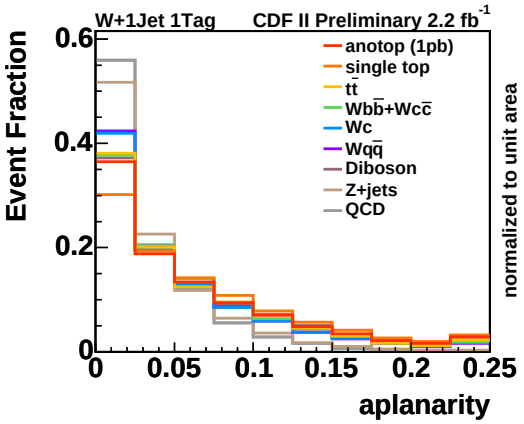

(e) aplanarity

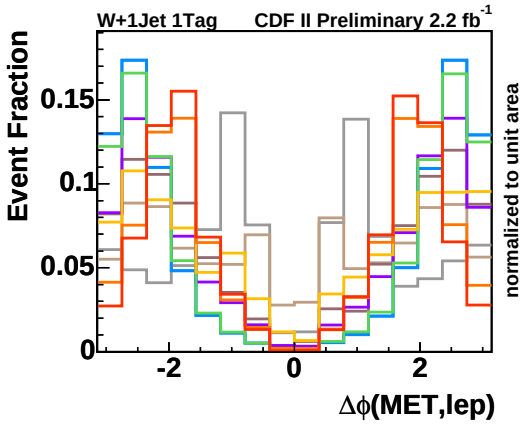

(f) $\Delta\phi(\ell, \vec{\not\!\!E}_{\mathrm{T}})$

Figure 5.5: The input variables nine to fourteen of the network.

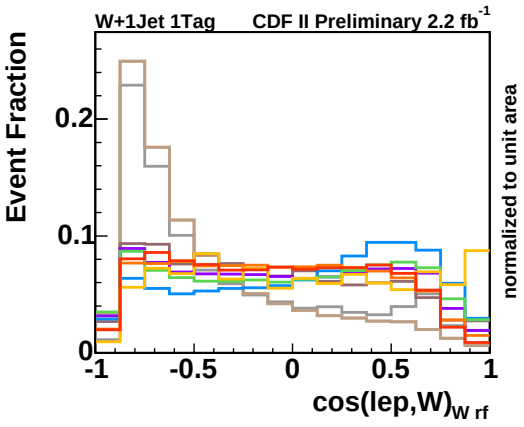

(a) $\cos\Theta(\ell, W)_{\mathrm{W}}$

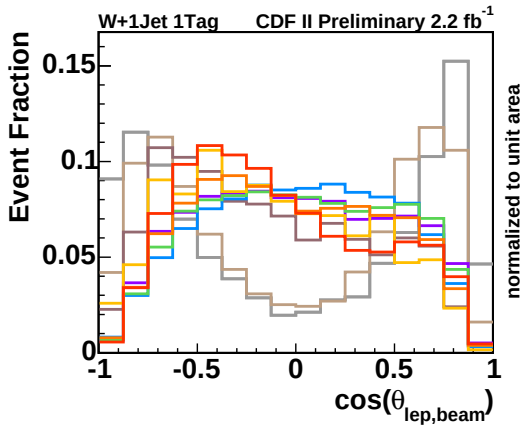

(b) $\cos\Theta(\ell, beam)_{\mathrm{lab}}$

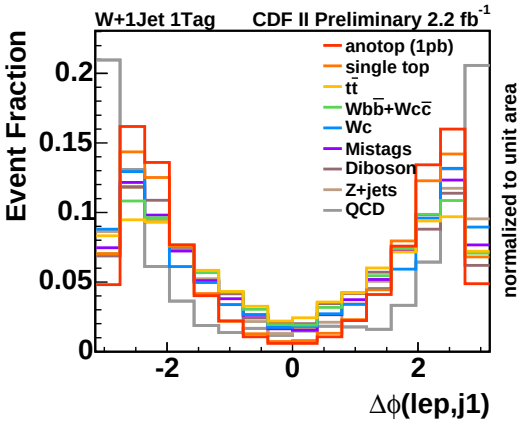

(c) $\Delta\phi(\ell, j)$

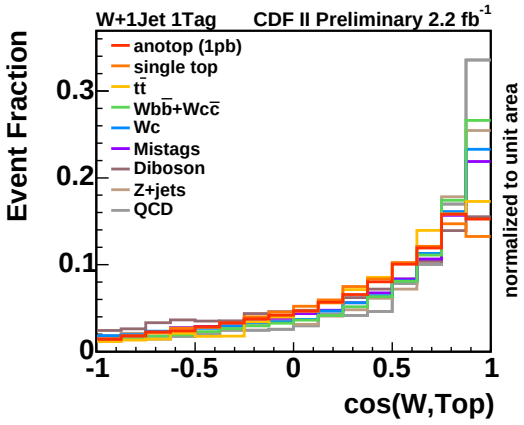

(d) $\cos\Theta(W, t)_{\mathrm{lab}}$

Figure 5.6: Input variables investigated for the training of the neural network, but were finally rejected.

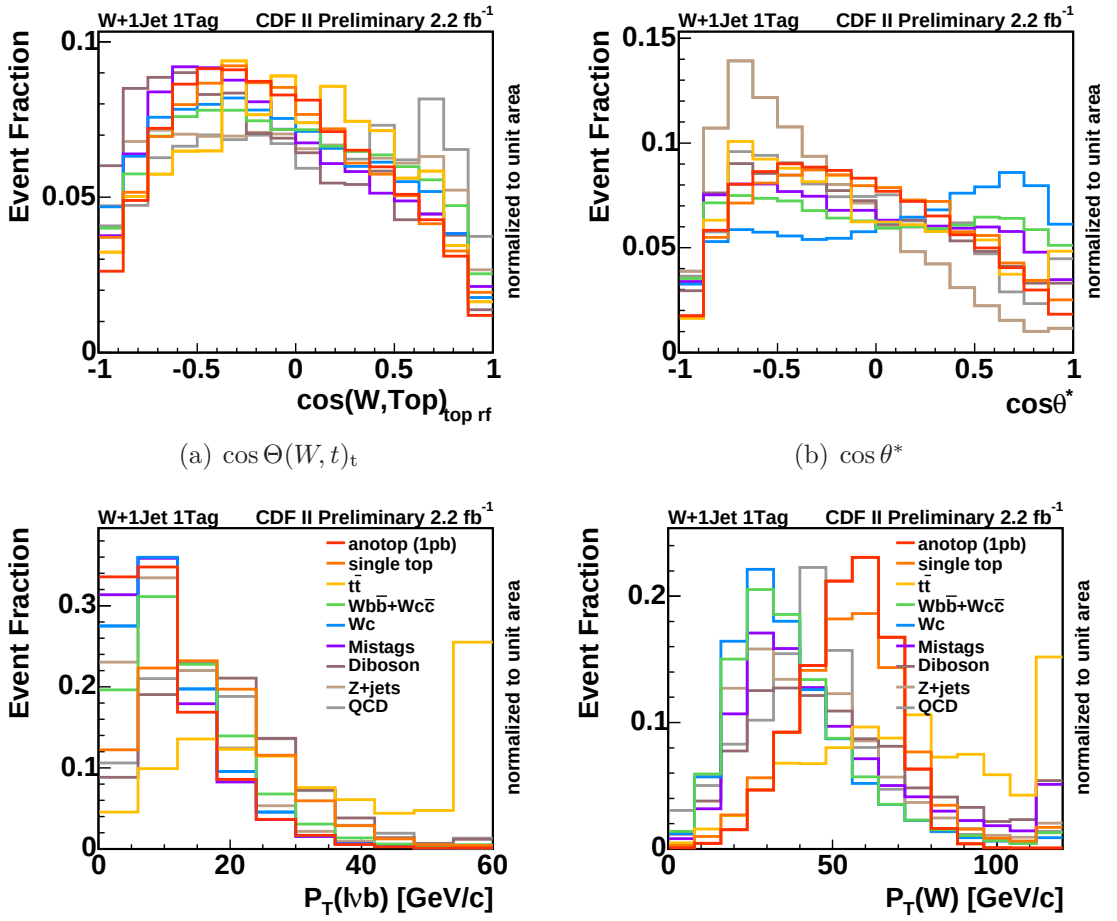

(a) $\cos\Theta(W,t)_{\mathrm{t}}$ (b) $\cos\theta^*$

(c) $p_{\mathrm{T},\ell\nu b}$ (d) $p_{\mathrm{T,W}}$

Figure 5.7: Input variables investigated for the training of the neural network, but were finally rejected.

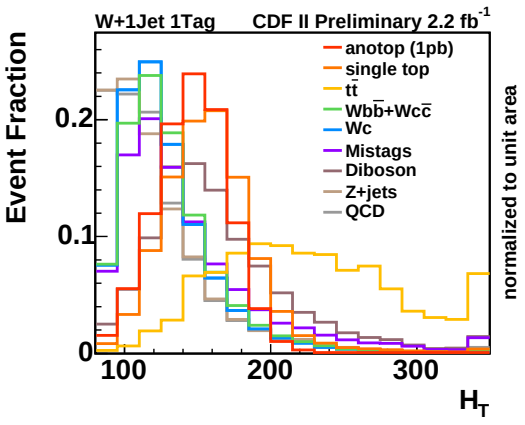

(a) H_{T}

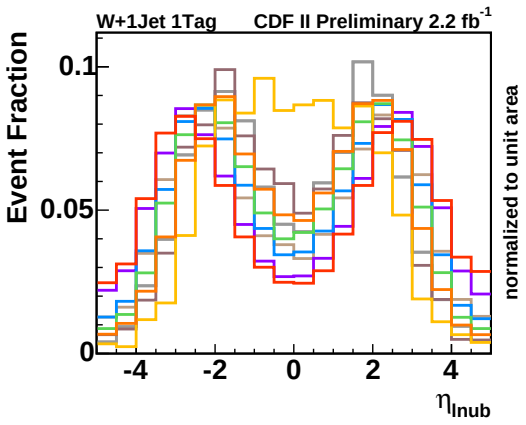

(b) $\eta_{\ell\nu b}$

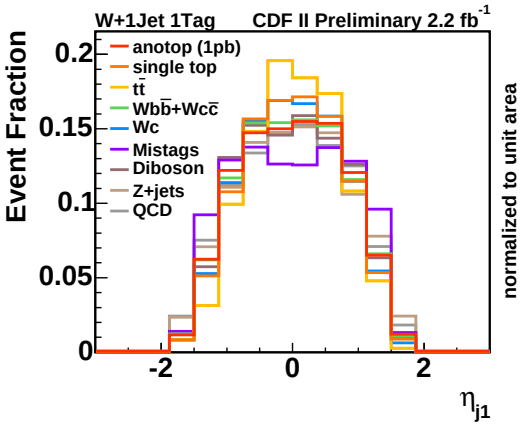

(c) η_j

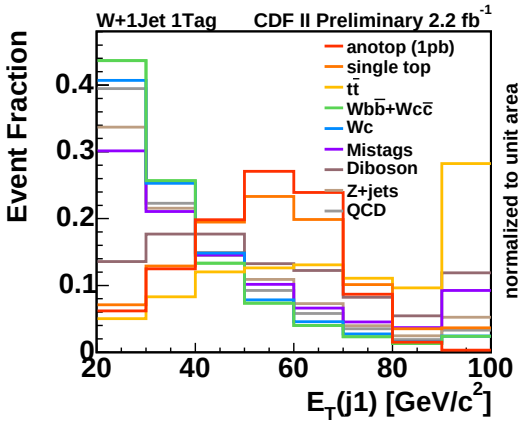

(d) $E_{\mathrm{T},jet}$

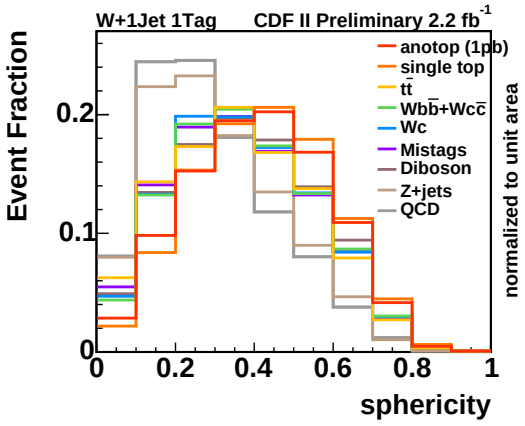

(e) sphericity

Figure 5.8: Input variables investigated for the training of the neural network, but were finally rejected.

Comparison between Observation and Simulation

Since the neural network is trained with simulated events, it is crucial to check if the input variables are modeled correctly. Hence it is necessary to compare the shape of each input variable in observed events with the shape obtained by modeled data embracing the background models described in section 4.4. For this comparison, the histogram templates for each process are scaled in such a way that they contribute according to the number of expected events for this process. To obtain a realistic estimate of the W+heavy flavor fractions in the $W + 1$ jet sample we perform a fit to the KIT flavor separator distribution. The processes included in the fit are those given in table 4.9. The mean number of events for each process is constrained to its expectation, except for the processes $Wb\bar{b}/Wc\bar{c}$ and Wc, which we let float as free parameters. The fit, see figure 5.9, returns scale factors for the different processes which we use for the data-MC comparison.This is the case for $Wb\bar{b}/Wc\bar{c}$ where we find $k = 1.29 \pm 0.08$, Wc $k = 1.01 \pm 0.16$ and mistags $k = 0.87 \pm 0.10$. These scale factors are applied to the estimated event yield quoted in table 4.9. The resulting compound model is used for the data-MC comparison. These scale factors are *not* used for the final fit when searching for anomalous single-top production. The comparisons of the distributions of the input variables of the network can be found in figures 5.10 to 5.12. KS and χ^2 tests were performed in order to validate the quality of the variables. One can see from the results, attached to each plot, that variables like $M_{\ell\nu b}$ and $p_{\mathrm{T,b}}$ are not so well modelled as η_W, $y_{\ell\nu b}$ and the output of the flavor separator. However, we find all in all a good agreement between our compound model and the observation.

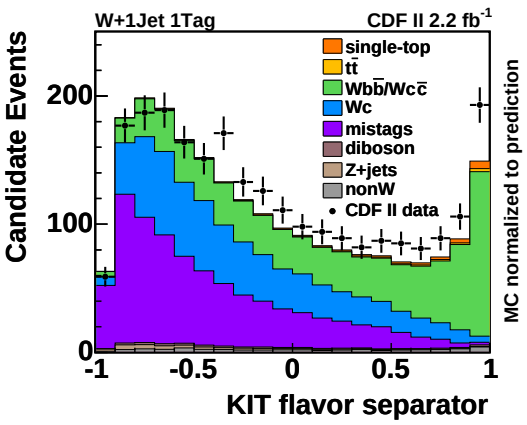

(a)

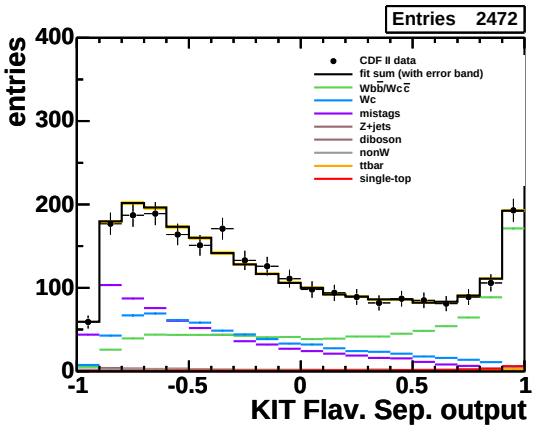

(b)

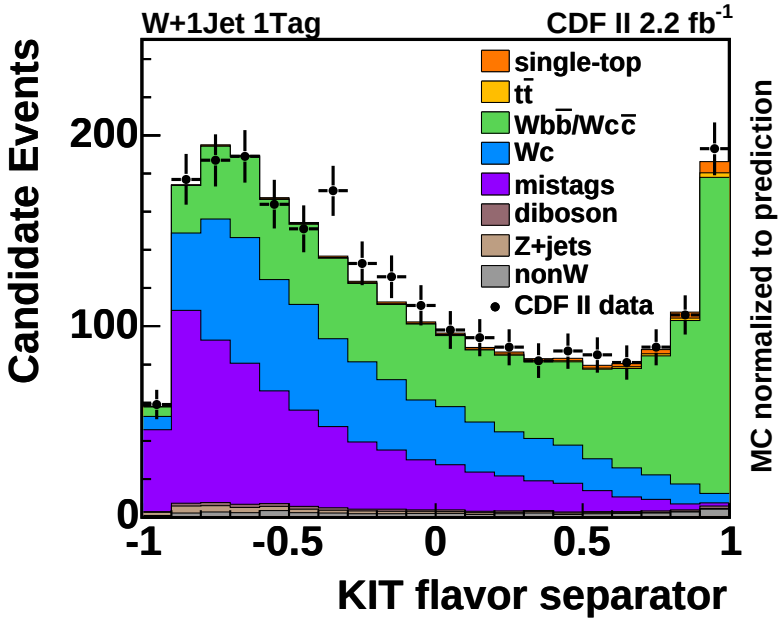

(c)

Figure 5.9: Fit on the KIT flavor separator distribution. (a) shows the distribution of the KIT flavor separator normalized to the prediction. (b) shows the fit on the KIT flavor separator distribution. (c) The scale factors obtained by the fit are applied to the distribution of the KIT flavor separator.

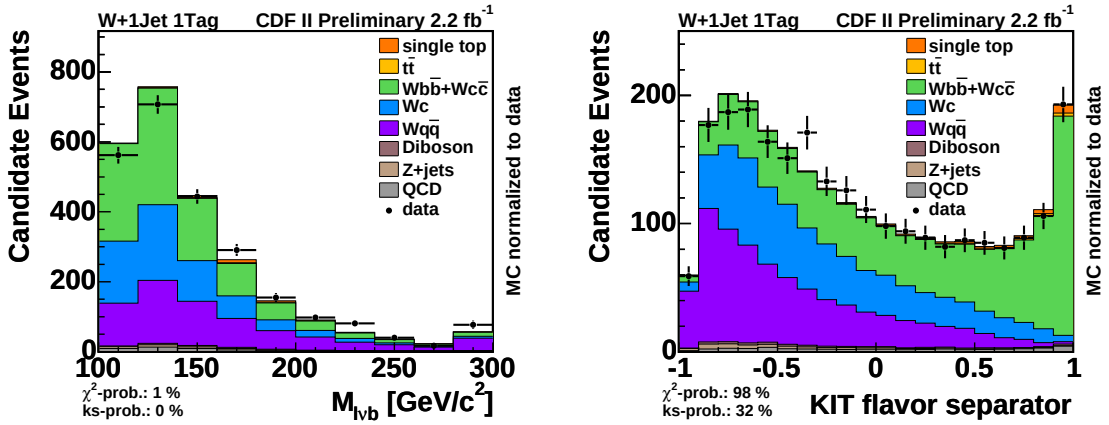

(a) $M_{\ell\nu b}$ (b) KIT flavor separator

(c) $M_{\mathrm{T}\ell\nu b}$ (d) $M_{\mathrm{T},W}$

Figure 5.10: The four most important input variables of the network: (a) $M_{\ell\nu b}$, (b) the neural-network b-tag output of the selected b-quark jet of the top-quark decay, (c) the transverse mass of the reconstructed top-quark, $M_{\mathrm{T}\ell\nu b}$ (d) the transverse W-boson mass $M_{\mathrm{T},W}$. The modeled distributions are scaled to the number of observed events.

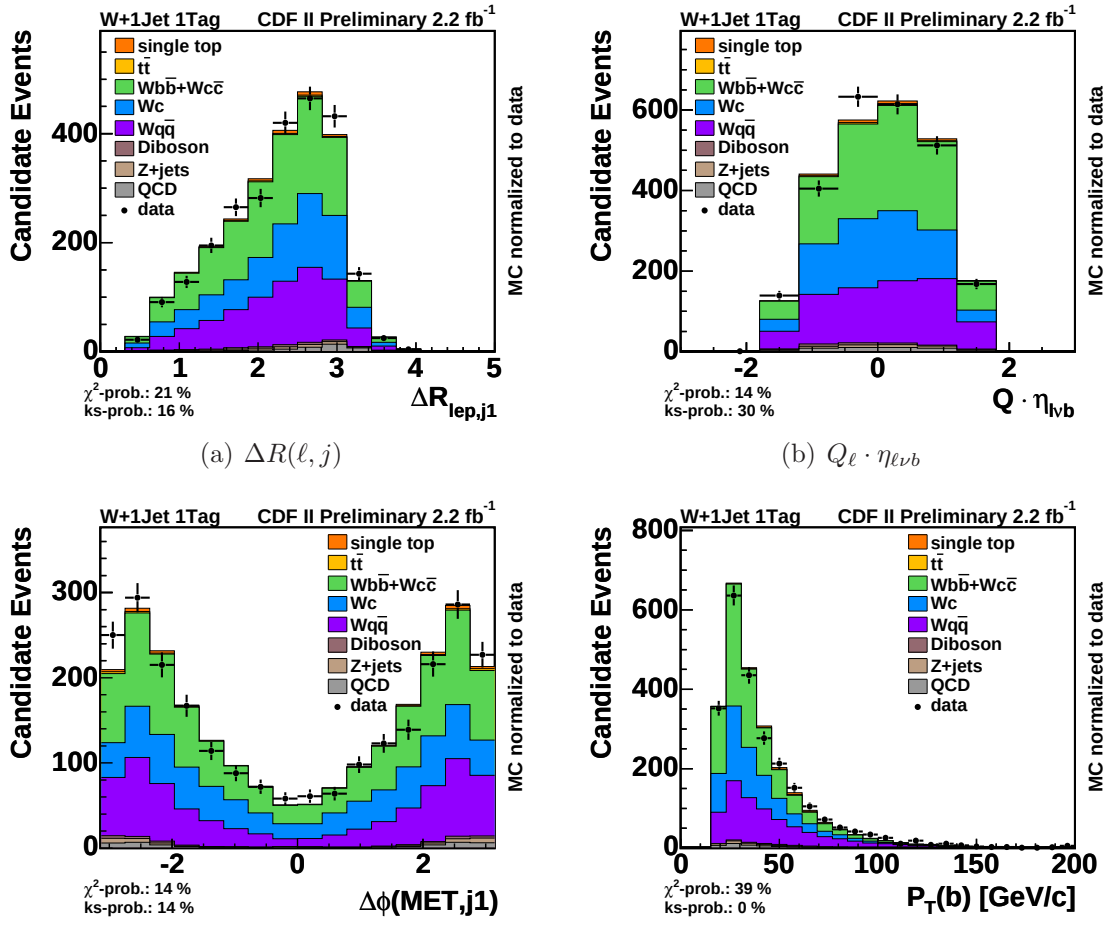

(a) $\Delta R(\ell, j)$ (b) $Q_\ell \cdot \eta_{\ell\nu b}$

(c) $\Delta\phi(j, \vec{\not{E}}_{\mathrm{T}})$ (d) $p_{\mathrm{T,b}}$

Figure 5.11: The input variables five to eight of the network. The modeled distributions are scaled to the number of observed events.

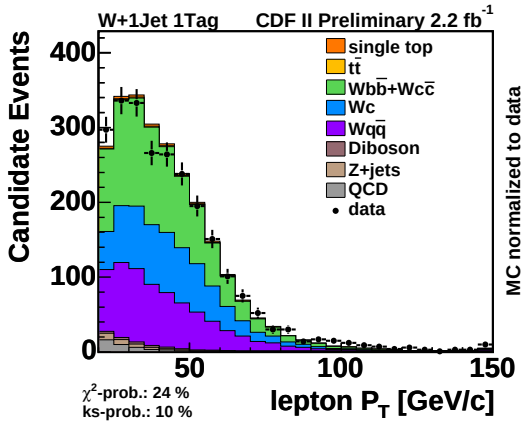

(a) $p_{\mathrm{T},\ell}$

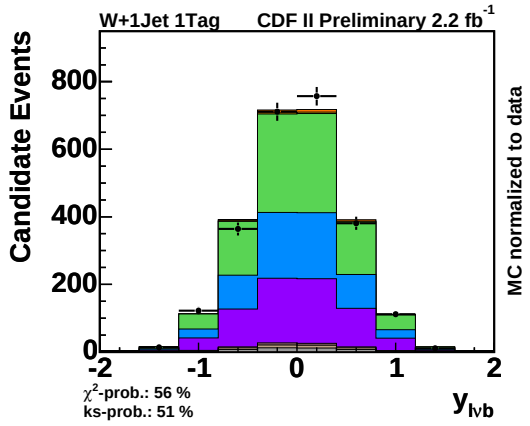

(b) $y_{\ell\nu b}$

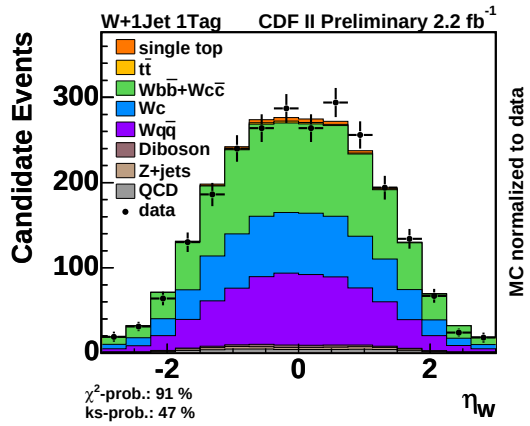

(c) η_W

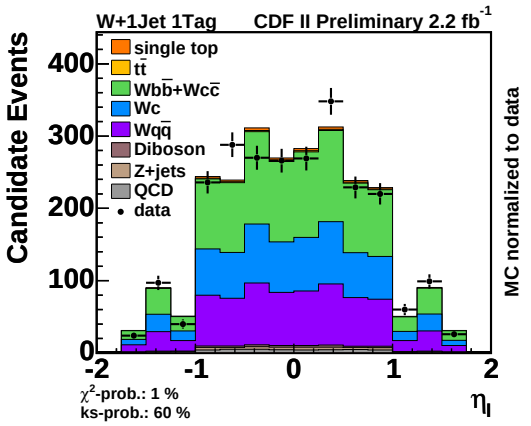

(d) η_ℓ

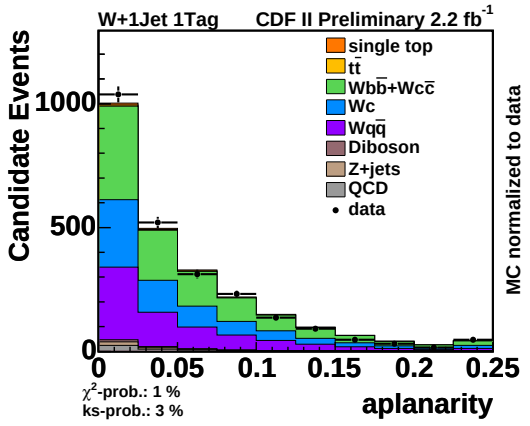

(e) aplanarity

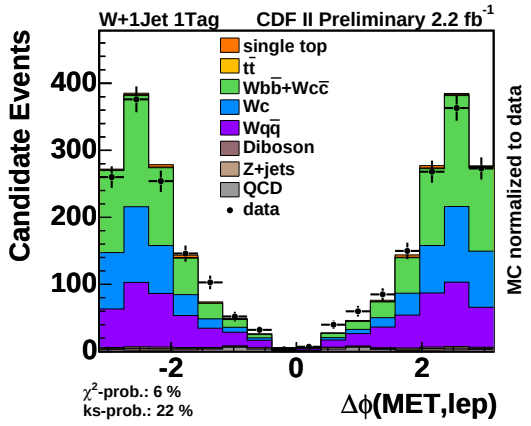

(f) $\Delta\phi(\ell, \vec{\not\!\!E}_{\mathrm{T}})$

Figure 5.12: The input variables nine to fourteen of the network. The modeled distributions are scaled to the number of observed events.

The comparisons of the distributions of the rest of the investigated input variables, those which were either not found suitable for the training or did not survived the 3σ cut, are presented in figures 5.13-5.15.

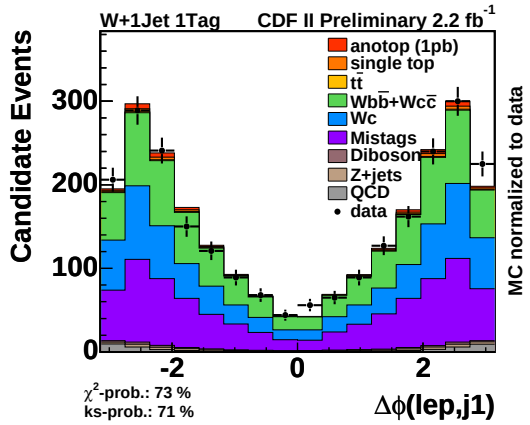

(a) $\Delta\phi(\ell, j)$

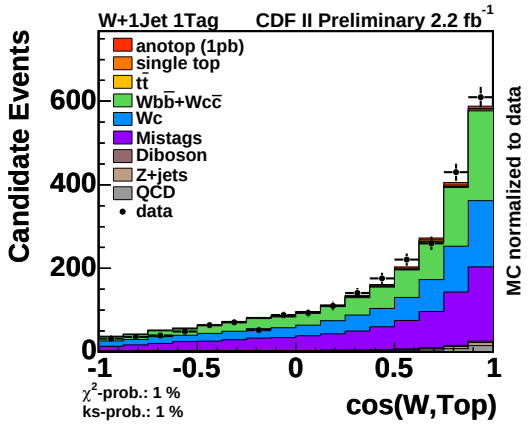

(b) $\cos\Theta(W, t)_{\text{lab}}$

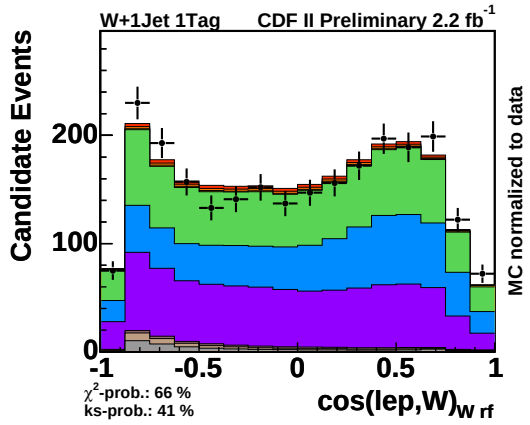

(c) $\cos\Theta(\ell, W)_{\text{W}}$

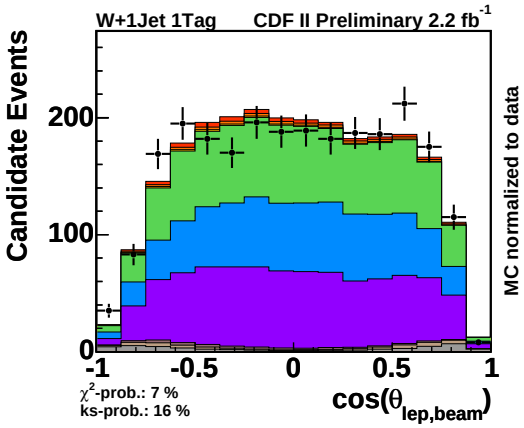

(d) $\cos\Theta(\ell, beam)_{\text{lab}}$

Figure 5.13: Input variables investigated for the training of the neural network, but were finally rejected.

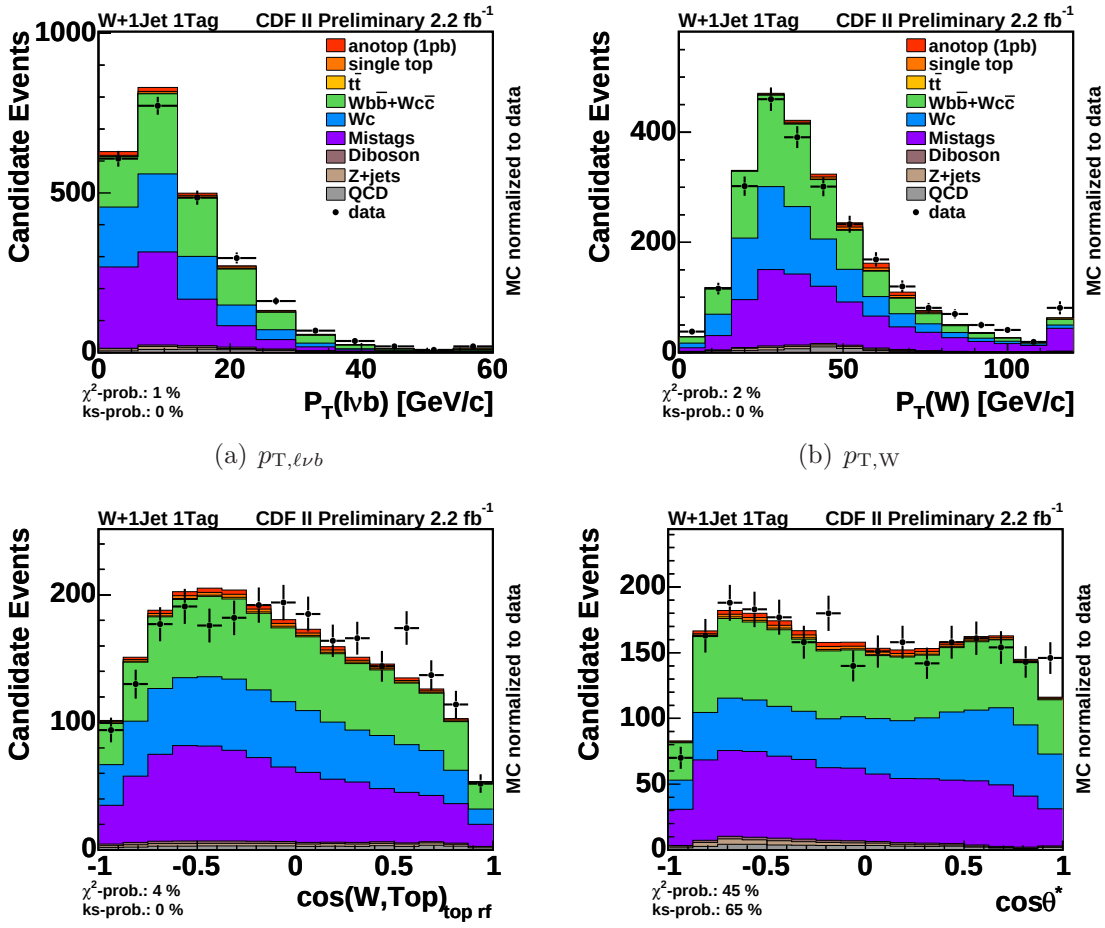

(a) $p_{\mathrm{T},\ell\nu b}$ (b) $p_{\mathrm{T,W}}$

(c) $\cos\Theta(W,t)_{\mathrm{t}}$ (d) $\cos\theta^*$

Figure 5.14: Input variables investigated for the training of the neural network, but were finally rejected.

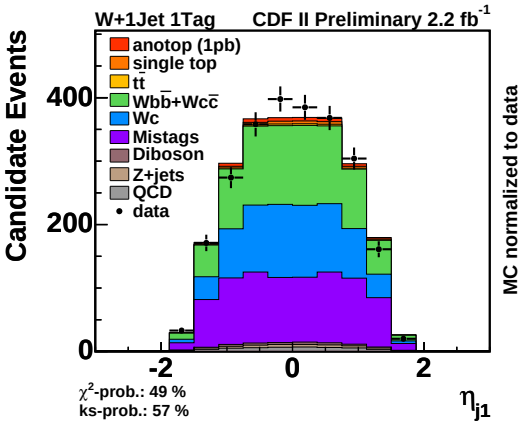

(a) η_j

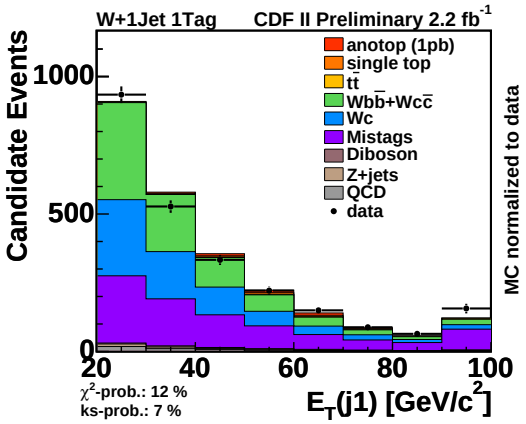

(b) $E_{\mathrm{T},jet}$

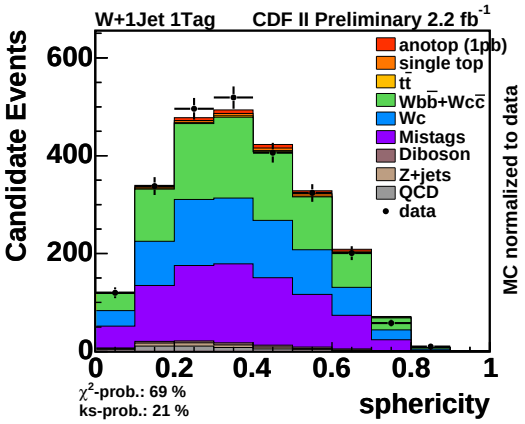

(c) sphericity

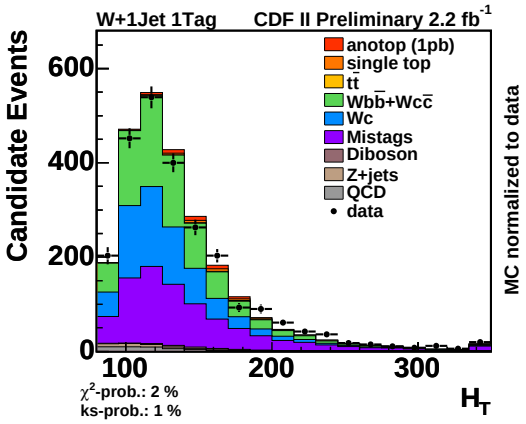

(d) H_{T}

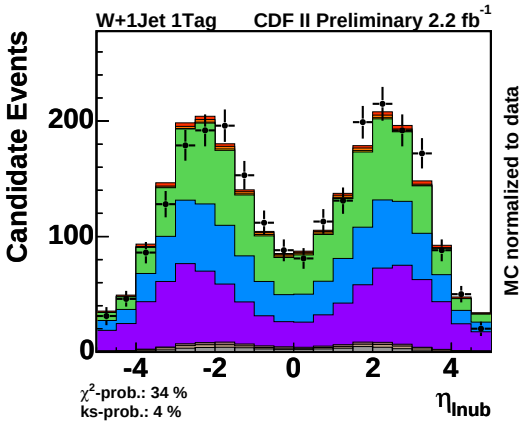

(e) $\eta_{\ell\nu b}$

Figure 5.15: Input variables investigated for the training of the neural network, but were finally rejected.

5.1.3 Output Distributions and Templates

The output of the neural network is used to create a template which is to be fitted to the output distribution of observed events (figure 5.16).

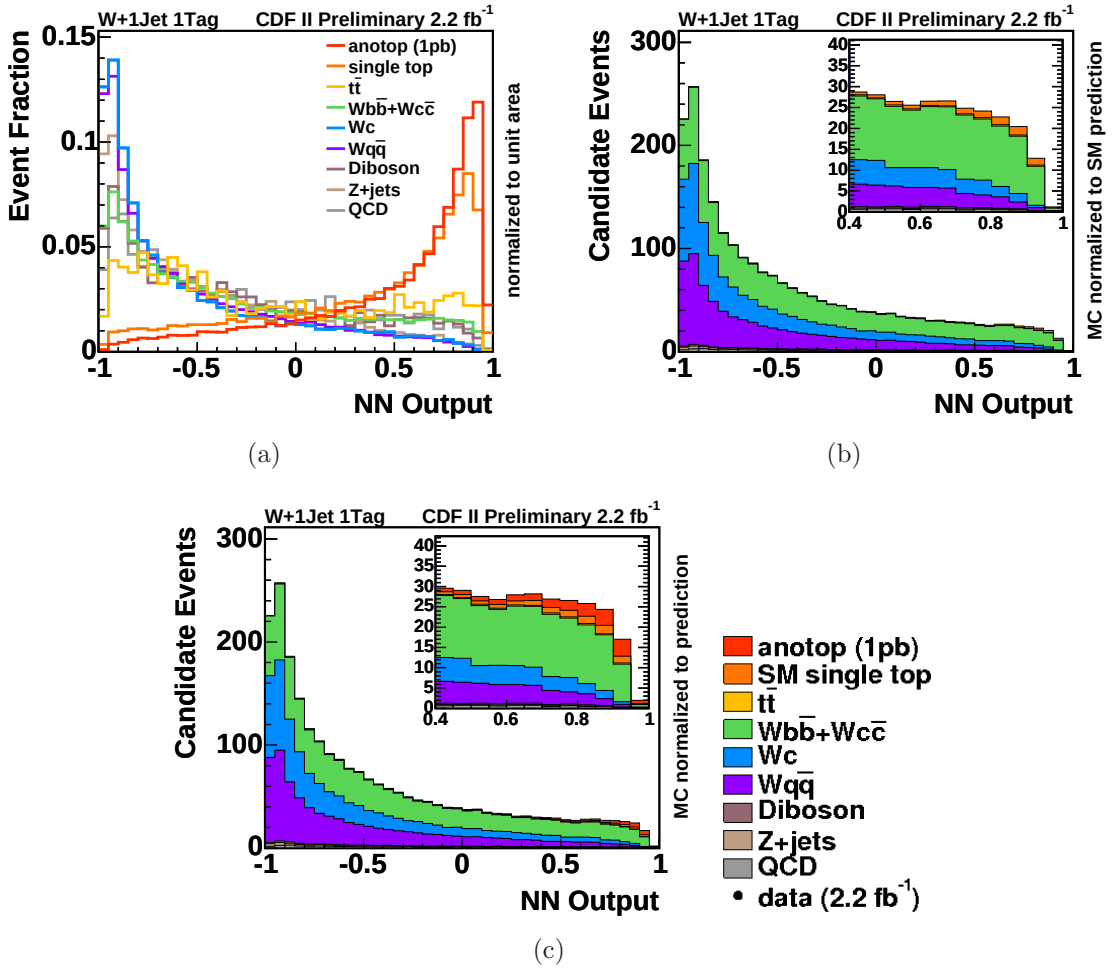

Figure 5.16: The template (a) is built by using the neural network in the W+1-jet-bin with 1 b tag. The predicted distribution is shown in (b). (c) shows how the distribution looks like if anomalous top (in red) is also considered for the given cross section of 1.0 pb, as discussed in section 4.3.

Zero-tag Network as a Cross Check

As a cross check, we trained a neural network to a sample of events passing all selection cuts except for the b-tagging requirement. The latter is called zero-tag sample. For this training, we require one taggable jet which has not been tagged.

The composition of the training sample is 50% anomalous top and 50% background, mixed according to the "Method II For You" prediction. Except for the output of the KIT flavor separator, the same variables have been used for the W+1-jet network with 1 b tag.

Process	Number of Events				
	ALL	CEM	CMUP	CMX	PHX
t-channel single-top	58.1	29.3	14.7	7.8	6.3
s-channel single-top	21.1	10.7	5.6	2.8	2
total single-top	79.2	40	20.3	10.6	8.3
$t\bar{t}$	35.9	17.8	10.4	4.8	3
$Wb\bar{b}$	2036.5	1007.7	491.6	302.7	234.6
$Wc\bar{c}$	4958.3	2482.6	1164.5	721.6	589.6
Wc	7738	3922.9	1777.8	1123.4	913.9
Mistags	$1.925 \cdot 10^5$	94032	43528	28483	25649
Non-W	2959.4	2155.9	308.7	185.2	309.6
WW	753.1	367.3	191.6	106.3	88
WZ	102.9	47.6	26.2	15.7	13.4
ZZ	4.2	1.5	1.4	0.9	0.4
total diboson	860.2	416.4	219.2	122.9	101.8
Z+jets	4063	565.4	1951.7	1413.9	131.9
total background	$2.1442 \cdot 10^5$	$1.0464 \cdot 10^5$	49472	32368	27942
AnoTop	87.2	44.6	18.6	10.5	13.5

Table 5.3: Summary of predicted numbers of background and signal events in the selected data sample in the 1-tag bin with 0 tag.).

The distributions of all input variables and the output distributions of the network (0 tag) can be found in figures 5.17-5.20. The number of expected events for all processes in the W+1 jet bin with 0 tag is shown in table 5.3.

The cross check with the pretagged samples shows that the modelling of our data is adequate. Figures 5.20 and 5.20(b) show the output of the zero-tag neural-network. Though the first bins in figure 5.20(b) are modelled well, the bins in the signal region do not share this feature to the same extent. However, the quality of the results is acceptable.

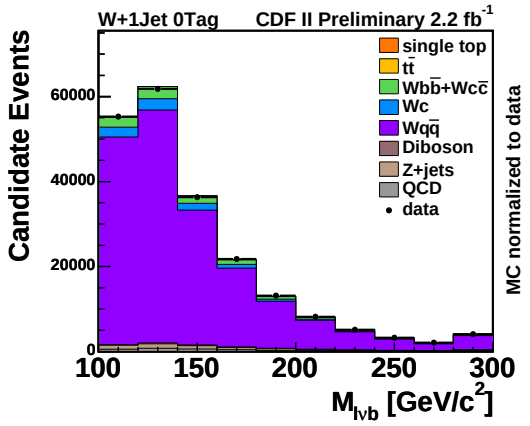

(a) $M_{\ell\nu b}$

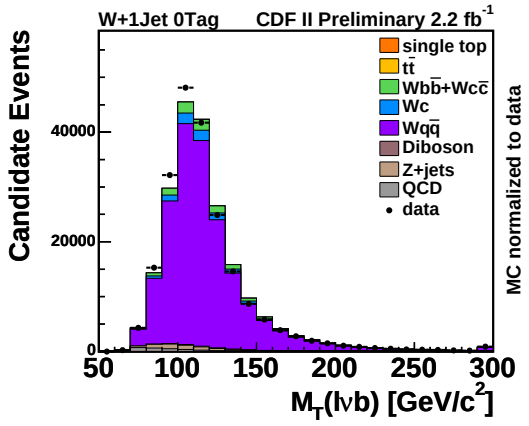

(b) $M_{\mathrm{T}\ell\nu b}$

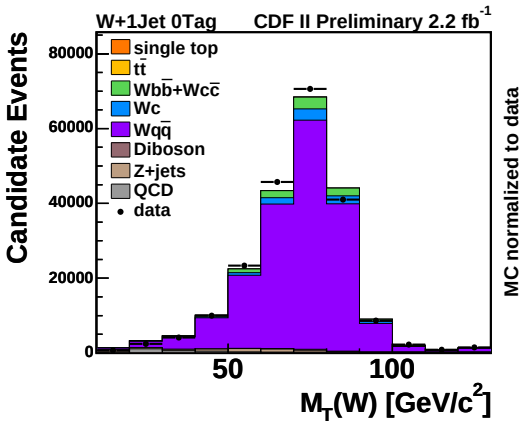

(c) $M_{\mathrm{T},W}$

Figure 5.17: Three out of the four most important input variables of the network in the W+1-jet bin with 0 tag (the KIT flavor separator output makes no sense in the W+1-jet bin with 0 tag): (a) $M_{\ell\nu b}$, output of the selected b-quark jet of the top-quark decay, (b) the transverse mass of the reconstructed top-quark, $M_{\mathrm{T}\ell\nu b}$ (c) the transverse W-boson mass $M_{\mathrm{T},W}$. The modeled distributions are scaled to the number of observed events.

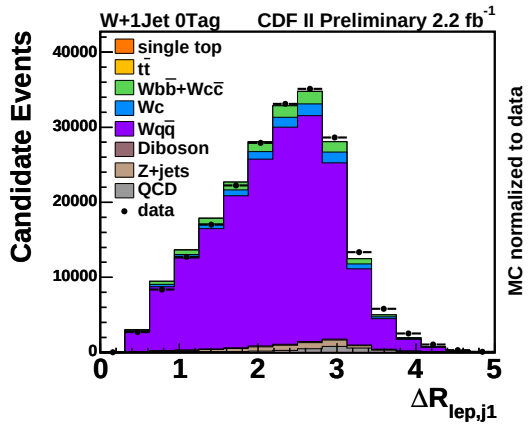

(a) $\Delta R(\ell, j)$

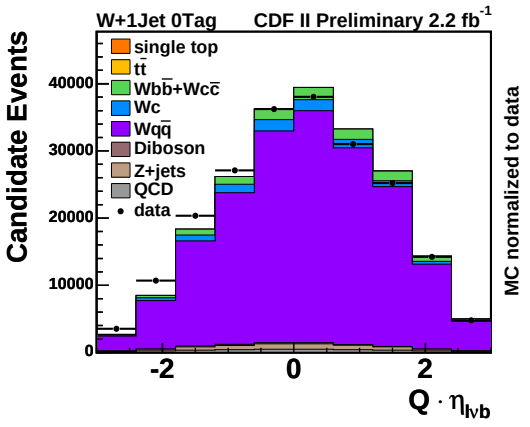

(b) $Q_\ell \cdot \eta_{\ell\nu b}$

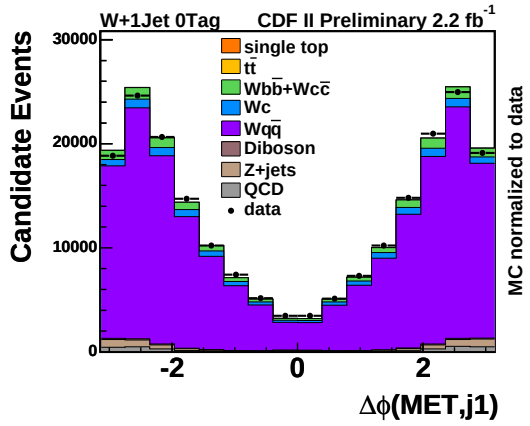

(c) $\Delta\phi(j, \vec{\not\!\!E}_{\mathrm{T}})$

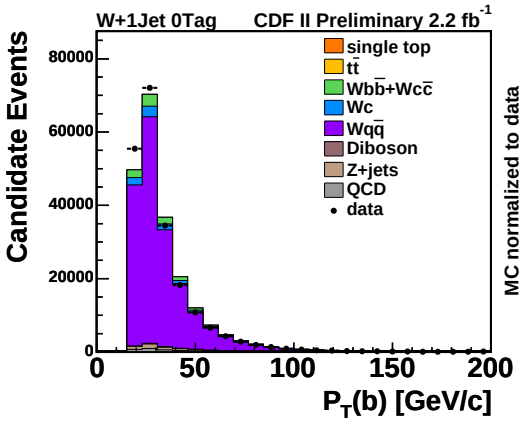

(d) $p_{\mathrm{T,b}}$

Figure 5.18: The input variables five to eight of the network in the W+1-jet bin with 0 tag. The modeled distributions are scaled to the number of observed events.

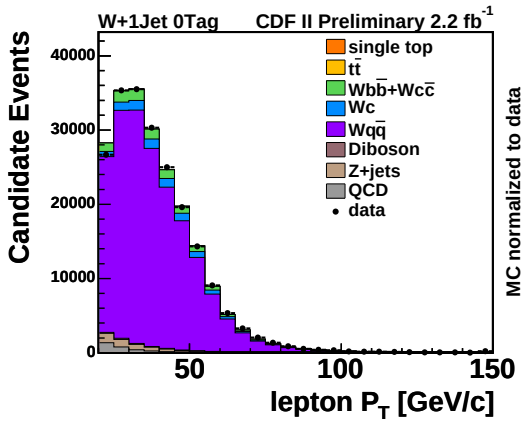

(a) $p_{\mathrm{T},\ell}$

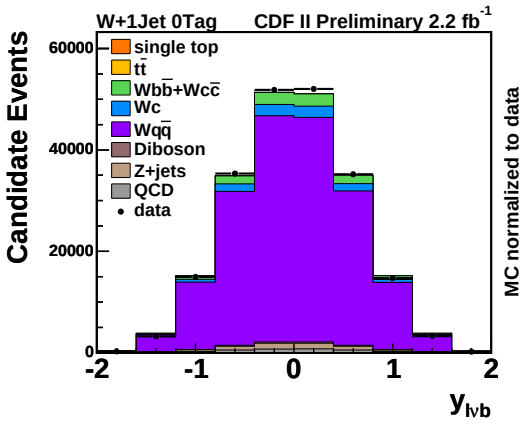

(b) $y_{\ell\nu b}$

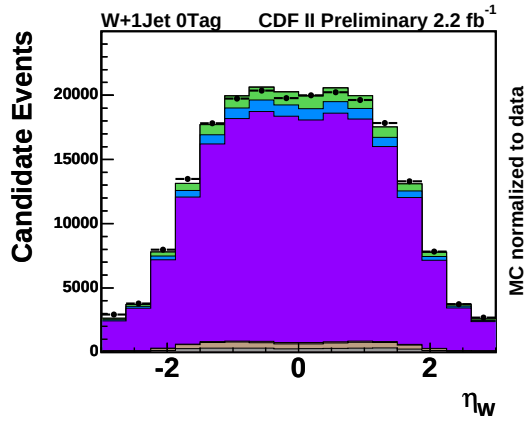

(c) η_W

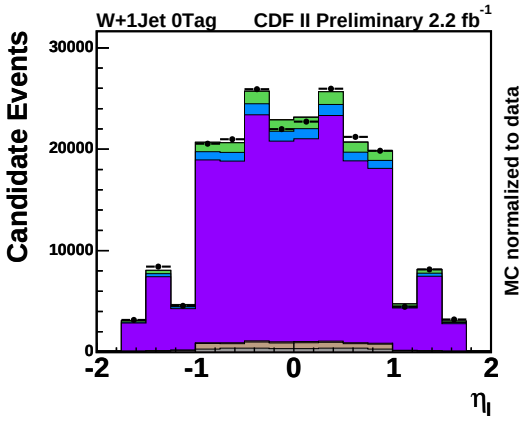

(d) η_ℓ

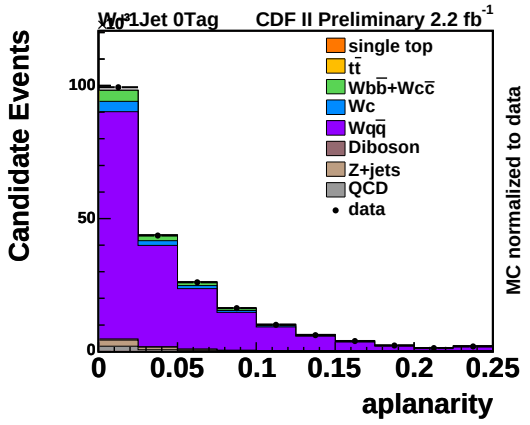

(e) aplanarity

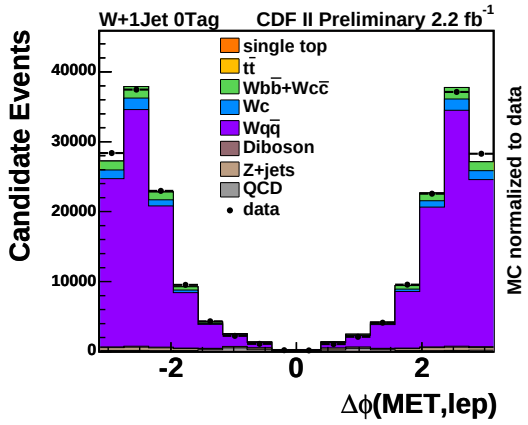

(f) $\Delta\phi(\ell, \vec{\not\!\!E}_{\mathrm{T}})$

Figure 5.19: The input variables nine to fourteen of the network in the W+1-jet bin with 0 tag. The modeled distributions are scaled to the number of observed events.

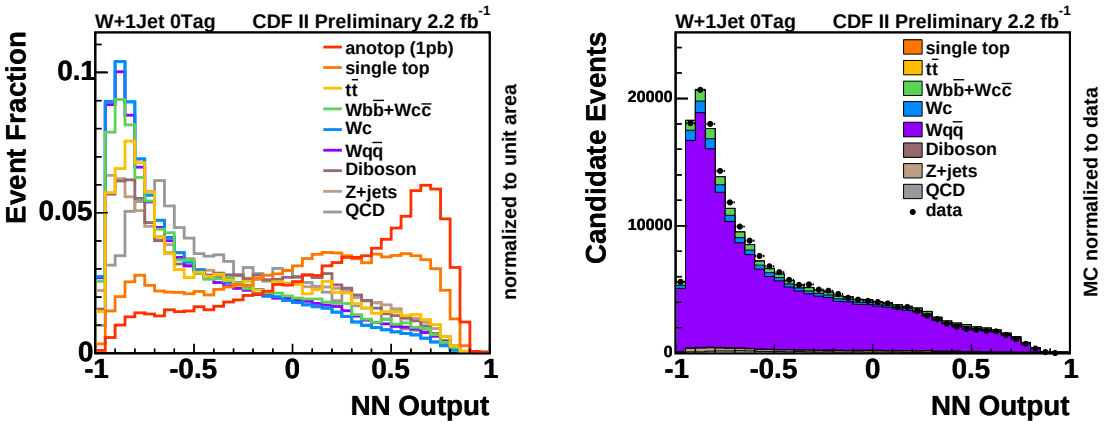

(a) (b)

Figure 5.20: The template (a) is built by using the control neural network in the W+1-jet bin with 0 tag. The predicted distribution compared with the measured one is shown in (b).

5.2 Systematic Uncertainties

Uncertainties in the modeling of physics processes and detector effects cause systematic uncertainties on the measurement results, affecting the rate of predicted signal and background events as well as the shape of the template histograms used in the fit to the observed data distribution. It must be noted that some effects induce only rate uncertainties, while some affect only the shape of the templates, even though most of them impact both.

The following sources of systematic uncertainties are considered: the uncertainty on the jet energy corrections, the uncertainty in modeling initial-state gluon radiation (ISR) and final-state gluon radiation (FSR), the choice of the parameterization of the parton distribution functions (PDF) used for the event simulation, the uncertainty in the event detection efficiency, the uncertainty in modeling the output of the KIT flavor separator, the uncertainty in the factorization and renormalization scale for the simulation of W+heavy flavor processes, the modeling of instrumental backgrounds, that is mistag events and non-W events and the uncertainty in the luminosity determination.

The impact of these sources of uncertainties is evaluated by altering the modeling of the corresponding processes or effects within their uncertainties or by assigning a plausible alternative model. As a result, relative changes of the event rates and shifted template distributions are obtained.

The effect of the uncertainty on the jet energy corrections is quantified by varying the corrections within their $\pm 1\sigma$ uncertainties [52]. The corresponding alternative

template distributions are calculated for all signal and background processes and are shown in figure 5.21 and 5.22.

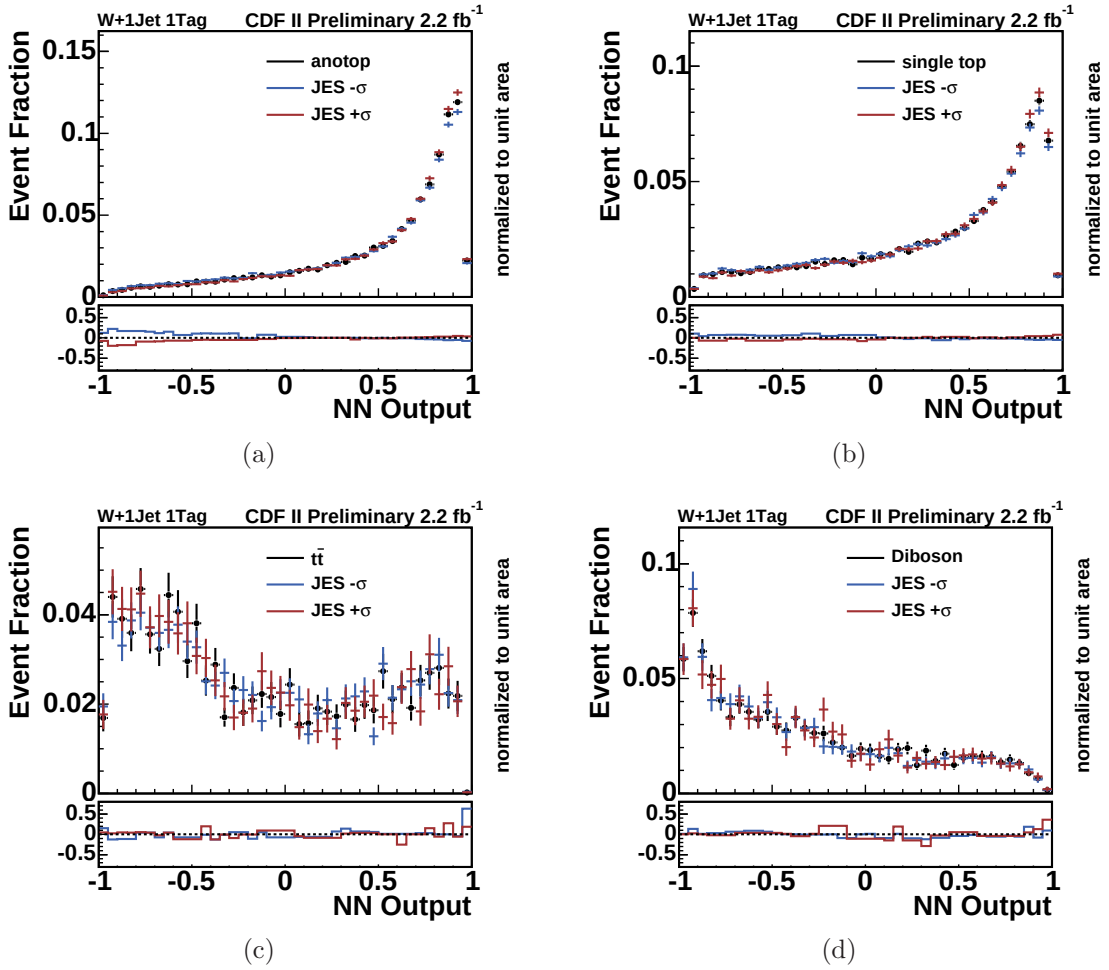

Figure 5.21: Shape systematics due to the uncertainty on the jet energy correction for anomalous top-quark (a), SM single-top (b), $t\bar{t}$ (c) and diboson (d). Each of the four plots in the figure consists of two parts. In the upper part the default distribution is shown in comparison to the shifted distributions. In the lower part the relative difference between the shifted distribution and the default is plotted, which is smoothed using a 5 bin median smoothing procedure.

The influence of initial-state and final-state gluon radiation is estimated by producing samples of simulated events for which the simulation was altered to produce either less or more gluon radiation compared to the standard setting [101]. Specifically, two parameters controlling the parton shower in the PYTHIA program are varied: Λ_{QCD} and the scale factor K to the transverse momentum scale of the showering. The different settings are derived from studies of ISR in Drell-Yan events. Using these specific ISR and FSR samples of simulated events, alternative template shapes are produced for anomalous top-quark, single-top-quark and $t\bar{t}$ events as illustrated in figures 5.23 and 5.24.

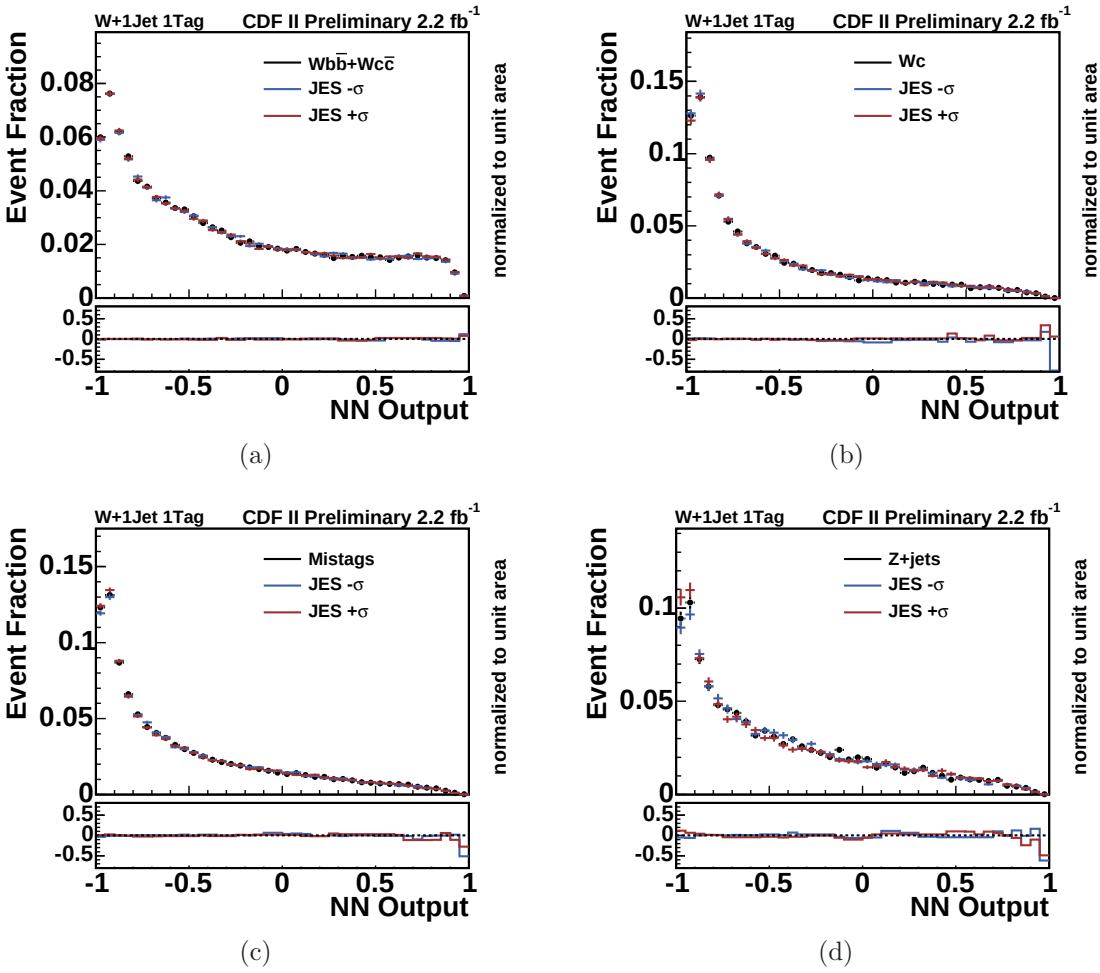

Figure 5.22: Shape systematics due to the uncertainty on the jet energy correction for $Wb\bar{b} + Wc\bar{c}$ (a), Wc (b), mistags (c) and Z+jets (d). Each of the four plots in the figure consists of two parts. In the upper part the default distribution is shown in comparison to the shifted distributions. In the lower part the relative difference between the shifted distribution and the default is plotted, which is smoothed using a 5 bin median smoothing procedure.

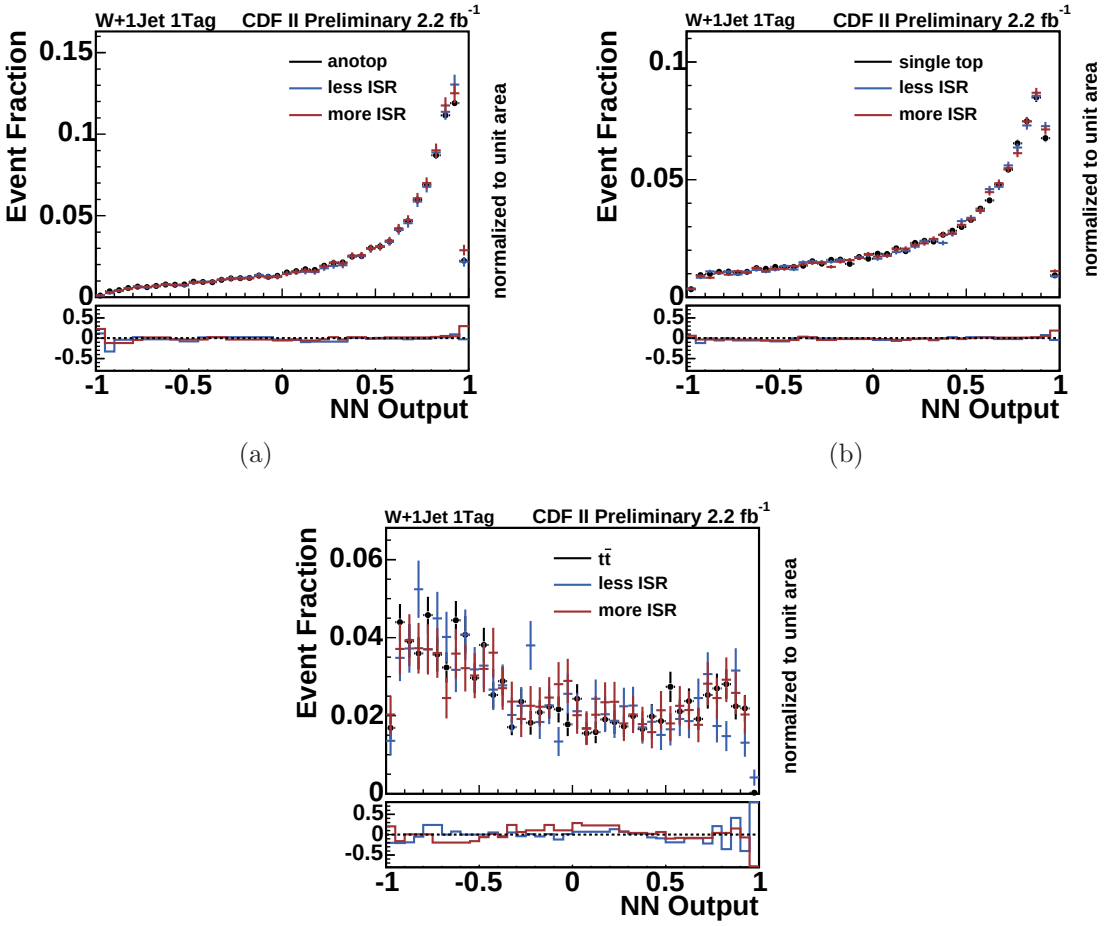

Figure 5.23: Shape systematics due to the uncertainty in ISR for anomalous top-quark (a), single-top (b) and $t\bar{t}$ (c). Each of the three plots in the figure consists of two parts. In the upper part the default distribution is shown in comparison to the shifted distributions. In the lower part the relative difference between the shifted distribution and the default is plotted.

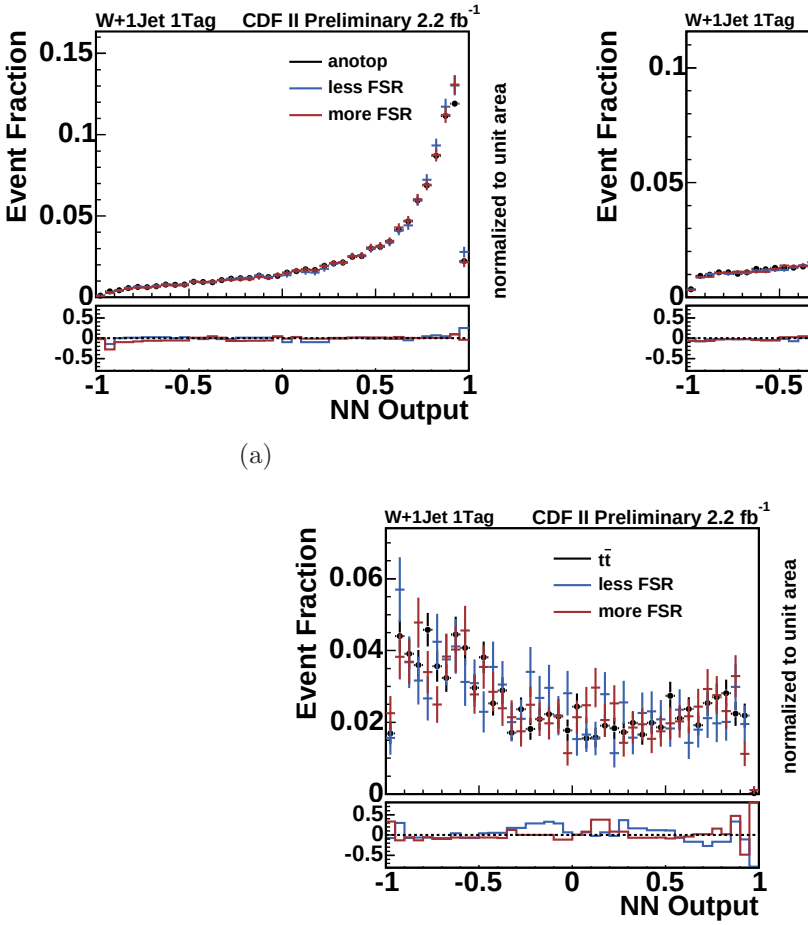

Figure 5.24: Shape systematics due to the uncertainty in the FSR for anomalous top-quark (a), single-top (b) and $t\bar{t}$ (c). Each of the three plots in the figure consists of two parts. In the upper part the default distribution is shown in comparison to the shifted distributions. In the lower part the relative difference between the shifted distribution and the default is plotted.

The impact of the uncertainties on the PDF parameterization are studied by reweighting anomalous top-quark, single-top-quark and $t\bar{t}$ events with weights associated with the 20 pairs of CTEQ6M eigenvectors. The rate uncertainty of the combined single top-quark processes, which is based on the MADEVENT event generator, is determined by a comparison to differential cross sections computed with the ZTOP program. The factorization and renormalization scale is varied in the simulation to derive an additional set of altered template histograms for W+heavy flavor events. The default W+jets Monte Carlo samples are generated with a dynamic scale $\mu^2 = Q^2$. As a variation, the scale is either doubled, $\mu^2 = 2Q^2$, or halved, $\mu^2 = \frac{Q^2}{2}$. The influence of the variation of Q^2 on the shape of the output distribution of $Wb\bar{b}$ events is illustrated in figure 5.25. It is one of the larger systematic uncertainties exhibiting a clear trend for both variations in the same direction.

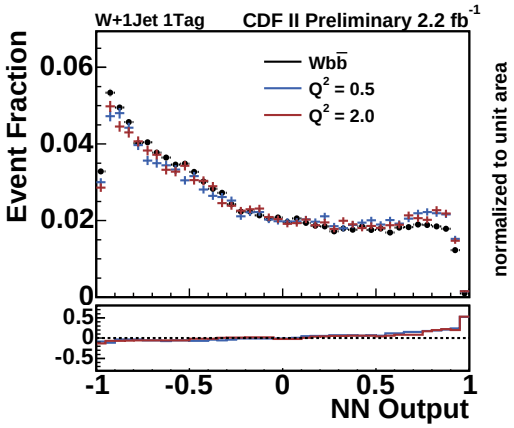

Figure 5.25: Shape systematics due to the uncertainty in the ALPGEN factorization/renormalization scale Q^2 for the $Wb\bar{b}$ background. The plot consists of two parts. The upper part shows the default distribution in comparison to the shifted distribution. The lower part shows the relative difference between the shifted distribution and the default one.

The uncertainty in the event detection efficiency ϵ_{evt} includes the uncertainties on the trigger efficiency, on the lepton identification efficiency, and on the b-tagging efficiency which is the dominating factor.
Since no cut is applied on the output of the KIT flavor separator, the uncertainty associated with this quantity does not imply a rate uncertainty, but only a shape uncertainty on the template distributions. Systematic effects are studied by utilizing the correction function derived for the mistags. Therefore we consider two scenarios. A pessimistic one, in which we apply the correction function on the c-like templates, such that they get more signal like. And the optimistic one, in which we use the uncorrected mistag shape, such that the mistag template gets more background like. The influence of these scenarios on $Wb\bar{b} + Wc\bar{c}$, Wc and the mistags' templates is illustrated in figure 5.26.

A modified model of QCD events is considered to investigate the influence of this aspect on the analysis. The flavor composition of the QCD sample is varied: the default model assumes a composition of 45% b-quark jets, 40% c-quark jets, and 15% light-quark jets, whereas the alternative model uses a composition of 60:30:10 [97], respectively. The influence of the flavor composition on the non-W template is illustrated in figure 5.27(a).

To evaluate the systematic effect on the shapes of the distributions caused by the modeling of mistagged light-quark jet events, an alternative model is utilized to create template distributions. This is realized by replacing the default mistag model based on simulated events as described in section 4.4 by a description on the basis of measured W+jets events before b tagging. The influence of the mistag model is illustrated in figure 5.27(b).

The analysis is done under the assumption of a top-quark mass of $m_{\text{top}} = 175\,\text{GeV}/c^2$.

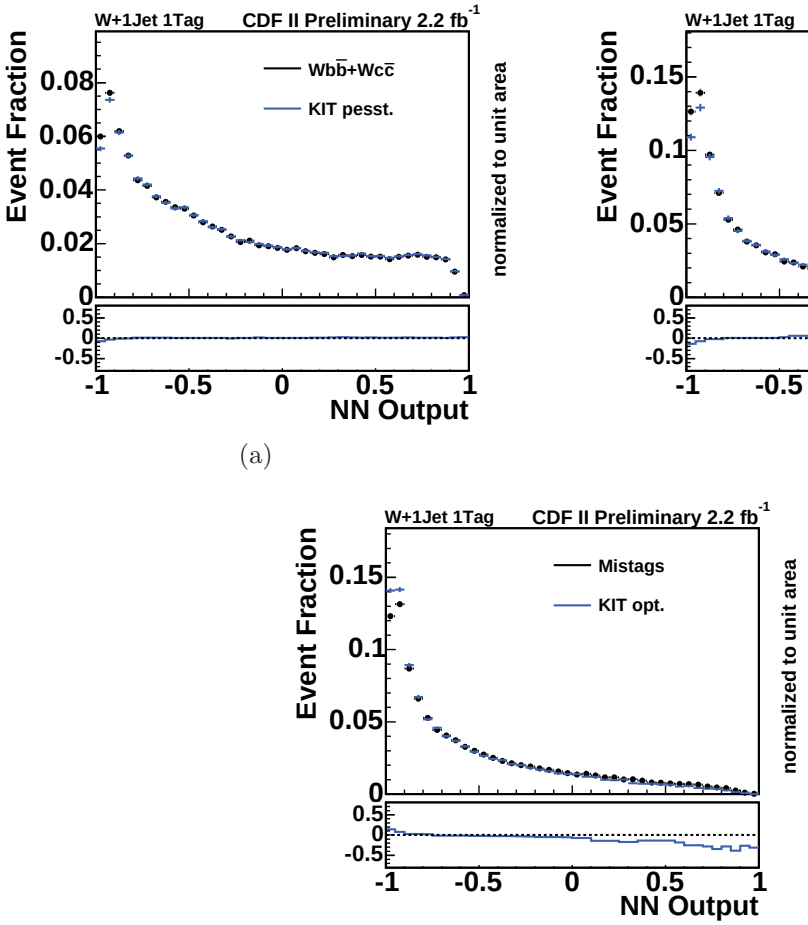

Figure 5.26: Shape systematics due to the influence of the mistags correction function of the KIT flavor separator on $Wb\bar{b} + Wc\bar{c}$ (a), Wc (b) and the mistags (c). Each of the three plots in the figure consists of two parts. The upper part shows the default distribution in comparison to the shifted distribution. The lower part shows the relative difference between the shifted distribution and the default one.

all uncertainties in %					
Source	anoTop	single-top	$t\bar{t}$	diboson	Z+jets
IFSR less/more	2.9/-2.9	2.1/1.3	-7.2/-7.9		
PDF	3.4/-3.7	2.8/-3.0	1.9/-2.3		
ϵ_{evt}	13.7/-13.7	5.7/-5.7	2.4/-2.4	7.8/-7.8	10.2/-10.2
Luminosity	6.0/-6.0	6.0/-6.0	6.0/-6.0	6.0/-6.0	6.0/-6.0
Cross section	0.0	12.6/-12.6	12.4/-12.4	1.9/-1.9	10.8/-10.8
M_{top} 172/178	5.3/-4.8	6.1/-5.5	9.7/-8.9		

Table 5.4: Systematic rate uncertainties.

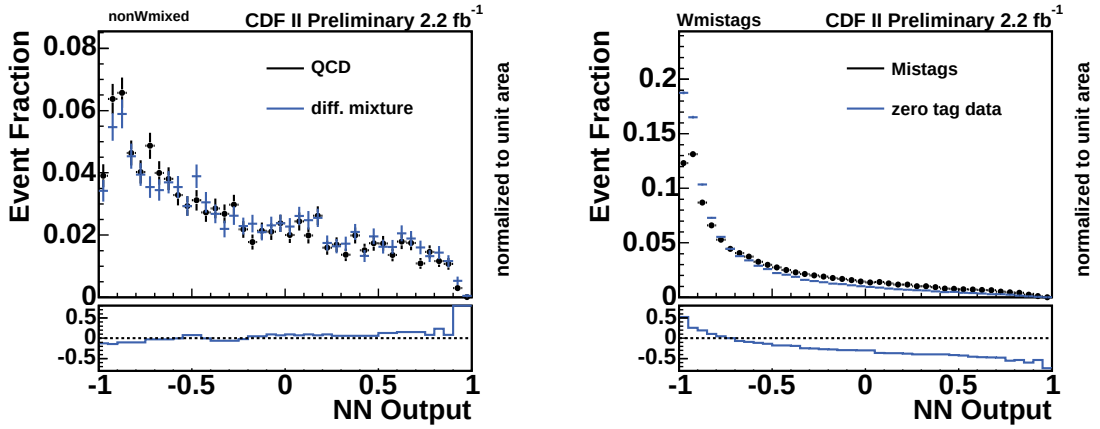

(a) (b)

Figure 5.27: (a): Shape systematics due to the influence of the non-W flavor composition. (b): Shape systematics due to the influence of the mistag model. Each of the two plots in the figure consists of two parts. The upper part shows the default distribution in comparison to the shifted distribution. The lower part shows the relative difference between the shifted distribution and the default one.

process	source: JES
ano-top	-6.7/-2.2 %
single-top	-9.6/+10.0 %
$t\bar{t}$	-15.6/+18.8 %
$Wb\bar{b}$	-9.3/+8.7 %
$Wc\bar{c} + Wc$	-6.3/+7.4 %
Z+jets	-0.1/+0.1 %
Diboson	-11.5/+13.5 %
Mistags	-0.1/+0.1 %

Table 5.5: Systematic JES down/up rate uncertainties.

That is why the uncertainty in the top-quark mass is not taken into account as a systematic uncertainty. Hence, the analyses provide rather an upper limit on the production cross-section of anomalous top quark at the specified value of the top-quark mass. However, if the top-quark mass is varied in the simulation by $\pm 3, \mathrm{GeV}/c^2$, the acceptance for anomalous top-quark events changes as shown in table 5.4. Table 5.5 shows explicitly the rate uncertainties caused by the biggest source of systematic errors, the jet energy scale (JES).

5.3 Statistical Procedure

In this section, the likelihood function used for the template fit is introduced. Moreover, the expected upper limit on the anomalous production cross-section is presented. The latter is a measure for the a-priori sensitivity of the analysis.

5.3.1 Likelihood Function

For this analysis we use a likelihood function for the template fit to the observed events. This likelihood function consists of Poisson terms for the individual bins of the fitted histogram:

$$L(\beta_1, ..., \beta_C; \delta_1, ..., \delta_S) = \prod_{k=1}^{B} \frac{e^{-\mu_k} \cdot \mu_k^{n_k}}{n_k!} \tag{5.5}$$

where B is the number of bins, k is the bin index, μ_k is the mean value of the predicted number of events in bin k, and n_k is the number of observed events in bin k.

$$\mu_k = \sum_{j=1}^{C} \mu_{jk} = \sum_{j=1}^{C} \beta_j \cdot \hat{\nu}_j \cdot \alpha_{jk} \ . \tag{5.6}$$

The index j runs over the different physical processes. The total number of considered physical processes is C. The predicted expectation values for the number of events of a certain event category are denoted $\hat{\nu_j}$. The free parameters in the fit are given by $\beta_j = \nu_j/\hat{\nu_j}$, i.e. the expectation values over their prediction. The normalized content of bin k of the template histogram for event category j is α_{jk}. Hence, the α_{jk} fulfill the normalization condition $\sum_{k=1}^{B} \alpha_{jk} = 1$. The expectation value of the physical process j in the bin k is denoted μ_{jk} and systematic uncertainties are included as factors modifying μ_{jk}, with

$$\begin{aligned} \mu_{jk} \quad = \quad & \beta_j \cdot \hat{\nu}_j \cdot \left\{ \prod_{i=1}^{S} \left(1 + |\delta_i| \cdot (\epsilon_{ji+} H(\delta_i) + \epsilon_{ji-} H(-\delta_i)\right) \right\} \cdot \\ & \alpha_{jk} \cdot \left\{ 1 + \sum_{i=1}^{S} \left(|\delta_i| \cdot \kappa_{jik}^{+} H(\delta_i) + \kappa_{jik}^{-} H(-\delta_i) \right) \right\} \ . \end{aligned} \tag{5.7}$$

In the fit, several effects causing systematic rate uncertainties are considered as given by table 5.4. In this notation, the sources of systematic uncertainties carry the index i. The variation in strength of a systematic effect i is measured with the variable δ_i which constitutes an additional fit parameter and measures the strength of the systematic effect in units of one standard deviation. The relative rate uncertainties due to these sources are named ϵ_{ji+} and ϵ_{ji-}. As outlined in section 5.2, several sources of uncertainties influencing the template shape are taken into account. In the template distributions, the shape uncertainties are reflected by relative uncertainties in the bin content of bin k, being denoted as κ_{jik}^{+} and κ_{jik}^{-}. The values of κ_{jik} are

calculated from the systematically shifted normalized template histograms α^{+}_{jik} and α^{-}_{jik} according to

$$\kappa^{\pm}_{jik} = \frac{\alpha^{\pm}_{jik} - \alpha_{jk}}{\alpha_{jk}} \; . \tag{5.8}$$

By construction the $\kappa^{\pm}_{jik}$ satisfy the normalization condition

$$\sum_{k=1}^{B} \alpha_{jk} \cdot \kappa^{\pm}_{jik} = 0 \; . \tag{5.9}$$

The template histogram taking into account the shifts caused by all systematic effects with strengths $\{\delta_i\}$ is given by

$$\alpha'_{jk} = \alpha_{jk} \cdot \left\{ 1 + \sum_{i=1}^{S} \delta_i \cdot \kappa_{jik} \right\} . \tag{5.10}$$

Due to (5.9), the shifted histogram α'_{jk} is properly normalized:

$$\sum_{k=1}^{B} \alpha'_{jk} = 1 \, . \tag{5.11}$$

The anomalous top-quark content is measured by computing the reduced likelihood function $\mathcal{L}_{\mathrm{red}}(\beta_1)$ which only depends on one variable, the normalized rate of anomalous single top-quark events, β_1. We obtain $\mathcal{L}_{\mathrm{red}}(\beta_1)$ from the full likelihood function $L(\beta_1, \ldots, \beta_C; \delta_1, \ldots, \delta_S)$ by integrating out the normalized background rates β_j, where j runs over the background event categories, and the parameters δ_i describing the strengths of systematic excursions. Theses parameters are also called *nuisance parameters*. The integration is performed using a Monte Carlo technique. Gaussian integration kernels are applied

$$G(\beta_j, 1.0, \Delta_j) = \frac{1}{\sqrt{2\,\pi\,\Delta_j^2}} \cdot \exp\left(\frac{-(\beta_j - 1.0)^2}{2\,\Delta_j^2} \right) \; , \text{ and} \tag{5.12}$$

$$G(\delta_i, 0.0, 1.0) = \frac{1}{\sqrt{2\,\pi}} \cdot \exp\left(\frac{-\delta_i^2}{2} \right) \; . \tag{5.13}$$

The relative uncertainties of the prediction Δ_j are given in table 5.6. We convert the reduced likelihood $\mathcal{L}_{\mathrm{red}}(\beta_1)$ into a probability density $p(\beta_1)$ by applying a prior $\pi(\beta_1)$, which is zero for $\beta_1 < 0$ and 1 elsewhere.

5.3.2 Expected Upper Limit

To compute the upper limit on the anomalous production cross section, ensemble tests are used. In this context, an ensemble test consists of a set of pseudo experiments. For each pseudo experiment, first the number of events N_j of each event

process	Δ
single-top	15.0 %
$t\bar{t}$	14.0 %
$Wb\bar{b}$+$Wc\bar{c}$	200.0 %
Wc	30.0 %
Mistags	16.6 %
Z+jets	10.8 %
Diboson	10.0 %
QCD	40.0 %

Table 5.6: Gaussian constraints.

category is determined by drawing a random number from a Poisson distribution of a mean $\hat{\nu}_j$. As a result, the pseudo experiment features a total number of $\sum N_j$ events. Systematic uncertainties on the expected background rates are considered by fluctuating the Poisson means $\hat{\nu}_j$ within their uncertainties Δ_j. In a second step, N_j random numbers are drawn from the template distributions of the neural network output for all considered event categories displayed in figure 5.16. Those random numbers are filled in a histogram which constitutes the neural network output distribution of a particular pseudo experiment.

To obtain a measure for our a-priori sensitivity we perform Monte Carlo experiments without anomalous top-quark events. For each experiment we calculate the upper limit at 95% C.L. (confidence level). We define the median of all upper limits as our sensitivity. We obtain: $\sigma^{95}_{\text{apriori}} = 1.4$ pb. The 16% quantile is 0.9 pb, while the 84% quantile is 2.3 pb. The distribution of upper limits is shown in figure 5.28.

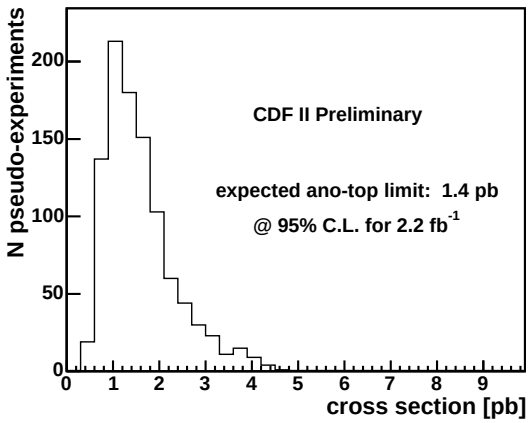

Figure 5.28: A-priori sensitivity: the median of the upper limit is 1.4 pb, the 16% quantile: is 0.9 pb, the 84% quantile is 2.3 pb.

Chapter 6

Results

In this chapter, the results of this search are presented. Section 6.1 refers to the upper limit on the anomalous cross section, which is obtained directly from the experiment. In sections 6.2 and 6.3 is shown how the experimental result can be applied to recent theoretical predictions and be converted to upper limits on the anomalous coupling constants and branching ratios.

6.1 Upper Limit on The Anomalous Cross Section

After the expected sensitivity has been determined, the neural network is applied to observed events. At first, the output distributions of observed events are compared to the expected distributions as shown on figure 6.1(b). Finally, the templates are fitted to the observed distributions to determine an upper limit on the anomalous top-quark cross section (figure 6.2).

The maximum of the probability density gives the most probable value for the cross section. To obtain the upper limit, we integrate the probability density from 0 to a value $\sigma^{95}_{\text{anoTop}}$ for which the integral is 0.95. We call $\sigma^{95}_{\text{anoTop}}$ the upper limit on the cross section of the anomalous top-quark production at the 95% C.L. We find an upper limit of 1.8 pb at the 95% C.L.. Figure 6.1(c) illustrates how the distributions would look like in the hypothesis of an existing anomalous top-channel with the cross section of 1.8 pb.

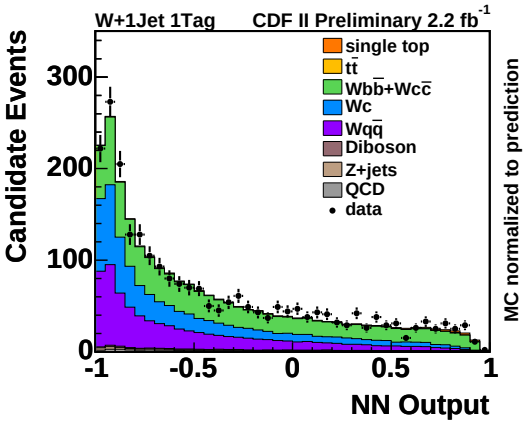

(a)

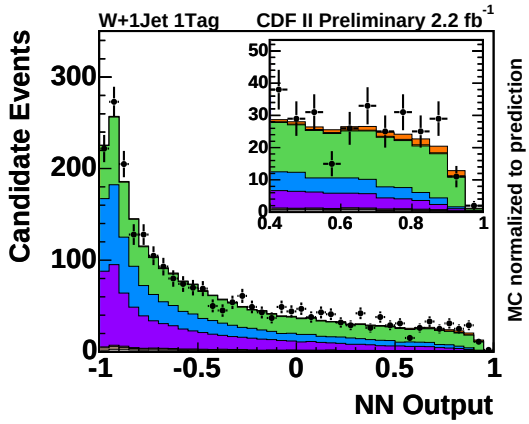

(b)

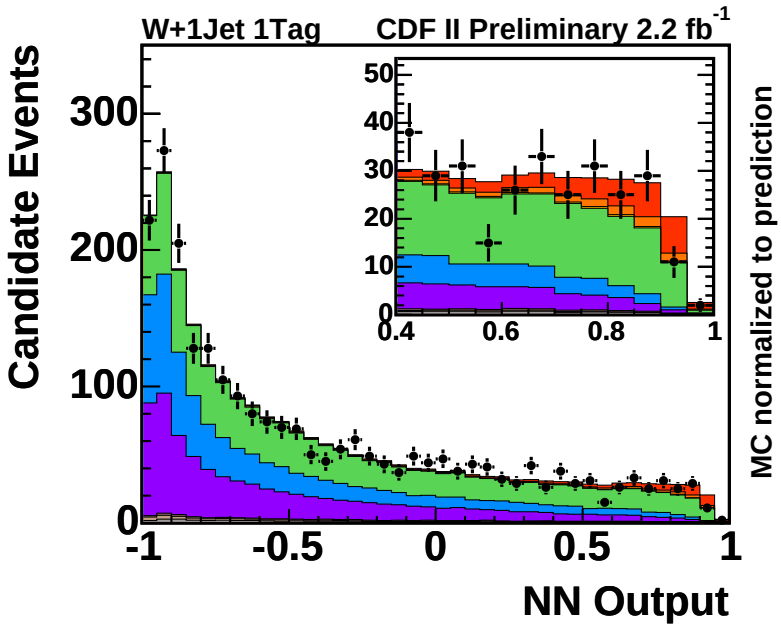

(c)

Figure 6.1: The predicted and measured distributions of the neutral-network output. (a) and (b) show the case that the predicted distribution consists only of SM background. (c): On top of the SM background, an anomalous top-quark signal has been added (red color on top), corresponding to a cross section of 1.8 pb, which is the upper limit on the cross section observed in data.

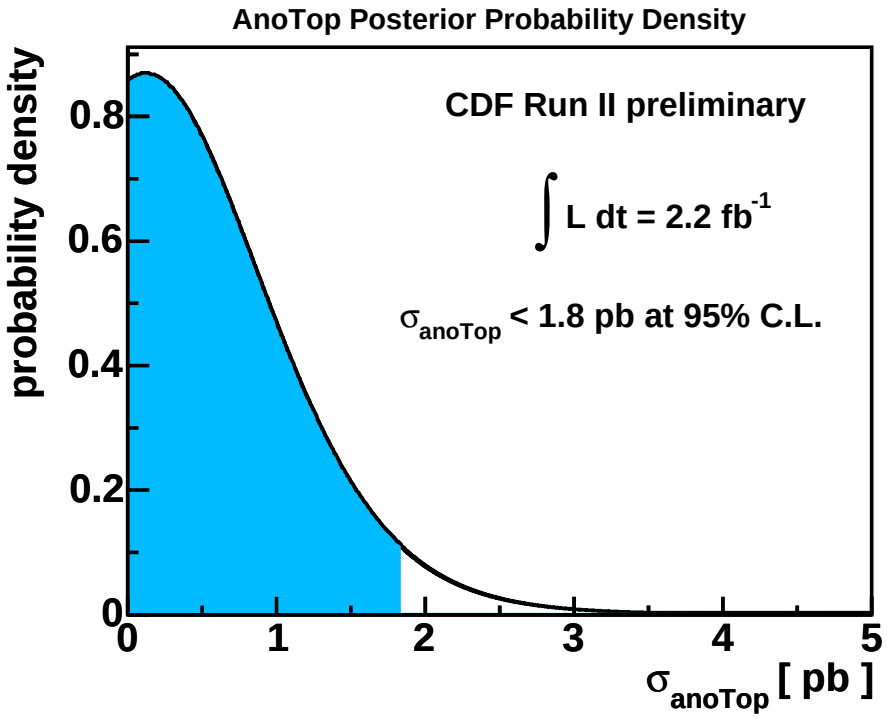

Figure 6.2: The posterior probability density. The region beyond the blue part of the distribution, which is referring to cross sections of anomalous top-quark production larger than 1.8 pb, is excluded at 95% C.L..

6.2 Upper Limit on The Anomalous Coupling Constants

Using theoretical predictions of $\sigma(u(c)+g \rightarrow t)$ which include threshold resummation effects [34, 102], we convert the upper limit on the cross section to upper limits on the FCNC coupling constants (Fig. 6.3) at the 95% C.L. and find $\kappa_{gtu}/\Lambda < 0.018$ TeV^{-1}, assuming $\kappa_{gtc} = 0$ and $\kappa_{gtc}/\Lambda < 0.069$ TeV^{-1}, assuming $\kappa_{gtu} = 0$.
Table 6.1 shows the LO, NLO and resummed cross sections for direct top-quark production at the Tevatron Run II in values of κ/Λ. These values were used to plot $\sigma_{ano} \propto {\kappa_{gtu}}^2$ and $\sigma_{ano} \propto {\kappa_{gtc}}^2$ in section 1.2.3.

For $\kappa_{gtu}/\Lambda = \kappa_{gtc}/\Lambda = \kappa/\Lambda$ one gets the limit on both anomalous subprocesses, based on the latters' contributions to the experimentally deduced limit on the overall anomalous top-quark production cross-section, by using

$$\sigma_{exp} = \frac{A}{(0.01)^2} \cdot {\kappa_{gtu}}^2 + \frac{B}{(0.01)^2} \cdot {\kappa_{gtc}}^2, \tag{6.1}$$

process	Tevatron Run II $\left(\frac{\kappa/\Lambda}{0.01\ \mathrm{TeV}^{-1}}\right)^2$ fb			LHC $\left(\frac{\kappa/\Lambda}{0.01\ \mathrm{TeV}^{-1}}\right)^2$ pb		
	LO	NLO	Resum	LO	NLO	Resum
$u + g \to t$	268	425	547	12.9	17.0	23.7
$c + g \to t$	13.1	28.1	38.2	1.71	2.53	3.71

Table 6.1: The LO, NLO and resummed cross sections for direct top-quark production at the Tevatron Run II as found in reference [34] for the case of using CTEQ PDFs. As a comparison, the corresponding expected values at the LHC are shown.

where $\sigma_{exp} = 1.8$ pb is the observed limit on the anomalous cross section, while A and B stand for the contributions of the subprocesses $u+g \to t$ and $c+g \to t$ to the overall cross section, respectively. In our case, $A = 0.547$ pb and $B = 0.0382$ pb, as shown in table 6.1. In this way, we get $\kappa_{gtu}/\Lambda = \kappa_{gtc}/\Lambda = \kappa/\Lambda = 0.017\ \mathrm{TeV}^{-1}$. One may then sum up the results for the limits on the anomalous coupling constants as done in table 6.2.

$\kappa/\Lambda\ [\ \mathrm{TeV}^{-1}]$	$\kappa_{gtu}/\Lambda\ [\ \mathrm{TeV}^{-1}]$	$\kappa_{gtc}/\Lambda\ [\ \mathrm{TeV}^{-1}]$
0.018	0.018	0
0.069	0	0.069
0.017	0.017	0.017

Table 6.2: Summary of the limits on the coupling constants.

6.3 Upper Limit on Branching Ratios (BR) in NLO Calculation

In order to convert the limit on the cross section in limits on the NLO branching ratios, $BR(t \to ug)$ and $BR(t \to cg)$, the theoretical calculations in next-to-leading order from [103] are used. The limits on the BRs in NLO calculation are $BR(t \to ug) < 3.9 \times 10^{-4}$ and $BR(t \to cg) < 5.7 \times 10^{-3}$, also shown in figure 6.3.
As already discussed in section 1.2.2, the branching ratio $BR(t \to cg)$ is expected to be at the level of $\approx 10^{-4}$ in the unconstrained Minimal Supersymmetric Standard Model (MSSM), while in the R-parity violating MSSM, the same BR is at the level of $\approx 10^{-3}$ [18]. The branching ratios of the gtc and the gtu couplings differ in about an order of magnitude from each other. This shows that the results of this analysis almost reach the predicted values for the enhanced FCNC in some SUSY scenarios. Yet we cannot exclude any specific scenario, since the prediction still lies within the experimental limit.

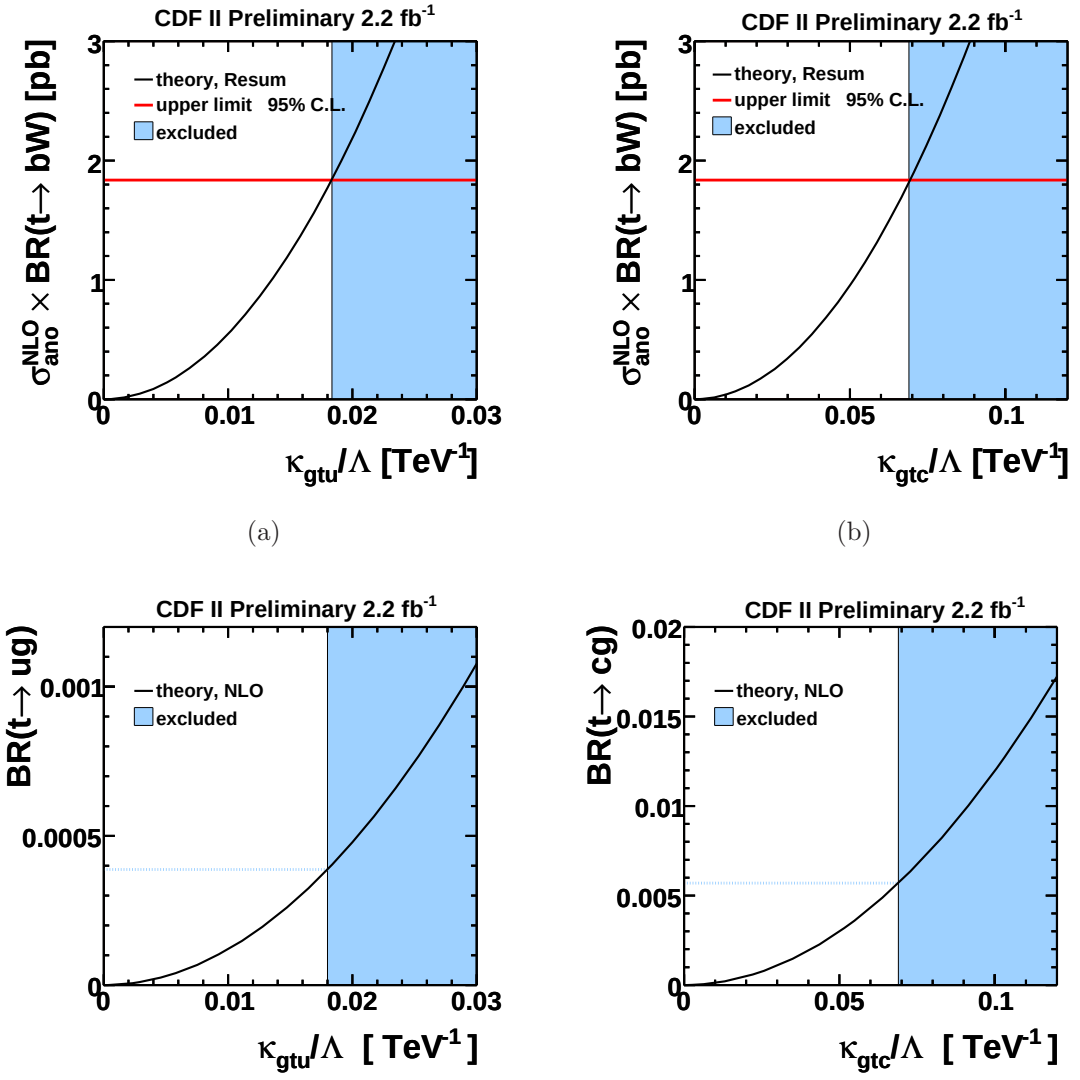

Figure 6.3: (a), (b): Upper limit on the anomalous cross section (in red). The black line is the theoretical prediction (Resum [34]). As a result, the colored region is excluded by the measurement, which sets an upper limit of 0.018 TeV^{-1} for κ_{gtu}/Λ and an upper limit of 0.069 TeV^{-1} for κ_{gtc}/Λ. (c), (d): Upper limit on the anomalous branching ratios. The black line is the theoretical prediction (NLO [103]). As a result, the colored region is excluded by the measurement, which sets an upper limit of 3.9×10^{-4} for $BR(t \to ug)$ and an upper limit of 5.7×10^{-3} for $BR(t \to cg)$.

Chapter 7

Summary

This analysis is focused on the search for the anomalous top-quark production mode $u(c) + g \rightarrow t$ via flavor-changing neutral currents (FCNC) in $p\bar{p}$ collision data at $\sqrt{s} = 1.96$ TeV, corresponding to an integrated luminosity of 2.2 fb^{-1}. The data were collected by the CDF II detector at the Fermilab Tevatron between March 2002 and August 2007.

This study was motivated by theoretical predictions to find hints for new physics, since FCNC are strongly suppressed in the SM. Typical branching ratios (BR) in the top-quark sector are expected at order of BR $\approx 10^{-14} - 10^{-10}$. My aim was to search for these interactions or set a limit on the production cross-section of the anomalous top quark if no signal is found, which turned out to be the case in this analysis. The experimentally obtained limit on the cross section would then allow the deduction of an upper an upper limit for the anomalous coupling constants κ_{gtu}/Λ and κ_{gtc}/Λ and for the anomalous branching ratios $BR(t \rightarrow ug)$ and $BR(t \rightarrow cg)$. The study was done in a model-independent way, by assuming an effective theory, which, for a given parameter space for the anomalous coupling constant, predicts the anomalous top-quark production to take place, while the top-quark decays subsequently Standard Model-like. In this thesis, I make use of this effect and search the data corresponding to the Standard Model leptonic decay-signature of the top-quark $t \rightarrow bW \rightarrow b\ell\nu_\ell$ in order to draw conclusions for the anomalous top-quark production cross-section. The leptonic decay signature consists of a lepton and missing energy (neutrino), which originate from the leptonic decay of the W boson and a bottom-quark jet.

The experimental methods used for this analysis can be summarized in four main categories. The first method is the Monte Carlo simulation. Various MC generators were introduced in order to produce the signal and background samples needed to describe the measured data. The signal process was simulated particularly for this analysis with the TopReX LO MC generator. The latter was found appropriate to implement to this study, since it contains special features and is thus able to reproduce the effects of the anomaly in the direct production of the top quark. The second and third experimental method are the detector simulation and the event reconstruction, respectively. The detector simulation is based on the programs GEANT

and GFLASH, while the event reconstruction includes the reconstruction of charged particles' tracks, jets, the primary and secondary vertex and the identification of leptons. Finally, the analytical instrumentation used in this thesis to extract the signal from the data, is a neural network, trained for this specific search. After estimating the expected events for each of the processes contributing to the amount of data, several input variables for the neural network were investigated in order to achieve the highest discriminating performance between signal and background events in the W+1-jet bin with 1 b tag. About 30 such variables were considered and finally 14 have been chosen as appropriate for this analysis.
The relevance and the correlation between the input variables in the training of the network was thoroughly investigated. In addition, data and simulation were compared for each of the variables and quality tests were performed with satisfying results. Moreover, an extra neural network, trained with samples that possess no assigned b tag in the W+1-jet bin, was used as a cross check. The latter showed that the modeling is adequate. After making sure that the neural network is functioning properly, it was used to distinguish between the modeled signal and background processes.
Before fitting the output of the neural network to the data, all systematic sources were investigated and taken into account. Furthermore, ensemble tests were used to obtain a measure for the a-priori sensitivity under the assumption there is no anomalous top-quark production. The last stage of this analysis, is the application to observed events. A binned likelihood fit method was used to fit the expectation to the data. Since no evidence of anomalous top-quark production via FCNC could be found, an upper limit on the latter's cross section was set. The experimentally deduced upper limit is 1.8 pb and lies within the range of the calculated sensitivity of this analysis.
In order to extract the information about the upper limit on the anomalous coupling constants, I used theoretical predictions which include threshold resummation effects leading to a higher cross section for a given coupling and thus give a stricter limit on the formers than LO and NLO calculations. I find $\kappa_{gtu}/\Lambda < 0.018$ TeV^{-1}, assuming $\kappa_{gtc} = 0$ and $\kappa_{gtc}/\Lambda < 0.069$ TeV^{-1}, assuming $\kappa_{gtu} = 0$. For the case $\kappa_{gtu}/\Lambda = \kappa_{gtc}/\Lambda = \kappa/\Lambda$ we find $\kappa/\Lambda = 0.017$ TeV^{-1}.
Finally, I was able to convert the experimental limit on the anomalous top-quark cross section to limits on the NLO branching ratios, using recently published theoretical calculations in next-to-leading order. The branching ratios are in this way constrained to $BR(t \to ug) < 3.9 \times 10^{-4}$ and $BR(t \to cg) < 5.7 \times 10^{-3}$.

It is useful to compare these new results to existing limits. The DØ collaboration, having set the strictest upper limits to date before this analysis was complete, do not present an experimental limit on the production cross section of $u(c) + g \to t$, they have published the upper limits on the coupling constants, $\kappa_{gtu}/\Lambda < 0.037$ TeV^{-1} and $\kappa_{gtc}/\Lambda < 0.15$ TeV^{-1}, using 230 pb^{-1} of their data. These limits correspond to $BR(t \to ug) < 1.64 \times 10^{-3}$ and $BR(t \to cg) < 2.69 \times 10^{-2}$. One has to mention here that the DØ analysis was done considering $2 \to 2$ FCNC subprocesses, while my analysis is the first to use the $2 \to 1$ signature. The results of my thesis give

an improvement of 51% and 54% over the existing upper limits on the coupling constants κ_{gtu}/Λ and κ_{gtc}/Λ, respectively, and an improvement of 76% and 79% over the existing upper limits on the branching ratios $BR(t \to ug)$ and $BR(t \to cg)$, respectively. They have been recently published and can be found in reference [104]. The branching ratio $BR(t \to cg)$ is expected to be at the level of $\approx 10^{-4}$ in the unconstrained Minimal Supersymmetric Standard Model (MSSM), while in the R-parity violating MSSM, the same BR is at the level of $\approx 10^{-3}$ [18]. The branching ratios of the gtc and the gtu couplings differ in about an order of magnitude from each other. This shows that the results of this analysis almost reach the predicted values for the enhanced FCNC in some SUSY scenarios. Yet we cannot exclude any specific scenario, since the prediction still lies within the experimental limit. References [105] and [106] suggest, that the branching ratios concerning the unconstrained MSSM will be probably measurable at the a next-generation hadron collider, while the effects in the R-parity violating version will be definitely measurable at the LHC.

Appendix A

Good Run List

141544	141572	141576	141577	141597	141598	141618	141619	141621
141660	141984	141989	142106	142107	142108	142109	142110	142111
142168	142170	142177	142202	144574	144575	144576	144578	144624
144628	144673	144674	144694	144696	144713	144714	144883	144884
145005	145006	145032	145033	145034	145035	145036	145044	145045
145532	145608	145651	145654	146850	146851	146920	147165	147804
147805	147806	147830	147832	147834	147835	147836	147837	147843
147865	147866	147869	148152	148153	148154	148157	148291	148293
148375	148648	148649	148674	148774	148775	148824	148825	148846
148852	148856	148857	148858	148908	148916	148950	148951	148953
149052	149053	149055	149056	149058	149059	149264	149354	149355
149386	149387	149481	149492	149493	149663	149677	149678	149680
149681	149682	149685	150010	150063	150066	150067	150070	150079
150080	150086	150087	150088	150108	150109	150110	150112	150113
150117	150118	150139	150140	150141	150145	150149	150287	150288
150289	150291	150340	150395	150415	150416	150418	150419	150420
150421	150422	150427	150428	150432	150433	150435	150443	150444
150799	150801	150802	150803	150805	150819	150820	150821	150823
150824	150853	151434	151435	151436	151449	151476	151477	151483
151509	151513	151514	151515	151555	151556	151557	151628	151641
151683	151688	151810	151811	151841	151842	151843	151844	151845
151868	151869	151870	151871	151872	151873	151902	151903	151906
151907	151911	151917	151918	151919	151920	151922	151971	151974
151978	152170	152266	152267	152270	152271	152274	152459	152464
152504	152507	152510	152514	152516	152517	152518	152520	152554
152555	152556	152559	152579	152598	152599	152600	152601	152602
152615	152616	152669	152674	152675	152680	152743	152745	152746
152747	152752	152772	152773	152809	152810	152811	152949	152953
152954	153061	153068	153074	153075	153076	153087	153091	153266
153268	153271	153325	153327	153343	153344	153345	153372	153373

153374	153389	153411	153412	153416	153447	153460	153557	153618
153620	153660	153661	153662	153693	153694	153697	153718	153738
153739	154021	154028	154029	154030	154118	154122	154126	154175
154176	154180	154208	154449	154451	154452	154453	154518	154653
154654	154675	154681	155113	155114	155115	155116	155121	155129
155130	155141	155145	155146	155148	155150	155299	155301	155304
155312	155313	155318	155320	155324	155343	155344	155345	155346
155347	155364	155365	155368	155389	155392	155393	155394	155409
155677	155678	155711	155712	155714	155742	155743	155744	155746
155747	155763	155764	155767	155768	155770	155793	155794	155795
155796	155818	155820	155821	155895	155918	155919	155920	155923
155996	155997	156006	156007	156081	156082	156083	156084	156087
156088	156089	156098	156100	156103	156112	156116	156117	156118
156369	156372	156401	156452	156457	156458	156460	156464	156484
156487	159603	160092	160151	160152	160153	160157	160175	160230
160301	160302	160303	160312	160314	160346	160359	160403	160405
160406	160407	160408	160410	160412	160414	160437	160440	160441
160533	160534	160541	160591	160592	160594	160596	160599	160601
160659	160663	160796	160802	160823	160886	160887	160890	160891
160987	160988	160989	161011	161013	161029	161031	161044	161170
161171	161324	161327	161330	161379	161408	161409	161411	161414
161415	161441	161552	161555	161633	161634	161638	161678	161713
161714	161718	161722	161754	161756	161757	161758	161760	161761
161762	161763	161778	161779	161780	161781	161783	161784	161786
161787	161788	161789	161790	161791	161792	161795	161817	161818
161820	161821	161823	161825	161826	161827	161829	161830	162130
162174	162175	162178	162238	162241	162252	162300	162301	162307
162310	162312	162393	162396	162399	162423	162453	162454	162462
162479	162480	162481	162498	162519	162520	162521	162631	162663
162664	162685	162686	162820	162825	162836	162837	162838	162839
162855	162856	162857	162937	162982	162986	163009	163011	163012
163025	163026	163035	163064	163113	163130	163136	163148	163385
163390	163394	163430	163431	163462	163463	163464	163474	163508
163510	163511	163512	163513	163515	163519	163526	163527	163960
164107	164109	164110	164128	164200	164235	164252	164257	164259
164261	164274	164303	164304	164305	164306	164307	164308	164352
164354	164386	164451	164509	164510	164511	164512	164517	164555
164625	164819	164820	164822	164844	164916	164952	164958	164963
164989	165062	165063	165064	165087	165088	165120	165121	165122
165199	165200	165201	165204	165207	165267	165269	165271	165297
165313	165314	165356	165357	165364	165365	165388	165412	165435
165436	165439	165470	165523	165836	165839	165869	165871	165873
165902	165906	165941	165944	165949	166007	166008	166037	166038
166063	166073	166227	166251	166325	166328	166367	166369	166371

166373	166374	166403	166406	166407	166472	166479	166482	166525
166529	166567	166614	166615	166653	166654	166655	166656	166657
166661	166662	166714	166715	166717	166770	166771	166772	166774
166776	166779	166783	166805	166927	166935	167023	167025	167053
167058	167059	167061	167138	167139	167186	167259	167261	167266
167290	167297	167299	167325	167444	167445	167506	167541	167551
167563	167565	167588	167623	167629	167631	167634	167635	167715
167717	167824	167849	167856	167865	167866	167954	167955	167956
167977	167996	167997	167998	168000	168001	168087	168089	168092
168559	168561	168563	168568	168599	168600	168601	168603	168605
168640	168766	168767	168770	168774	168775	168820	168822	168823
168889	175066	175078	175079	175090	175092	175095	175096	175143
175146	175147	175148	175150	175155	175195	175196	175283	175288
175289	175292	176651	176655	176695	176696	177214	177217	177301
177304	177313	177314	177315	177316	177337	177339	177340	177342
177345	177363	177364	177366	177370	177371	177384	177411	177412
177414	177415	177416	177417	177418	177478	177480	177485	177486
177487	177488	177490	177491	177624	177625	177628	177633	177793
177797	177798	177799	177800	177927	177932	177937	177938	177941
178015	178063	178064	178065	178066	178067	178068	178070	178071
178072	178073	178074	178076	178077	178080	178119	178120	178145
178146	178151	178154	178155	178156	178164	178165	178255	178256
178258	178260	178261	178262	178280	178295	178297	178298	178301
178303	178304	178305	178307	178310	178339	178389	178390	178391
178397	178400	178402	178405	178409	178432	178433	178434	178435
178437	178438	178440	178448	178450	178513	178536	178537	178539
178540	178546	178547	178602	178677	178683	178684	178735	178738
178741	178743	178744	178757	178758	178759	178761	178785	178816
178852	178853	178854	178855	178862	178881	178882	178886	178887
178888	178889	178921	179018	179019	179021	179037	179039	179040
179042	179043	179054	179055	179056	182843	182873	182874	183055
183057	183058	183077	183078	183079	183094	183097	183124	183125
183126	183129	183130	183139	183142	183165	183207	183209	183491
183492	183530	183553	183557	183561	183617	183619	183631	183633
183695	183696	183702	183752	183759	183760	183761	183783	183785
183861	183863	183864	183865	183913	183914	183915	183960	183961
183963	183965	183966	183968	183970	183971	184012	184015	184021
184059	184060	184062	184064	184067	184068	184069	184071	184072
184073	184078	184079	184081	184084	184204	184205	184206	184234
184237	184240	184243	184289	184290	184291	184310	184311	184314
184370	184377	184380	184414	184419	184424	184444	184445	184450
184453	184456	184459	184463	184464	184466	184467	184469	184492
184495	184516	184518	184519	184729	184730	184731	184732	184733
184738	184762	184763	184765	184778	184779	184780	184782	184800

184801	184802	184832	184835	184868	184957	185009	185017	185018
185037	185040	185072	185075	185082	185172	185176	185201	185220
185223	185248	185249	185250	185259	185260	185262	185277	185280
185281	185331	185332	185349	185351	185374	185375	185376	185377
185379	185381	185383	185384	185386	185516	185517	185518	185521
185522	185524	185542	185545	185594	185595	185634	185637	185640
185643	185644	185721	185723	185725	185726	185727	185728	185777
185782	185847	185848	185849	185962	185968	185969	185970	185971
185973	186039	186040	186041	186047	186048	186049	186083	186084
186087	186088	186090	186091	186092	186145	186302	186306	186308
186316	186321	186573	186575	186586	186591	186598	191208	191289
191290	191428	191430	191433	191534	191543	191545	191560	191565
191567	191568	191596	191636	191637	191638	191640	191724	191727
191765	191766	191769	191778	191783	191786	191803	192230	192232
192237	192243	192282	192296	192297	192299	192300	192302	192306
192344	192345	192348	192351	192354	192360	192362	192364	192365
192368	192370	192372	192373	192374	192376	192384	192386	192390
192399	192424	192439	192440	192441	192792	192793	192794	192868
192871	192878	192892	192893	192917	192918	192923	192982	192984
192987	192988	192994	192995	192996	193007	193013	193015	193017
193029	193030	193031	193031	193032	193049	193051	193061	193104
193105	193106	193107	193110	193164	193167	193242	193247	193271
193272	193275	193372	193377	193396	193458	193459	193461	193462
193463	193464	193466	193467	193468	193469	193470	193472	193475
193479	193485	193487	193488	193855	193856	193888	193892	193901
193908	193909	193910	193911	193912	193985	193987	193988	193989
193990	193991	193993	193996	194005	194007	194023	194025	194027
194028	194029	194030	194031	194032	194033	194039	194043	194146
194147	194149	194152	194161	194219	194260	194261	194263	194264
194265	194266	194315	194318	194320	194323	194326	194328	194337
194379	194382	194383	194386	194403	194407	194454	194455	194458
194459	194460	194498	194504	194535	194536	194538	194539	194560
194562	194590	194601	194602	194810	194813	194844	194845	194850
194860	194861	194862	194899	194900	194903	194905	194907	194911
194920	195210	195211	195246	195267	195313	195316	195341	195343
195346	195382	195383	195384	195402	195405	195408	195449	195450
195451	195452	195457	195624	195638	195678	195678	195704	195716
195718	195719	195720	195740	195741	195742	195745	195746	195756
195758	195759	195762	195780	195781	195786	195787	195788	195790
195791	195804	195805	195809	195814	195930	196043	196045	196077
196085	196099	196100	196152	196153	196163	196169	196170	196183
196228	196229	196230	196231	196232	196275	196276	196346	196352
196354	196365	196366	196368	196370	196419	196423	196425	196427
196440	196441	196471	196473	196483	196489	196661	196663	196664

196737	196737	196752	196795	196796	196878	196879	196886	196892
196893	196901	196902	196946	196948	196989	197071	197079	197080
197103	197118	197186	197188	197189	197191	197192	197194	197286
197287	197289	197317	197321	197404	197405	197440	197441	197636
197640	197644	197657	197713	197714	197715	197716	197762	197763
197808	197809	197812	197813	197985	197990	197995	197998	197999
198082	198116	198117	198152	198154	198159	198162	198206	198207
198379	198380	198416	198423	198513	198514	198557	198583	198596
198613	198623	198686	198695	198696	198709	198710	198711	198739
198782	198843	198881	198882	199025	199028	199041	199141	199142
199143	199146	199148	199152	199154	199156	199157	199158	199186
199187	199189	199189	199216	199217	199218	199223	199225	199559
199593	199594	199595	199618	199619	199620	199650	199652	199653
199655	199657	199725	199727	199852	199853	199853	199979	199983
200004	200023	200026	200027	200028	200049	200051	200055	200056
200058	200059	200196	200197	200274	200282	200284	200309	200324
200533	200534	200535	200536	200570	200572	200635	200641	200659
200660	200661	200663	200664	200669	200710	200719	200725	200752
200756	200883	200894	200896	200970	201037	201038	201039	201041
201072	201083	201131	201132	201133	201152	201154	201969	202002
202003	202041	202070	202073	202075	202081	202087	202088	202134
202135	202135	202136	202156	202174	202175	202290	202306	202307
202312	202313	202321	202334	202335	202336	202353	202363	202364
202365	202370	202389	202392	202393	202395	202396	202397	202399
202415	202424	202449	202513	202514	202526	202535	202536	202538
202539	202540	202542	202600	202697	202722	202723	202724	202732
202733	202736	202738	202739	202741	202770	202771	202817	202973
202998	203000	203001	203015	203020	203055	203066	203067	203091
203139	203141	203150	203153	203155	203190	203195	203202	203206
203212	203213	203262	203263	203265	203304	203309	203334	203335
203336	203345	203347	203383	203435	203437	203439	203442	203443
203453	203454	203456	203457	203488	203502	203506	203509	203625
203626	203634	203643	203650	203663	203673	203683	203685	203686
203687	203764	203765	203797	203797	203799	203819	203824	203826
203869	203871	203872	203873	203874	203881	203896	204076	204077
204082	204105	204111	204116	204118	204184	204185	204204	204211
204216	204257	204262	204264	204265	204266	204287	204339	204340
204378	204400	204402	204413	204444	204447	204469	204471	204478
204479	204480	204549	204550	204576	204578	204589	204591	204593
204594	204596	204639	204640	204642	204643	204650	204677	204679
204680	204682	204695	204714	204720	204721	204722	204746	204747
204748	204750	204827	204829	204832	204835	204855	204857	204921
204927	204928	204929	205007	205008	205009	205018	205021	205069
205070	205072	205073	205074	205075	205078	205079	205143	205151

205152	205153	205154	205309	205310	205311	205312	205314	205315
205317	205318	205320	205321	205322	205324	205325	205548	205549
205555	205556	205558	205560	205562	205563	205577	205624	205627
205628	205640	205641	205642	205647	205648	205716	205719	205720
205889	205890	205891	205960	205963	205964	205966	205968	205970
205990	205991	205994	205995	206029	206031	206033	206174	206186
206248	206251	206255	206256	206257	206259	206279	206281	206282
206283	206285	206288	206297	206298	206300	206301	206306	206326
206436	206445	206531	206537	206668	206669	206671	206693	206695
206697	206717	206719	206722	206723	206733	206828	206829	206830
206840	206867	206871	206951	206981	206982	206989	206990	206995
207000	207078	207079	207080	207114	207115	207151	207153	207158
207211	207214	207215	207217	207219	207405	207411	207414	207421
207488	207512	207513	209018	209019	209020	209021	209047	209048
209049	209050	209051	209052	209053	209070	209072	209085	209102
209106	209123	209149	209155	209159	209172	209186	209189	209191
209261	209262	209263	209265	209316	209318	209341	209372	209373
209399	209400	209401	209402	209436	209437	209439	209465	209484
209485	209486	209489	209491	209492	209494	209498	209501	209506
209507	209511	209513	209531	209532	209534	209535	209537	209541
209760	209761	209762	209764	209770	209772	209773	209789	209790
209818	209819	209848	209849	209850	209861	209862	209904	209907
209911	209920	209921	209979	209982	209983	209984	209986	210008
210846	210859	210877	210891	210914	211130	211135	211198	211200
211265	211267	211268	211271	211272	211274	211275	211292	211311
211312	211314	211315	211316	211337	211396	211397	211398	211399
211402	211403	211404	211405	211441	211448	211449	211452	211631
211633	211867	211870	211871	211873	211877	211882	211883	211903
212009	212011	212133	218399	218424	218426	218623	218624	218625
218626	218627	218653	218654	218658	218692	218695	218713	219023
219025	219030	219033	219035	219041	219082	219091	219092	219095
219108	219139	219219	219221	219222	219223	219224	219225	219232
219237	219265	219266	219267	219268	219269	219306	219313	219357
219358	219381	219382	219383	219384	219385	219386	219462	219463
219469	219471	219472	219475	219476	219477	219479	219519	219526
219528	219539	219567	219568	219569	219570	219606	219607	219609
219612	219659	219673	219705	219789	219790	219879	219880	219885
219888	219891	219892	219896	219897	219943	219945	219946	219964
219967	219971	219972	219974	219975	220067	220071	220072	220072
220072	220080	220182	220183	220184	220217	220218	220219	220221
220224	220226	220227	220246	220247	220248	220256	220269	220272
220508	220509	220510	220511	220547	220578	220579	220589	220591
220604	220724	220725	220726	220727	220730	220731	220732	220844
220845	220847	220859	220898	221168	221169	221173	221174	221201

221223	221224	221296	221297	221334	221464	221499	221500	221528
221532	221537	221604	221605	221657	221658	221722	221723	221751
221804	221808	221827	221844	221904	221911	221917	221918	221920
222009	222011	222246	222250	222252	222253	222254	222271	222279
222288	222290	222314	222322	222326	222332	222353	222354	222356
222357	222364	222417	222418	222419	222426	222530	222532	222533
222549	222552	222556	222576	222604	222610	222648	222652	222655
222722	222724	222727	222728	222778	222779	222780	222791	222792
222793	222797	222801	222802	222809	222811	222833	222834	222835
222840	222841	222850	222854	222866	222867	222882	222885	222886
222888	222946	222947	222957	223118	223119	223120	223158	223160
223162	223177	223233	223236	223240	223309	223325	223329	223330
223331	223332	223338	223339	223369	223432	223481	223485	223494
223498	223501	223535	223536	223538	223624	223634	223637	223641
223642	224057	224068	224070	224085	224087	224115	224116	224120
224126	224161	224171	224365	224366	224367	224390	224423	224442
224445	224478	224480	224481	224521	226196	226224	226246	226252
226253	226254	226297	226311	226336	226350	226363	226365	226406
226407	227377	227380	227456	227554	227704	227708	227709	227710
227711	227718	227720	227721	227722	227723	227724	227726	227728
227730	227747	227749	227750	227782	227806	227808	227809	227834
227867	227881	227882	227883	227884	227885	227886	227892	227897
227903	228163	228397	228399	228400	228402	228405	228406	228450
228536	228575	228576	228588	228596	228664	228683	228693	228694
228698	228699	228734	228735	228738	228741	228763	228786	228819
228824	228827	228838	228849	228853	228873	228874	228875	228876
228878	228902	228995	229040	229084	229116	229170	229202	229204
229205	229313	229332	229335	229385	229388	229389	229408	229438
229448	229451	229490	229534	229664	229672	229674	229675	229676
229688	229757	229759	229764	229772	229788	229789	229790	229877
229879	229881	229896	229928	229934	229936	230005	230008	230010
230058	230078	230419	230435	230460	230461	230486	230487	230489
230507	230508	230509	230536	230536	230560	230562	230563	230565
230566	230568	230599	230615	230620	230621	230628	230769	230770
230778	230782	230795	230887	230896	230921	230923	230946	230947
230965	230993	230996	231022	231060	231081	231082	231083	231084
231123	231124	231126	231130	231153	231155	231156	231161	231179
231201	231203	231250	231264	231289	231294	231298	231334	231452
231453	231454	231478	231479	231481	231490	231491	231514	231628
231693	231712	231741	231781	231905	231907	231924	231927	231929
231964	231973	232025	232027	232028	232062	232065	232086	232087
232088	232089	232090	232098	232185	232226	232240	232261	232264
232282	232283	232286	232297	232428	232429	232436	232443	232444
232445	232456	232459	232492	232493	232495	232496	232500	232510

232522	232711	232770	232781	232802	232803	232804	232812	232840
232841	233028	233030	233031	233035	233050	233070	233071	233076
233077	233078	233080	233081	233097	233098	233109	233110	233111
233133	233134	233171	233174	233175	233610	233614	233618	233650
233656	233743	233764	233798	233830	233846	233864	233869	233929
234054	234265	234269	234313	234314	234317	234339	234398	234409
234411	234413	234463	234471	234481	234571	234572	234587	234588
234589	234591	234653	234663	234669	234673	234677	234753	234754
234864	234875	234917	234931	234972	234985	235001	235002	235003
235056	235073	235091	235092	235093	235114	235158	235159	235160
235163	235181	235190	235195	235224	235232	235389	235422	235423
235428	235430	235593	235594	235648	235663	235757	235765	235774
235777	235780	235791	235814	235830	235917	235924	235932	235982
235983	235993	236023	236039	236040	236132	236168	236254	236255
236256	236284	236286	236389	236399	236403	236503	236515	236517
236524	236543	236580	236585	236631	236653	236753	236756	236759
236760	236761	236762	236763	236764	236780	236781	236806	236878
236879	236893	236965	237003	237045	237079	237093	237105	237108
237118	237122	237143	237144	237153	237226	237227	237294	237308
237309	237310	237311	237313	237335	237346	237478	237522	237539
237705	237795	237850	237851	237972	237980	237981	237983	237984
238234	238235	238240	238241	238341	238342	238347	238451	238452
238453	238454	238457	238493	238497	238513	238792	238794	238817
238877	238917	238920	238926	238927	238952	238981	238989	239000
239076	239101	239207	239210	239216	239218	239230	239252	239256
239276	239277	239334	239338	239347	239350	239354	239356	239451
239487	239504	239552	239641	239652	239671	239823	239853	239899
239900	239901	239905	239906	239923	239936	239955	239967	239974
239976	240033	240034	240035	240037	240066	240074	240087	240094
240097	240115	240130	240230	240250	240262	240296	240297	240386
240393	240394	240399	240445	240449	240451	240468	240610	240611
240618	240620	240630	240631	240632	240633	240645	240647	240652
240669	240672	240673	240788	240790	240801	240803	240804	240833
240836	240837	240839	240840	240841	240842	240843	240844	240871
240872	240873	240893	240894	240895	240905	240912	240916	240957
240964	240988	240995	240996	241002	241038	241051	241060	241109
241110	241181	241256	241271	241491	241511	241584	241614	241615
241616	241617	241640	241664	241665	242031	242033	242036	242037
242040	242041	242043	242101	242102	242166	242167	242168	242289
242290	242291	242347	242348	242349	242351	242352	242354	242355
242356	242364	242381	242382	242488	242489	242557	242558	242565
242582	242583	242587	242588	242589	242595	242640	242646	242648
242649	242650	242651	242654	242658	242662	242665	242666	242668
242693	242694	242695	242696	242698	242699	242705	242706	242707

242708	242710	242725	242727	242728	242729	242730	242734	242762
242764	242766	242768	242769	242791	242860	242861	242862	242863
242864	242865	242869	242872	242877	242880	242882	242883	242887
242889	242890	243027	243028	243029	243030	243033	243036	243037
243040	243041	243070	243117	243149	243163	243168	243174	243221
243223	243224	243237	243238	243252	243253	243254	243255	243274
243350	243352	243354	243402	243409	243411	243413	243419	243420
243422	243423	243425	243426	243521	243523	243648	243650	243655
243663	243668	243674	243675	243711	243712	243713	243715	243730
243732	243744	243787	243792	243808	243809	243834	243837	243839
243840	243841	243842	243843	243919	243928	243932	243995	243997
243998	244006	244007	244186	244187	244188	244189	244190	244191
244194	244199	244297	244298	244299	244335	244340	244342	244344
244346	244417	244420	244451	244453	244455	244457	244460	244465
244484	244485	244487	244495	244496	244497	244498	244501	244519
244521	244522	244524	244537	244544	244545	244649	244651	244655
244674	244676	244696	244697	244720	244751	244752	244754	244761
244789	244792	244933	244940	244941	244963	244966	244983	244996
244998	245001	245021	245057	245058	245059	245060	245063	245091
245102	245210	245218	245222	245224	245231	245280	245283	245284
245285	245292	245369	245371	245375	245448	245454	245464	245480
245485	245490	245494	245516	245518	245639	245646	245712	245713
245715	245716	245772	245773	245779	245783	245785	245821	245823
245824	245825	245826	245839	245865	245974	245979	245981	245984
245985	245986	246023	246025	246051	246056	246066	246074	246077
246078	246082	246083	246110	246111	246112	246116	246124	246125
246127	246128	246132	246133	246134	246136	246140	246153	246160
246186	246187	246223	246226	246229	246231			

Table A.1: The "goodrun" list version 19, used for this analysis.

Appendix B

Used Data and MC Samples

In the search of anomalous top-quark production, a set of Monte Carlo simulated samples (see table B.8) is used to model the selected data sample. The parton level of anomalous top-quark production is simulated with TopReX and the showering of the process is done with PYTHIA. Anomalous top-quark production is simulated with the matrix element generator MADEVENT and PYTHIA showering. For the modeling of $t\bar{t}$, diboson, and Z+jets production, simulated events generated with PYTHIA are used. W+heavy flavor events were simulated using a combination of ALPGEN and HERWIG. In addition, this combination forms the basis for the mistag model used in this analysis.

sample	process	origin	events
`bhel0d, bhmu0d, bpel0d`	data	CDF detector	$1016 \cdot 10^6$
`bhel0h, bhmu0h, bpel0h`	data	CDF detector	$754 \cdot 10^6$
`bhel0i, bhmu0i, bpel0i`	data	CDF detector	$1548 \cdot 10^6$
`bhel0j, bhmu0j, bpel0j`	data	CDF detector	$1560 \cdot 10^6$
`ttop6x`	AnoTop	TopReX + PYTHIA	10^6
`stopm0`	t-channel	MADEVENT + PYTHIA	10^6
`stop00`	t-channel	MADEVENT + PYTHIA	10^6
`ttop75`	$t\bar{t}$	PYTHIA	$4.8 \cdot 10^6$

Table B.1: Monte Carlo samples used in the search for anomalous top-quark production.

sample	process	origin	events
btop0w	Wbb	ALPGEN + PYTHIA	$1.5 \cdot 10^6$
btop1w	Wbb	ALPGEN + PYTHIA	$1.5 \cdot 10^6$
btop2w	Wbb	ALPGEN + PYTHIA	$1.5 \cdot 10^6$
btop5w	Wbb	ALPGEN + PYTHIA	$1.5 \cdot 10^6$
btop6w	Wbb	ALPGEN + PYTHIA	$1.5 \cdot 10^6$
btop7w	Wbb	ALPGEN + PYTHIA	$1.5 \cdot 10^6$
dtop0w	Wbb	ALPGEN + PYTHIA	$1.5 \cdot 10^6$
dtop1w	Wbb	ALPGEN + PYTHIA	$1.5 \cdot 10^6$
dtop2w	Wbb	ALPGEN + PYTHIA	$1.5 \cdot 10^6$
ptopw0	Wbb	ALPGEN + PYTHIA	$5 \cdot 10^6$
ptopw1	Wbb	ALPGEN + PYTHIA	$5 \cdot 10^6$
ptop2w	Wbb	ALPGEN + PYTHIA	10^6
ptop3w	Wbb	ALPGEN + PYTHIA	10^6
ptop4w	Wbb	ALPGEN + PYTHIA	10^6
ptopw5	Wbb	ALPGEN + PYTHIA	$5 \cdot 10^6$
ptkt6w	Wbb	ALPGEN + PYTHIA	10^6
ptop7w	Wbb	ALPGEN + PYTHIA	10^6
ptop8w	Wbb	ALPGEN + PYTHIA	10^6
ptop9w	Wbb	ALPGEN + PYTHIA	10^6
utopw0	Wbb	ALPGEN + PYTHIA	$5 \cdot 10^6$
utop2w	Wbb	ALPGEN + PYTHIA	10^6
utop3w	Wbb	ALPGEN + PYTHIA	10^6
utop4w	Wbb	ALPGEN + PYTHIA	10^6
ctop0w	Wbb	ALPGEN + PYTHIA	$2 \cdot 10^6$
ctop1w	Wbb	ALPGEN + PYTHIA	$2 \cdot 10^6$
ctop2w	Wbb	ALPGEN + PYTHIA	$2 \cdot 10^6$
ctop5w	Wbb	ALPGEN + PYTHIA	$2 \cdot 10^6$
ctop6w	Wbb	ALPGEN + PYTHIA	$2 \cdot 10^6$
ctop7w	Wbb	ALPGEN + PYTHIA	$2 \cdot 10^6$
etopw0	Wbb	ALPGEN + PYTHIA	$2 \cdot 10^6$
etopw1	Wbb	ALPGEN + PYTHIA	$2 \cdot 10^6$
etopw2	Wbb	ALPGEN + PYTHIA	$2 \cdot 10^6$

Table B.2: Monte Carlo samples used in the search for anomalous top-quark production.

sample	process	origin	events
stopw0	Wbb	ALPGEN + PYTHIA	$2 \cdot 10^6$
stopw1	Wbb	ALPGEN + PYTHIA	$2 \cdot 10^6$
stopw2	Wbb	ALPGEN + PYTHIA	$2 \cdot 10^6$
stopw3	Wbb	ALPGEN + PYTHIA	$2 \cdot 10^6$
stopw5	Wbb	ALPGEN + PYTHIA	$2 \cdot 10^6$
stopw6	Wbb	ALPGEN + PYTHIA	$2 \cdot 10^6$
stopw7	Wbb	ALPGEN + PYTHIA	$2 \cdot 10^6$
stopw8	Wbb	ALPGEN + PYTHIA	$2 \cdot 10^6$
stopwa	Wbb	ALPGEN + PYTHIA	$2 \cdot 10^6$
stopwb	Wbb	ALPGEN + PYTHIA	$1.5 \cdot 10^6$
stopwc	Wbb	ALPGEN + PYTHIA	$1.5 \cdot 10^6$
stopwd	Wbb	ALPGEN + PYTHIA	$1.5 \cdot 10^6$
ctop0w	$Wc\bar{c}$	ALPGEN + PYTHIA	$2 \cdot 10^6$
ctop1w	$Wc\bar{c}$	ALPGEN + PYTHIA	$2 \cdot 10^6$
ctop2w	$Wc\bar{c}$	ALPGEN + PYTHIA	$2 \cdot 10^6$
ctop5w	$Wc\bar{c}$	ALPGEN + PYTHIA	$2 \cdot 10^6$
ctop6w	$Wc\bar{c}$	ALPGEN + PYTHIA	$2 \cdot 10^6$
ctop7w	$Wc\bar{c}$	ALPGEN + PYTHIA	$2 \cdot 10^6$
etopw0	$Wc\bar{c}$	ALPGEN + PYTHIA	$2 \cdot 10^6$
etopw1	$Wc\bar{c}$	ALPGEN + PYTHIA	$2 \cdot 10^6$
etopw2	$Wc\bar{c}$	ALPGEN + PYTHIA	$2 \cdot 10^6$
ptopw0	$Wc\bar{c}$	ALPGEN + PYTHIA	$5 \cdot 10^6$
ptopw1	$Wc\bar{c}$	ALPGEN + PYTHIA	$5 \cdot 10^6$
ptop2w	$Wc\bar{c}$	ALPGEN + PYTHIA	10^6
ptop3w	$Wc\bar{c}$	ALPGEN + PYTHIA	10^6
ptop4w	$Wc\bar{c}$	ALPGEN + PYTHIA	10^6
ptopw5	$Wc\bar{c}$	ALPGEN + PYTHIA	$5 \cdot 10^6$
ptopw6	$Wc\bar{c}$	ALPGEN + PYTHIA	$5 \cdot 10^6$
ptop7w	$Wc\bar{c}$	ALPGEN + PYTHIA	10^6
ptop8w	$Wc\bar{c}$	ALPGEN + PYTHIA	10^6
ptop9w	$Wc\bar{c}$	ALPGEN + PYTHIA	10^6
utopw0	$Wc\bar{c}$	ALPGEN + PYTHIA	$5 \cdot 10^6$
utopw1	$Wc\bar{c}$	ALPGEN + PYTHIA	$5 \cdot 10^6$
utop2w	$Wc\bar{c}$	ALPGEN + PYTHIA	10^6
utop3w	$Wc\bar{c}$	ALPGEN + PYTHIA	10^6
utop4w	$Wc\bar{c}$	ALPGEN + PYTHIA	10^6

Table B.3: Monte Carlo samples used in the search for anomalous top-quark production.

sample	process	origin	events
ztopb0	Z+jets	ALPGEN + PYTHIA	$0.5 \cdot 10^6$
ztopb1	Z+jets	ALPGEN + PYTHIA	$0.5 \cdot 10^6$
ztopb2	Z+jets	ALPGEN + PYTHIA	$0.5 \cdot 10^6$
ztopb5	Z+jets	ALPGEN + PYTHIA	$0.5 \cdot 10^6$
ztopb6	Z+jets	ALPGEN + PYTHIA	$0.5 \cdot 10^6$
ztopb7	Z+jets	ALPGEN + PYTHIA	$0.5 \cdot 10^6$
ztopbt	Z+jets	ALPGEN + PYTHIA	$1.5 \cdot 10^6$
ztopc0	Z+jets	ALPGEN + PYTHIA	$0.7 \cdot 10^6$
ztopc1	Z+jets	ALPGEN + PYTHIA	$0.7 \cdot 10^6$
ztopc2	Z+jets	ALPGEN + PYTHIA	$0.7 \cdot 10^6$
ztopc5	Z+jets	ALPGEN + PYTHIA	$0.7 \cdot 10^6$
ztopc6	Z+jets	ALPGEN + PYTHIA	$0.7 \cdot 10^6$
ztopc7	Z+jets	ALPGEN + PYTHIA	$0.7 \cdot 10^6$
ztopct	Z+jets	ALPGEN + PYTHIA	$2 \cdot 10^6$
ztopt3	Z+jets	ALPGEN + PYTHIA	$6 \cdot 10^6$
ztopt4	Z+jets	ALPGEN + PYTHIA	$6 \cdot 10^6$
ztopt2	Z+jets	ALPGEN + PYTHIA	$2.4 \cdot 10^6$
itopww	WW	PYTHIA	$2.4 \cdot 10^6$
itopwz	WZ	PYTHIA	$2.4 \cdot 10^6$
itopzz	ZZ	PYTHIA	$2.4 \cdot 10^6$
ztopp1	mistags	ALPGEN + PYTHIA	$2.5 \cdot 10^6$
ztopzb	mistags	ALPGEN + PYTHIA	$4.5 \cdot 10^6$
ztopp6	mistags	ALPGEN + PYTHIA	$2.5 \cdot 10^6$
ztopzt	mistags	ALPGEN + PYTHIA	$4.5 \cdot 10^6$

Table B.4: Monte Carlo samples used in the search for anomalous top-quark production.

sample	process	origin
topw0	mistags	ALPGEN + PYTHIA
tkt1w	mistags	ALPGEN + PYTHIA
top2w	mistags	ALPGEN + PYTHIA
top3w	mistags	ALPGEN + PYTHIA
top4w	mistags	ALPGEN + PYTHIA
topw5	mistags	ALPGEN + PYTHIA
tkt6w	mistags	ALPGEN + PYTHIA
top7w	mistags	ALPGEN + PYTHIA
top8w	mistags	ALPGEN + PYTHIA
top9w	mistags	ALPGEN + PYTHIA
nonW0d_anti-eleMuon	nonW mixed	DATA + ALPGEN
nonW0d_anti-ele	nonW mixed	DATA + ALPGEN
nonW0h_anti-eleMuon	nonW mixed	DATA + ALPGEN
nonW0h_anti-ele	nonW mixed	DATA + ALPGEN
nonW0i_anti-eleMuon	nonW mixed	DATA + ALPGEN
nonW0i_anti-ele	nonW mixed	DATA + ALPGEN
nonWmi_anti-eleMuon	nonW mixed	DATA + ALPGEN
nonWmi_anti-ele	nonW mixed	DATA + ALPGEN
nonWmi_v2_anti-eleMuon	nonW mixed	DATA + ALPGEN
nonWmi_v2_anti-ele	nonW mixed	DATA + ALPGEN
nonWmi2_anti-eleMuon	nonW mixed	DATA + ALPGEN
nonWmi2_anti-ele	nonW mixed	DATA + ALPGEN
nonWmi3_anti-eleMuon	nonW mixed	DATA + ALPGEN
nonWmi3_anti-ele	nonW mixed	DATA + ALPGEN
nonWmj_anti-eleMuon	nonW mixed	DATA + ALPGEN
nonWmj_anti-ele	nonW mixed	DATA + ALPGEN

Table B.5: Monte Carlo samples used in the search for anomalous top-quark production.

sample	process	origin
nonWmj_p12_anti-eleMuon	nonW mixed	DATA + ALPGEN
nonWmj_p12_anti-ele	nonW mixed	DATA + ALPGEN
nonWmj_p13_anti-eleMuon	nonW mixed	DATA + ALPGEN
nonWmj_p13_anti-ele	nonW mixed	DATA + ALPGEN
nonW0d_anti-eleMuonDoubleTag	nonW mixed	DATA + ALPGEN
nonW0d_anti-eleDoubleTag	nonW mixed	DATA + ALPGEN
nonW0h_anti-eleMuonDoubleTag	nonW mixed	DATA + ALPGEN
nonW0h_anti-eleDoubleTag	nonW mixed	DATA + ALPGEN
nonW0i_anti-eleMuonDoubleTag	nonW mixed	DATA + ALPGEN
nonW0i_anti-eleDoubleTag	nonW mixed	DATA + ALPGEN
nonWmi_anti-eleMuonDoubleTag	nonW mixed	DATA + ALPGEN
nonWmi_anti-eleDoubleTag	nonW mixed	DATA + ALPGEN
nonWmi_v2_anti-eleMuonDoubleTag	nonW mixed	DATA + ALPGEN
nonWmi_v2_anti-eleDoubleTag	nonW mixed	DATA + ALPGEN
nonWmi2_anti-eleMuonDoubleTag	nonW mixed	DATA + ALPGEN
nonWmi2_anti-eleDoubleTag	nonW mixed	DATA + ALPGEN
nonWmi3_anti-eleMuonDoubleTag	nonW mixed	DATA + ALPGEN
nonWmi3_anti-eleDoubleTag	nonW mixed	DATA + ALPGEN
nonWmj_anti-eleMuonDoubleTag	nonW mixed	DATA + ALPGEN
nonWmj_anti-eleDoubleTag	nonW mixed	DATA + ALPGEN
nonWmj_p12_anti-eleMuonDoubleTag	nonW mixed	DATA + ALPGEN
nonWmj_p12_anti-eleDoubleTag	nonW mixed	DATA + ALPGEN
nonWmj_p13_anti-eleMuonDoubleTag	nonW mixed	DATA + ALPGEN
nonWmj_p13_anti-eleDoubleTag	nonW mixed	DATA + ALPGEN

Table B.6: Monte Carlo samples used in the search for anomalous top-quark production.

sample	process	origin
gjt1kdEle	nonW mixed	DATA + ALPGEN
gjt1khEle	nonW mixed	DATA + ALPGEN
gjt1kiEle	nonW mixed	DATA + ALPGEN
gjt1miEle	nonW mixed	DATA + ALPGEN
gjt1mi_p8Ele	nonW mixed	DATA + ALPGEN
gjt1mi_p9Ele	nonW mixed	DATA + ALPGEN
gjt1mi_p10Ele	nonW mixed	DATA + ALPGEN
gjt1mj_p11Ele	nonW mixed	DATA + ALPGEN
gjt1mj_p12Ele	nonW mixed	DATA + ALPGEN
gjt1mj_p13Ele	nonW mixed	DATA + ALPGEN
gjt1kdMuon	nonW mixed	DATA + ALPGEN
gjt1khMuon	nonW mixed	DATA + ALPGEN
gjt1kiMuon	nonW mixed	DATA + ALPGEN
gjt1miMuon	nonW mixed	DATA + ALPGEN
gjt1mi_p8Muon	nonW mixed	DATA + ALPGEN
gjt1mi_p9Muon	nonW mixed	DATA + ALPGEN
gjt1mi_p10Muon	nonW mixed	DATA + ALPGEN
gjt1mj_p11Muon	nonW mixed	DATA + ALPGEN
gjt1mj_p12Muon	nonW mixed	DATA + ALPGEN
gjt1mj_p13Muon	nonW mixed	DATA + ALPGEN

Table B.7: Monte Carlo samples used in the search for anomalous top-quark production.

sample	process	origin
gjt1kdEleDoubleTag	nonW mixed	DATA + ALPGEN
gjt1khEleDoubleTag	nonW mixed	DATA + ALPGEN
gjt1kiEleDoubleTag	nonW mixed	DATA + ALPGEN
gjt1miEleDoubleTag	nonW mixed	DATA + ALPGEN
gjt1mi_p8EleDoubleTag	nonW mixed	DATA + ALPGEN
gjt1mi_p9EleDoubleTag	nonW mixed	DATA + ALPGEN
gjt1mi_p10EleDoubleTag	nonW mixed	DATA + ALPGEN
gjt1mj_p11EleDoubleTag	nonW mixed	DATA + ALPGEN
gjt1mj_p12EleDoubleTag	nonW mixed	DATA + ALPGEN
gjt1mj_p13EleDoubleTag	nonW mixed	DATA + ALPGEN
gjt1kdMuonDoubleTag	nonW mixed	DATA + ALPGEN
gjt1khMuonDoubleTag	nonW mixed	DATA + ALPGEN
gjt1kiMuonDoubleTag	nonW mixed	DATA + ALPGEN
gjt1miMuonDoubleTag	nonW mixed	DATA + ALPGEN
gjt1mi_p8MuonDoubleTag	nonW mixed	DATA + ALPGEN
gjt1mi_p9MuonDoubleTag	nonW mixed	DATA + ALPGEN
gjt1mi_p10MuonDoubleTag	nonW mixed	DATA + ALPGEN
gjt1mj_p11MuonDoubleTag	nonW mixed	DATA + ALPGEN
gjt1mj_p12MuonDoubleTag	nonW mixed	DATA + ALPGEN
gjt1mj_p13MuonDoubleTag	nonW mixed	DATA + ALPGEN

Table B.8: Monte Carlo samples used in the search for anomalous top-quark production.

List of Figures

List of Tables

Bibliography

[1] Th. Müller,
'Die Suche nach den Fundamentalen Bausteinen der Natur',
Talk given at the 'Physik am Samstag'-lecture series in Karlsruhe, Germany (2003).

[2] E. Noether,
Invariante Variationsprobleme. Nachr. v. d. Ges. d. Wiss. zu Goettingen, pages 235-257 (1918).

[3] C.Amsler *et al.* (Particle Data Group),
Phys. Lett. B 667, 1 (2008).

[4] P. W. Higgs,
Phys. Lett. 12, 132 (1964).

[5] CDF and DØ Collaborations,
arXiv:0903.4001v1 [hep-ex] (2009).

[6] M. Kobayashi and T. Maskawa,
'CP Violation in the Renormalizable Theory of Weak Interaction',
Prog. Theor. Phys. 49 (1973) 652.

[7] H.L. Lai *et al.* (CTEQ Collaboration),
Eur. Phys. J. C 12, 375 (2000), e-print Archive hep-ph/9903282.

[8] F. Abe *et al.* (CDF Collaboration),
Phys. Rev. D 50, 2966 (1994).

[9] *et al.*F. Abe *et al.* (CDF Collaboration),
Phys. Rev. Lett. 73, 225 (1994).

[10] S. Abachi *et al.* (DØ Collaboration),
Phys. Rev. Lett. 74, 2632 (1995).

[11] T. Aaltonen *et al.* (CDF Collaboration),
arXiv:0903.0885 (2009).

[12] V. M. Abazov *et al.* (DØ Collaboration),
arXiv:0903.0850 (2009).

[13] S. Moch and P. Uwer,
Phys. Rev. D 78, 034003 (2008).

[14] N. Kidonakis,
Phys. Rev. D 74, 114012 (2006).

[15] S. L. Glashow, J. Iliopoulos and L. Maiani,
Phys. Rev. D 2, 1585 (1970).

[16] H. Fritzsch,
Phys. Lett. B 224, 423 (1989).

[17] J. A. Aguilar-Saavedra,
Acta Phys. Polon. B 35, 2695 (2004).

[18] F. Larios, R. Martinez, M. A. Perez,
Int. J. Mod. Phys. A 21, 3473-3494 (2006).

[19] B. Grzadkowski, J. F. Gunion, and P. Krawczyk,
Phys. Lett. B 268, 106 (1991).

[20] G. Eliam, J. L. Hewett and A. Soni,
Phys. Rev. D 44, 1473 (1991).

[21] M. Luke and M. J. Savage,
Phys. Lett. B 307, 387 (1993).

[22] G. Couture, C. Hamzaoui and H. König,
Phys. Rev. D 52, 1713 (1993).

[23] Jorge L. Lopez, D. V. Nanopoulos and Raghavan Rangarajan,
Phys. Rev. D 56, 3100 (1997).

[24] T. P. Cheng and M. Sher,
Phys Rev. D 48, 3484 (1987).

[25] W. S. Hou,
Phys. Lett. B 296, 179 (1992).

[26] L. J. Hall and S. Weinberg,
Phys. Rev. D 48, 979 (1993).

[27] D. Atwood, L. Reina and A. Soni,
ibid. 53, 1199 (1996).

[28] C. T. Hill,
Phys. Lett. B 266, 419 (1991); 345, 483 (1995).

[29] B. Holdom,
ibid. 339, 114 (1994); 351, 279 (1995).

[30] H. Georgi, L. Kaplan, D. Morin and A. Schenk,
Phys. Rev. D 51, 3888 (1995).

[31] X. Zhang,
Phys. Rev. D 51, 5309 (1995).

[32] J. Berger, A. Blotz, H.-C. Kim and K. Goeke,
ibid. 54, 3598 (1996).

[33] J. J. Liu *et. al.*,
Phys. Rev. D 72, 074018 (2005).

[34] Li Lin Yang, Chong Sheng Li, Yang Gao, Jian Jun Liu,
Phys. Rev. D 73, 074017 (2006).

[35] Ehab Malkawi and Tim Tait,
'Top-Charm Strong Flavor-Changing Neutral Currents at the Tevatron',
hep-ph/9511337 (1995).

[36] M. Hosch, K. Whisnant and B.-L. Young,
'Direct top quark production at hadron colliders as a probe of new physics',
Phys. Rev. D 56, 9 (1997).

[37] Tim M. P. Tait and C.-P. Yuan,
'Single Top Production as a Window to Physics Beyond the Standard Model',
hep-ph/0007298 (2000).

[38] T. Han, K. Whisnant, B.-L. Young and X. Zhang,
Phys. Lett. B 385, 311 (1996).

[39] V. M. Abazov *et al.* (DØ Collaboration),
Phys. Rev. Lett. 99, 191802 (2007).

[40] ALEPH Collaboration,
Phys. Lett. B 543, 173-182 (2002).

[41] J. Abdallah *et al.* (DELPHI Collaboration),
Phys. Lett. B 590, 21-34 (2004).

[42] P. Achard *et al.* (L3 Collaboration),
Phys. Lett. B 549, 290 (2002).

[43] G. Abbiendi *et al.* (OPAL collaboration),
Phys. Lett. B 521, 181-194 (2001).

[44] A. Aktas *et al.* (H1 Collaboration),
Eur. Phys. J. C 33, 9 (2004).

[45] S. Chekanov *et al.* (ZEUS Collaboration),
Phys. Lett. B 559, 153.

[46] T. Aaltonen *et al.* (CDF Collaboration),
Phys. Rev. Lett. 101, 192002 (2008).

[47] P. H. Garbincius,
Tevatron collider operations and plans,
hep-ex/0406013 (2004).

[48] S. Klimenko *et al.*,
The CDF Run II Luminosity Monitor,
Internal CDF Note 4330 (1998).

[49] S. Klimenko *et al.*,
Luminosity Monitor Based on Cherenkov Counters for P-Pbar Colliders,
Nucl. Instr. Meth. A 441 (366-373) (2000).

[50] S. Klimenko *et al.*,
The CDF Run II Luminosity Monitor,
Nucl. Instr. Meth. A 461 (540-544) (2001).

[51] The CDF II Collaboration,
The CDF II Detector,
FERMILAB-PUB-96/39–E Technical Design Report (1996).

[52] A. Bhatti *et al.*,
Determination of the jet energy scale at the Collider Detector at Fermilab,
Nucl. Instrum. Meth. A 566, 375-412 (2006).

[53] M. G. Albrow *et al.*,
CDF Run II Triggers Table and Datasets Plan,
Internal CDF Note 4718 (2001).

[54] B. Ashmanskas *et al.*,
The CDF silicon vertex trigger,
Nucl. Instrum. Meth. A 518, 532-536 (2004).

[55] G. Gomez-Ceballos *et al.*,
Event builder and Level 3 at the CDF experiment,
Nucl. Instrum. Meth. A 518, 522-524 (2004).

[56] T. Sjöstrand, S. Mrenna, P. Skands,
PYTHIA 6.4 Physics and Manual,
hep-ph/0603175 (2006).

[57] B. Andersson, G. Gustafson, G. Ingelman and T. Sjostrand,
Parton Fragmentation and String Dynamics,
Phys. Rept. 97, 31 (1983).

[58] T. Sjostrand,
Jet Fragmentation of Nearby Partons,
Nucl. Phys. B 248, 469 (1984).

[59] G. Corcella, *et al.*,
HERWIG 6: An event generator for hadron emission reactions with interfering gluons (including supersymmetric processes),
J. High Energy Phys. 01, 010 (2001).

[60] D. Amati and G. Veneziano,
Preconfinement as a Property of Perturbative QCD,
Phys. Lett. B 83, 87 (1979).

[61] S. R. Slabospitsky, L. Sonnenschein,
Comput. Phys. Commun. 148, 87 (2002),
arXiv:hep-ph/0201292.

[62] F. Maltoni and T. Stelzer,
MadEvent: Automatic event generation with MadGraph,
J. High Energy Phys. 02, 027 (2003).

[63] T. Stelzer and W. F. Long,
Automatic generation of tree level helicity amplitudes,
Comput. Phys. Commun. 81, 357-371 (1994).

[64] M. Mangano*et al.*,
ALPGEN, a generator for hard multiparton processes in hadronic collisions,
J. High Energy Phys. 07, 001 (2003).

[65] S. Agostinelli *et al.*,
GEANT 4 - A Simulation Toolkit,
Nucl. Instrum. Meth. A 506, 250 (2003).

[66] G. Grindhammer and S. Peters,
The Parameterized Simulation of Electromagnetic Showers in Homogeneous and Sampling Calorimeters,
arxiv.org:hep-ex/001020.

[67] E. Gerchtein and M. Paulini,
CDF detector simulation framework and performance,
Talk given at 2003 Conference on Computing in High-Energy and Nuclear Physics, (2003).

[68] A. Mukherjee,
CTC and VTX Tracking,
Internal CDF note 5490.

[69] P. Azzi, G. Busetto, P. Gatti, and A. Ribon,
Histogram Tracking in the COT,
Internal CDF note 5562.

[70] F. D. Snider,
Tracking at CDF: Algorithms and experience from Run I and Run II,
Nucl. Instrum. Meth. A 566, 133-141 (2006).

[71] C. Hays *et al.*,
The COT Pattern Recognition Algorithm and Offline Code,
Internal CDF Note 6692 (2004).

[72] K. Bloom and W.-M. Yao,
Outside-In Silicon Tracking at CDF,
Internal CDF note 5991.

[73] C. Neu for the CDF collaboration,
CDF b-tagging: Measuring efficiency and false positive rate,
Presented at TOP 2006: International Workshop on Top Quark Physics, Coimbra, Portugal (2006).

[74] C. Neu *et al.*,
SecVtx Optimization Studies for 5.3.3 Analyses,
Internal CDF Note 7578 (2005).

[75] M. Feindt,
A neural Bayesian estimator for conditional probability densities.
arXiv:physics/0402093 (2004).

[76] M. Feindt and U. Kerzel,
The NeuroBayes neural network package.
Nucl. Instrum. Meth. A 559, 190-194 (2006).

[77] V. Blobel and E. Lohrmann,
Statistische und numerische Methoden der Datenanalyse.
Teubner Stuttgart Leibzig, (1998).

[78] S. Richter, Ph.D. thesis, University of Karlsruhe (2007),
Search for electroweak single top-quark production with the CDF II experiment,
FERMILAB-THESIS-2007-35 (2007).

[79] E. Sexton-Kennedy and P. Murat*et al.*,
Commissioning the CDF Offline Software,
physics/0306112 (2003).

[80] H. Frisch,
The Good Run List,
Internal CDF Note 5613 (2001).

[81] *Good Run list Version 19*,
http://www-cdf.fnal.gov/internal/dqm/goodrun/v19/goodrun_em_mu_si_cmxignored.list.

[82] V. Martin,
High p_{T} muons, recommended cuts and efficiencies for release 5.3,
Internal CDF Note 7031 (2004).

[83] V. Martin,
High-p_{T} muon ID cuts and efficiencies for use with 5.3.1 data and 5.3.3 MC, Internal CDF Note 7367 (2005).

[84] C. Hill *et al.*,
Electron identification in offline release 5.3, Internal CDF Note 7309 (2005).

[85] A. A. Ashimova, S. R. Slabospitsky,
Phys. Lett. B 668, 282-285 (2008).

[86] E. E. Boos, L. V. Dudko and V. I Savrin,
CMS Note 2000/065 (2000).

[87] Z. Sullivan,
Understanding single-top-quark production and jets at hadron colliders, Phys. Rev. D 70, 114012 (2004).

[88] Y. L. Dokshitzer,
Calculation of the structure functions for deep inelastic scattering and e+ e- annihilation by perturbation theory in quantum chromodynamics, Sov. Phys. JETP 46, 641-653 (1977).

[89] V. N. Gribov and L. N. Lipatov,
Deep inelastic e p scattering in perturbation theory, Sov. J. Nucl. Phys. 15, 438-450 (1972).

[90] G. Altarelli and G. Parisi,
Asymptotic freedom in parton language, Nucl. Phys. B 126, 298 (1977).

[91] H. L. Lai *et al.*,
Global QCD analysis of parton structure of the nucleon: CTEQ5 parton distributions, Eur. Phys. J. C 12, 375-392 (2000).

[92] J. Lueck (Karlsruhe U., EKP),
Masters Thesis, Kinematics of electroweak single top quark production, FERMILAB-MASTERS-2006-01 (2006).

[93] N. Kidonakis and R. Vogt,
Phys. Rev. D 68, 114014 (2003), hep-ph/0308222.

[94] D. Hirschbühl, J. Lück, Th. Müller, A. Papaikonomou, Th. Peiffer, M. Renz, S. Richter, I. Schall, J. Wagner-Kuhr, W. Wagner,
Search for single top–quark production with neural networks using 2.2fb^{-1}, Internal CDF Note 9107 (2008).

[95] S. Budd *et al.*,
Estimation and modeling of non-W background for single-top searches,
Internal CDF Note 8489 (2006).

[96] T. Chwalek *et al.*,
Update of the neural network b tagger for single-top analyses,
Internal CDF Note 8903 (2007).

[97] S. Elbracht *et al.* ,
Fitting the flavor composition of lepton trigger data in bins of MET and lepton isolation,
Internal CDF Note 9131 (2007).

[98] J. Adelman, S. Budd, P. Dong, R. Erbacher, S. Grinstein, D. Hare, K. Lannon. E. Palencia, C. Plager, J. Slaunwhite, D. Sherman, T. Schwarz, V. Sorin, B. Stelzer, R. Wallny,
Internal CDF Note 9185 (2008).

[99] R. Bonciani *et al.*,
Nucl. Phys. B 529, 424 (1998).

[100] M. Cacciari *et al.*,
J. High Energy Phys. 0404, 068 (2004).

[101] A. Abulencia *et al.*,
Top quark mass measurement using the template method in the lepton + jets channel at CDF II,
Phys. Rev. D 73, 032003 (2006).

[102] J. J. Liu *et. al.*
Phys. Rev. D 72, 074018 (2005).

[103] J. J. Zhang *et al.*,
arXiv:0810.3889v4 [hep-ph].

[104] T. Aaltonen *et al.* (CDF Collaboration),
Search for top-quark production via flavor-changing neutral currents in W+1 jet events at CDF,
Phys. Rev. Lett. 102, 151801 (2009).

[105] J. J. Liu, C. S. Li, L. L. Yang, L. G. Jin,
Phys. Lett. B 599, 92 (2004).

[106] J. M. Yang, B.-L. Young, X. Zhang,
Phys. Rev. D 58, 055001 (1998).